AD-A170 788   ANISOTROPY AND MICROSTRUCTURE OF RARE EARTH PERMANENT   1/2
MAGNET MATERIALS..(U) TECHNISCHE UNIV VIENNA (AUSTRIA)
INST OF APPLIED AND TECHNICA.. P SKALICKY ET AL.
UNCLASSIFIED   JAN 86 R/D-4060A-R-MS DAJA45-84-C-0010   F/G 20/3   NL

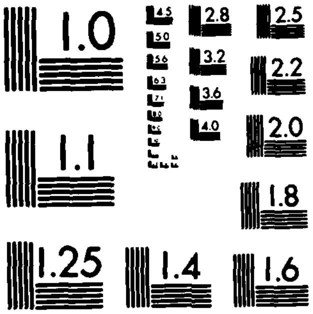

MICROCOPY RESOLUTION TEST CHART
NATIONAL BUREAU OF STANDARDS-1963-A

12

ANISOTROPY AND MICROSTRUCTURE
OF
RARE EARTH PERMANENT MAGNET MATERIALS

Final
[illegible] REPORT

by

Josef Fidler
Roland Grössinger
Hans Kirchmayr
Peter Skalicky

January 1986

United States Army
EUROPEAN RESEARCH OFFICE OF THE U.S. ARMY
LONDON ENGLAND

CONTRACT NUMBER DAJA 45-84-C-0010

Peter Skalicky
Institute of Applied and Technical Physics,
[illegible]
[illegible] Vienna, Austria

[illegible]

Unclassified
SECURITY CLASSIFICATION OF THIS PAGE *(When Data Entered)*

413949

ADA170788
R&D 4060A-R-MS

REPORT DOCUMENTATION PAGE

READ INSTRUCTIONS BEFORE COMPLETING FORM

1. REPORT NUMBER

2. GOVT ACCESSION NO.

3. RECIPIENT'S CATALOG NUMBER

4. TITLE *(and Subtitle)*
Anisotropy and Microstructure of Rare Earth Permanent Magnet Materials

5. TYPE OF REPORT & PERIOD COVERED
Final Report
December 1983-March 1986

6. PERFORMING ORG. REPORT NUMBER

7. AUTHOR(s)
Peter Skalicky, Josef Fidler, Roland Grossinger, and Hans Kirchmayr

8. CONTRACT OR GRANT NUMBER(s)
DAJA45-84-C-0010

9. PERFORMING ORGANIZATION NAME AND ADDRESS
Institute of Applied and Technical Physics
Technical University, Vienna
Karlsplatz 13, A-1040 Vienna, Austria

10. PROGRAM ELEMENT, PROJECT, TASK AREA & WORK UNIT NUMBERS
PE 61102A
1L161102BH57-04
ASH57

11. CONTROLLING OFFICE NAME AND ADDRESS
USARDSG-UK
Box 65
FPO NY 09510-1500

12. REPORT DATE
January 1986

13. NUMBER OF PAGES
50

14. MONITORING AGENCY NAME & ADDRESS*(if different from Controlling Office)*

15. SECURITY CLASS. *(of this report)*
Unclassified

15a. DECLASSIFICATION/DOWNGRADING SCHEDULE

16. DISTRIBUTION STATEMENT *(of this Report)*
Approved for Public Release; distribution unlimited.

17. DISTRIBUTION STATEMENT *(of the abstract entered in Block 20, if different from Report)*

18. SUPPLEMENTARY NOTES

19. KEY WORDS *(Continue on reverse side if necessary and identify by block number)*
Rare earth-iron permanent magnets, microstructure of Nd-Fe-B magnets, magnetic anisotropy of Nd-Fe-B magnets, electron microscopy, pulsed field technique, intrinsic magnetic coercive force

20. ABSTRACT *(Continue on reverse side if necessary and identify by block number)*

The present report is divided into two parts, the microstructural investigations and the anisotropy measurements of rare earth permanent magnet materials. Section I shows that the hardmagnetic properties, i.e. coercivity, of the individual Nd-Fe-B permanent magnet material strongly depends on the compositional and processing parameters (milling, blending, anealing, etc.) and are directly correlated to the microstructural properties (grain size, compo-

DD FORM 1 JAN 73 **1473** EDITION OF 1 NOV 65 IS OBSOLETE.

UNCLASSIFIED
SECURITY CLASSIFICATION OF THIS PAGE *(When Data Entered)*

sition and distribution of phases, crystal defects and precipitates) and to the magnetocrystalline anisotropy of the material. By means of transmission electron microscopy together with STEM X-ray microanalysis at least three categories of phases were identified in sintered rare earth-iron permanent magnets. From microstructural investigations it can be assumed that the coercivity of sintered rare earth-iron permanent magnet materials is controlled by the nucleation and expansion fields for reversed domains.

In Section II the magnetic anisotropy measurements of varoius rare earth-iron based magnets between 80 K and the Curie temperature are shown and the results are discussed by means of an expanded model for the anisotropy field. From the study of the temperature dependence of the anisotropy field of the mixed crystal series $(N,RE)_{15}Fe_{77}B_{8}$ (RE=Y,La,Ce) the One Ion character of the Nd sublattice is shown.

Besides the anisotropy field $H_A(T)$ also the intrinsic coercive force ${}_iH_c(T)$ was determined by means of the pulsed field technique and the results are discussed in terms of pinning and nucleation models for revesed domains.

TABLE OF CONTENTS

SECTION I: MICROSTRUCTURE AND COERCIVITY OF Nd-Fe-B BASED MATERIALS

Page

SECTION II: ANISOTROPY AND COERCIVITY OF Nd-Fe-B BASED MATERIALS

Page

LIST OF ILLUSTRATIONS

Figure Page

SECTION I:

Figure Page

SECTION II:

LIST OF TABLES

Table

SECTION II: Page

SECTION I

MICROSTRUCTURE AND COERCIVITY OF Nd-Fe-B BASED MATERIALS

by

J. Fidler and P. Skalicky
Institute of Applied and Technical Physics
Technical University of Vienna
Karlsplatz 13, A-1040 Vienna, Austria.

(1) INTRODUCTION

The magnetic hardness of permanent magnet materials depends critically on the microstructure of the individual magnets. In the light of the historical development of the coercivity and the energy density product of hard magnetic materials the improvement of the energy density product is closely connected with a better understanding of the mechanismus leading to higher coercive forces of the magnets (1). The coercive force of hard magnetic materials is determined either by the nucleation of reserved magnetic domains at magnetic fields which are lower than the theorectical maximum value of the anisotropy-field, or by the strong pinning of domain walls at crystal lattice defects and precipitates during the magnetization reversal (2,3). Analytical investigations for the characterization of the microstructural parameters, such as grain size distribution, phase determination, chemical homogeneity of the grains, crystal lattice defects and precipitates, are necessary for a better knowledge of the limiting factors of the coercivity.

However, the technical important parameters such as the remanence and the coercivity are not only determined by the intrinsic properties such as the spontaneous magnetization and the anisotropy but also by more complicated features, e.g. the interaction of domain walls with crystal defects. For a basic understanding of the coercivity the magnetocrystalline anisotropy must be known. The high theoretical coercive fields due to the high magnetocrystalline anisotropy are not obtained in rare earth permanent materials. Therefore microstructural investigations are necessary to identify the various phases occuring in permanent magnetic materials. Special emphasis of our investigations has been laid on the measurement of the hard magnetic properties and on the investigation of the microstructure of newly developed hard magnetic materials. Using high resolution and analytical electron microscopy together with X-ray microanalysis and metallography the microstructure of various magnetic materials was characterized and correlated with the hardmagnetic properties of the magnets (4,5,6,7).

During the period Jan.1985 until Dec.1985 various Nd-Fe-B sintered magnets produced by different producers were investigated. Special attention of our microstructural investigations have been laid on the following:

- Grain size and grain size distribution
- Phase analysis (crystal structure and chemical composition)
- Grain boundary-phase (crystalline or amorphous)
- Influence of heat treatments on microstructure and hard magnetic properties
- Influence of sintering-aid phases (liquid phase sintering)
- Crystal lattice defects

(2) MICROSTRUCTURE AND COERCIVITY OF Nd-Fe-B PERMANENT MAGNET MATERIALS

Sintered magnets with nominal composition close to $Nd_{15}Fe_{77}B_8$ exhibit the highest energy density products so far (8,9). These magnets show magnetization curves according to nucleation of reversed domains (3). The new class rare earth-iron permanent magnet materials can be divided into two types (Fig.1) depending on whether the magnet was produced by a powder metallurgical process (8,10) or derived from rapidly solidified melt-spun ribbons (11). Sintered Nd-Fe-B magnets exhibit grain size up to 15µm, whereas rapidly solidified melt-spun ribbon-magnets exhibit grain size in the order of 50nm. Since the temperature dependence coefficient of the coercivity of rare earth-iron permanent magnets is considerably high, which limits the temperature range for many applications, our special emphasis will be laid on magnets with very high coercive forces at room temperature, such as Dy- or Tb-containign Nd-Fe-B magnets, or magnets with a special multi-step heat treatment (12) in order to increase the coercivity. We also want to investigate the role of transition element or rare earth oxide (13) substitutions on the microstructure of Nd-Fe-B sintered magnets, since such additions also increase the coercivity.

For a better understanding of the coercivity mechanism the knowledge of the crystal structure and the chemical composition of the various phases occuring in Nd-Fe-B magnet materials is necessary. A result of our electron microscope studies so far an identical microstructure in various sintered magnets, supplied by different producers, was observed (14,15). The following phases (Fig.2 and 3) were detected by analytical electron microscopic techniques and are summarized in Table 1 .

Fig.1:

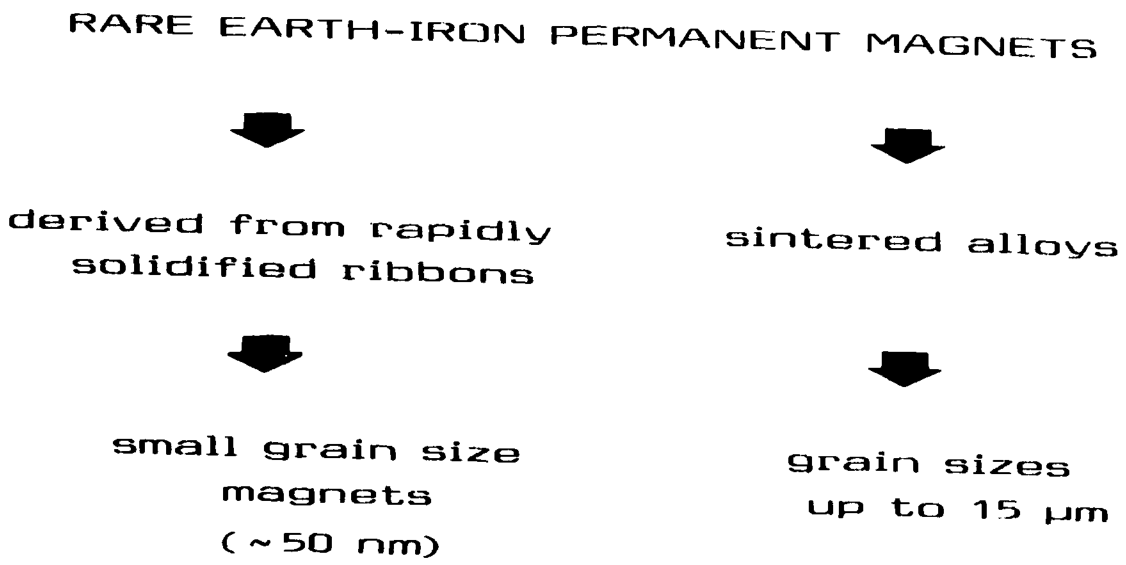
RARE EARTH-IRON PERMANENT MAGNETS
derived from rapidly solidified ribbons
sintered alloys
small grain size magnets (~50 nm)
grain sizes up to 15 µm

Fig.2: Optical (a) and electron (b) micrographs showing the three - phase microstructure of a $Nd_{15}Fe_{77}B_8$ sintered magnet. The oprical micrograph (a) shows the magnetic domain structure within the hard magnetic grains of phase A.

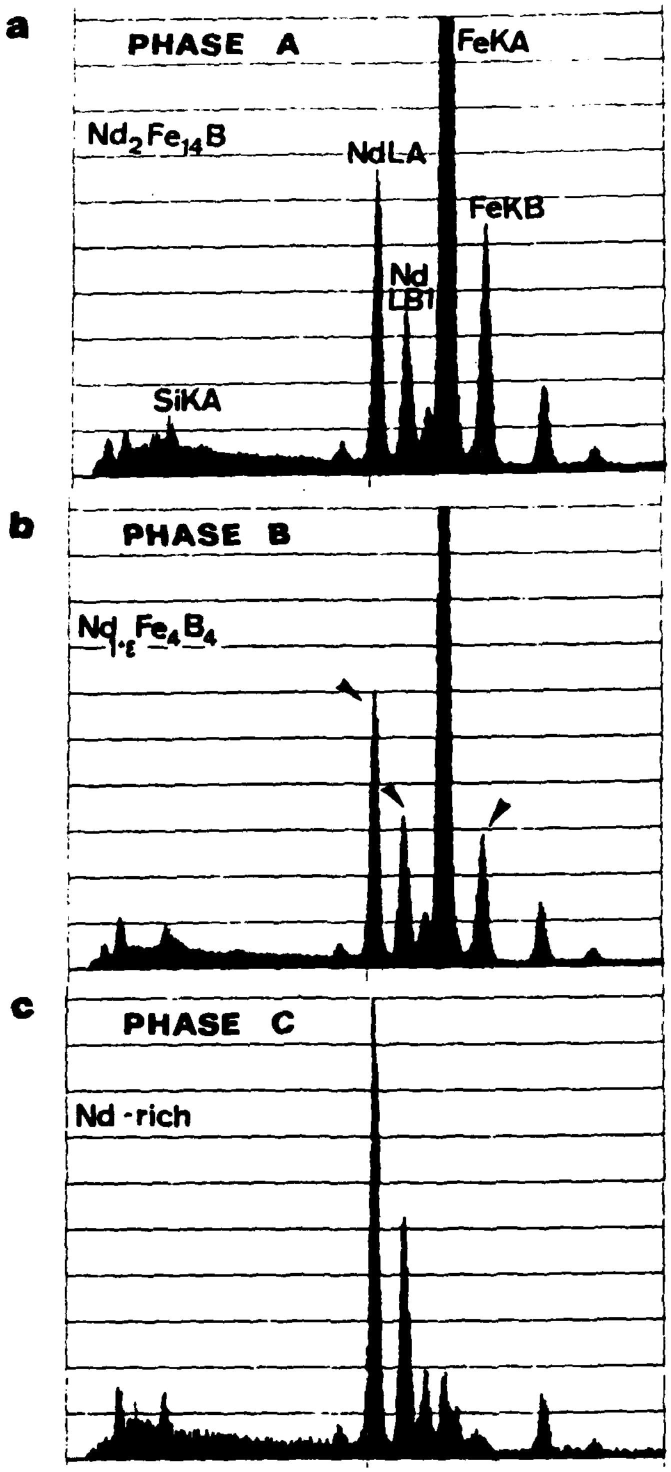

Fig.3: Energy dispersive X-ray spectra corresponding to the phases found in the Nd-Fe-B magnet of Fig.2.

Table1 : PHASES IN SINTERED $Nd_{15}Fe_{77}B_8$ MAGNETS

				MH
A	$Nd_2Fe_{14}B$	tetr	a=0.88 nm, c=1.22 nm	950
B	$Nd_{1+\epsilon}Fe_4B_4$	tetr.	a=0.71 nm, c=14.5 nm	1430
C	Nd-rich	f.c.c.	a=0.52 nm	360
D	Nd-oxides	hex.	a=0.38 nm, c=0.60 nm	
E	α - Fe	b.c.c.	a=0.29 nm	190

Not detected: Nd_2Fe_{17} , $NdFe_2$, MH .... microhardness

Phase A is always found to be free of crystal lattice defects and corresponds to the hard magnetic boride $Nd_2Fe_{14}B$. In the energy dispersive X-ray spectrum of phase A (Fig.3a) the FeKB-peak lies between the NdlA- and NdlB1-peak.

Phase B is Nd-richer than phase A. In the corresponding X-ray spectrum the FeKB-peak is smaller than the NdLB1-peak (Fig.3.b). The ratio of the Fe- to the Nd-concentration (in at%) was found to be in the range 3.6 to 3.9. Our high resolution electron studies revealed a crystal lattice periodicity of 0.4nm, 4.8nm and 14.5nm (5). Both results, obtained by X-ray STEM microanalysis and high resolution electron microscopy, are in agreement with structural and compositional data of the phase $Nd_{1.109}Fe_4B_4$ (16). The grain interior of phase B shows a high crystal defect density, which explains the large value of the microhardness (see Table 1).

Phase C is found to be a Nd-rich phase. The ratio of the Nd- to Fe-concentration (in at%) determined by X-ray microanalysis is about 6 corresponding to about 85 at% Nd. This phase may also occur with some content of oxygen and/or boron. Phase C is mainly found as isolated inclusions near grain boundaries or as layer phase along grain boundaries.

It should be mentioned that depending on the raw material used by the producer various impurities such as silicon, chlorine, phosphorus, niobium, platinum, tin etc. are found in all of the phases above listed. As result of our investigations of sintered NdFeB magnets, produced by a powder metallurgical process, the coercivity is primarily determined by the magnetization reversal within the hard magnetic $Nd_2Fe_{14}B$ grains and is limited by the nucleation and expansion field for reversed domains. The layer phase, separating the hard magnetic grains, contributes also to the coercivity. Replacing neodynium by dysprosium (Nd:Dy=10:1) increases the coercivity, but does not show any drastic effect on the composition of the different phases, whereas generally the grain size of such magnets is considerably smaller than in magnets without dysprosium.

(3) INFLUENCE OF RAW MATERIAL AND PROCESSING PARAMETERS ON MICROSTRUCTURE AND HARD MAGNETIC PROPERTIES

The nature of the raw material has an influence on the final hard magnetic properties of rare earth permanent magnets. For the seperation of neodymium from the raw material in the form of oxides, chlorides and flourides different techniques are used (17):

(a) NdF_3 or $NdCl_3$ + Ca (reduction) + Fe → Nd-Fe

(b) Nd_2O_3 + Ca (reduction) + Fe → Nd-Fe

(c) NdF_3 or $NdCl_3$ + electrotwinning → Nd metal

Depending on the type of the separation technique used the Nd-rich starting material for the magnet production contains different rare earth impurities (mainly lanthanum and praseodymium) and non-rare earth impurities, particularly calcium, magnesium aluminium, platinum and other refractory metals. Calcium-oxid precipitates are found in rare earth magnets where a raw material is used which was prepared by the calciothermic reduction process (1). Due to the high melting point of elemental boron (2.300°C) a ferro-boron alloy is used together with a neodymium-iron alloy for the preparation of the final alloy close to the nominal composition $Nd_{15}Fe_{77}B_8$, which is the starting material for sintered Nd-Fe-B magnets. Ferro-boron alloys mainly contain silicon impurities. The main production steps for processing of sintered rare earth permanent magnets are:

ALLOY PREPARATION
MILLING
COMPOSITIONAL CONTROL
PARTICLE ALIGNMENT and PRESSING
SINTERING and HEAT TREATMENT
MACHINING and FINAL MAGNETIZING

The molten alloy close to the nominal composition of $Nd_{15}Fe_{77}B_8$ is pulvarized to a powder of several microns during different milling steps. The hard magnetic properties of the final magnet strongly depend on the following properties of the powder:

Average particle size
Particle size distribution
Particle shape
Particle surface (oxidation)
Particle chemistry and structure
Grain size

After grinding the powder particles may be single crystals or may be polycrystalline. In some cases the agglomeration of individual particles must be taken into account and it must be distinguished between grain, particle and agglomerate (Fig.4). The scanning electron micrograph of Fig.5 shows the irregular particle shapes obtained after the compacting and alignment process of a Nd-Fe-B powder. The porosity of the individual particles which is another structural characteritic does not play an important role in the case of optimally sintered Nd-Fe-B magnets. The compacting parameters (die-pressing or isostatic pressing, D.C. or pulsed magnetic field, pressing pressure) determines the degree of particle alignment and therefore controlls the remanence and also the energy density product of the final magnet. Besides the parameters which determine the composition of the phases within the magnets there are also processing parameters, particulary during sintering and annealing steps such as sintering temperature, cooling rate, aging temperature and time, which

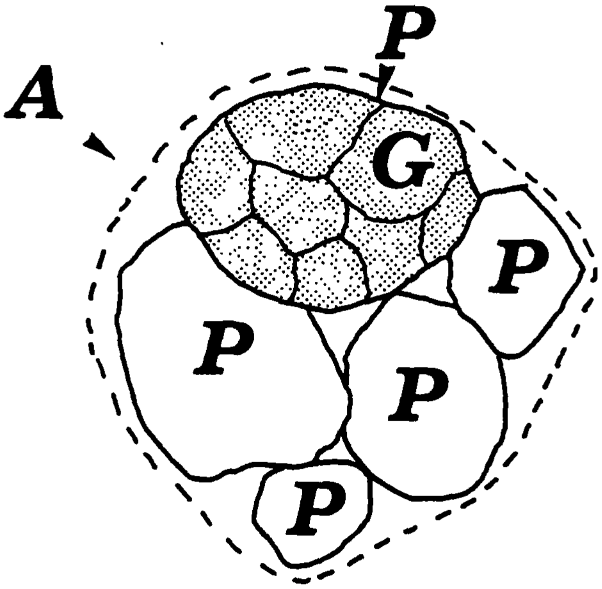

Fig.4: Schematic drawing showing the difference between grains G , individual particles P and agglomerate of particles A.

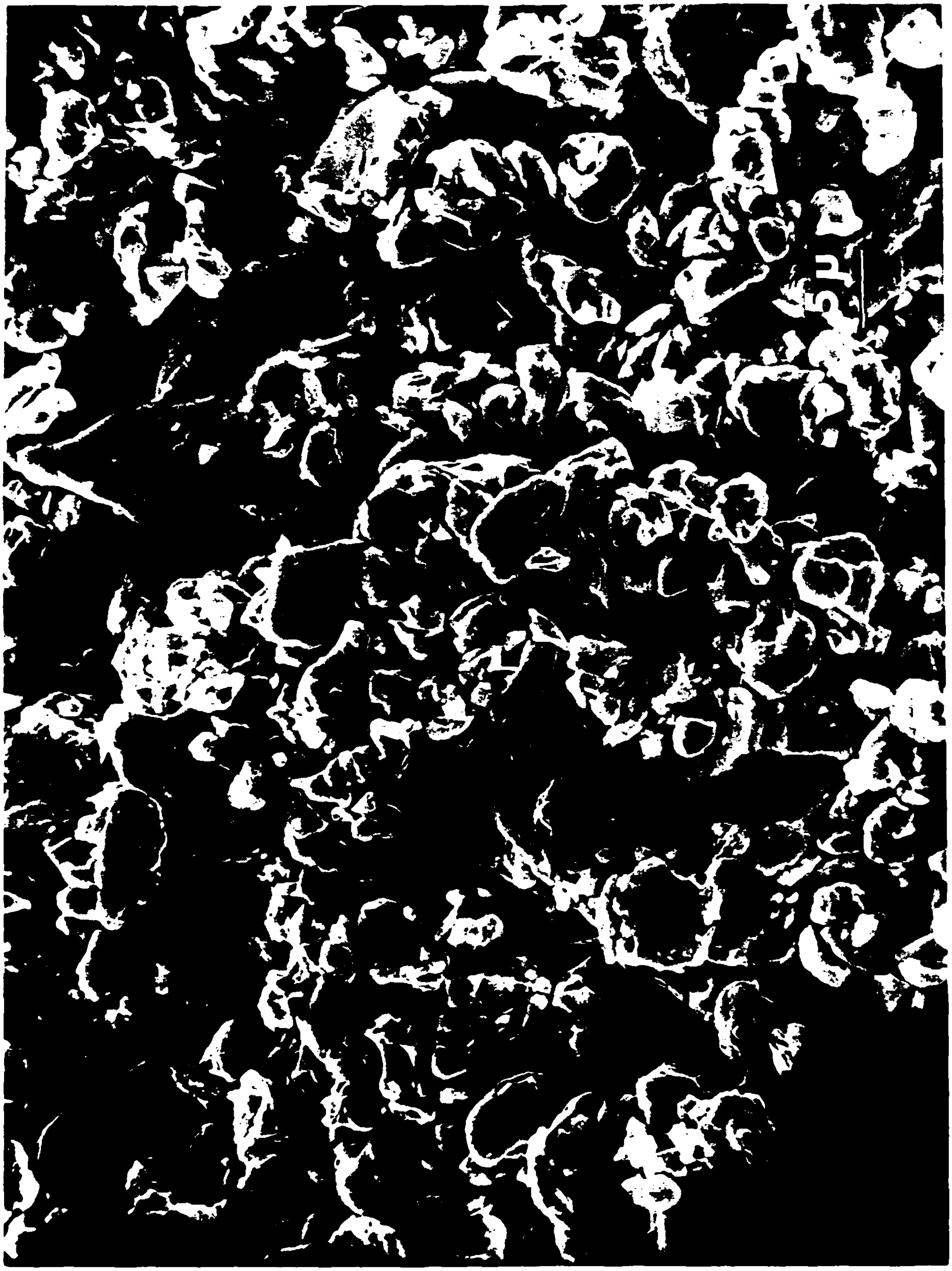

Fig.5: Scanning electron micrograph showing the irregular-shaped particles of a Nd-Fe-B magnet material after milling and pressing and before sintering.

must carefully be controlled in order to achieve maximum intrinsic coercivities. Figure 6 shows a typical schematic heat treatment curve of SmCo 1:5, SmCo 2:17 and NdFeB magnets. The heat treatment sequence to sinter multi-phase SmCo 2:17 magnets is more complicated and time consuming than the ones for sintering SmCo1:5 or NdFeB magnets. The reason for different heat treatment sequencies for the different materials is due to the formation of different microstrucutres (5).

To avoid oxidation the individual processing steps of rare earth permanent magnets must be carried out in inert gas atmosphere or under vacuum. In Nd-Fe-B magents always Nd-oxide particles (Nd_2O_3) can be found even by optical metallography and transmission electron microscopy. Oxygen impurities from the raw material or due to oxygen pick-up during milling should be kept to a minimum, because the coercivity is drasticly reduced in sintered magnets containing more than 1 wt% oxygen. The formation of Nd_2O_3 shifts the effective composition to the Fe-rich side of the effective composition to the Fe-rich side of the phase diagram and also acts as nucleation centres for reversed magnetic domains during the magnetization reversal.

Contrary to the oxid-phase other phases due to impurities, especially of the raw material, were only be detected by analytical electron microsocopy. The electron microtraph of Fig.7a shows a Nd-rich phase containing chlorine with a rather large grain size (about 40µm) which contains a dense net of dislocations. The corresponding X-ray spectrum shows corresponding chlorine and neodynium-peaks.

To obtain highest coercivities the influence of impurities of the raw material must be taken into account to understand the formation of the microstructure of the final magnet.

(4) EXPERIMENTAL

Different types of high coercivity Nd-Fe-B magnet materials were investigated during the period Jan.1985 until Dec.1985. The magnet samples were prepared by different magnet producers. The nominal composition and the heat treatment conditions of the magnet materials varied from sample to sample and are partly unknown (Table 2). Besides highest optical investigations also analytical electron microscope investigations together with X-ray microanalysis were carried out on the magnet samples. The specimens for electron microsocopy were prepared by electro-

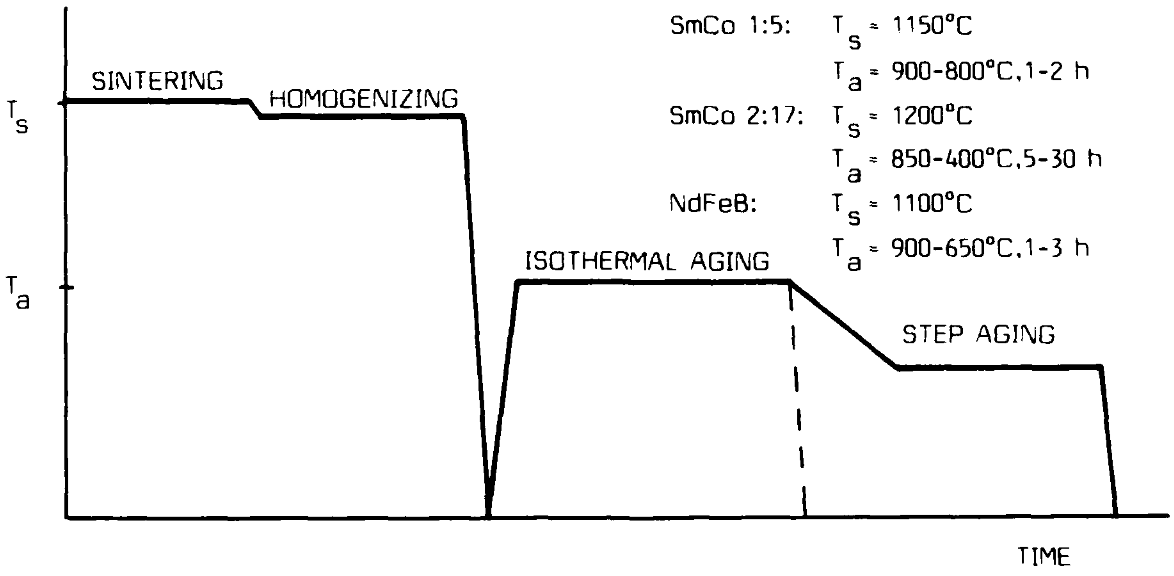

Fig.6:

SCHEMATIC HEAT TREATMENT CURVE OF RARE EARTH PERMANENT MAGNETS

Table 2: Compositional, heat treatment and magnetic data of magnet samples investigated.

Magnet No.	Producer	Nominal Composition	Sintering	Post-Sintering	$(B.H)_{max}$ MGOe	$_JH_c$ kOe	B_r kG
SUM A2 NEOMAX 35	Sumitomo	$Nd_{15}Fe_{77}B_8$	1100°C,1h	600°C,?	34	12	12
CRU 30H CRUMAX 30H	Colt Crucible	?	?	?	30	19	11.2
HIT 1-13	Hitachi	$Nd(Fe_b B_{.1})_{5.4}$	1090°C,2h↓	900°C,2h↘ plus 680°C,1h↓wq	36	11	12.3
HIT 4-13	Hitachi	$Nd(Fe_b B_{.1} Al_{.01})_{5.4}$	//	//	34	12	12.0
HIT A1-11	Hitachi	$(Nd_{.86} Dy_{.14})(Fe_b B_{.08})_{5.4}$	//	//	33	18.5	11.7
HIT B4-4	Hitachi	$(Nd_{.86} Dy_{.14})(Fe_b B_{.08} Al_{.01})_{5.4}$	//	//	30	22	11.2

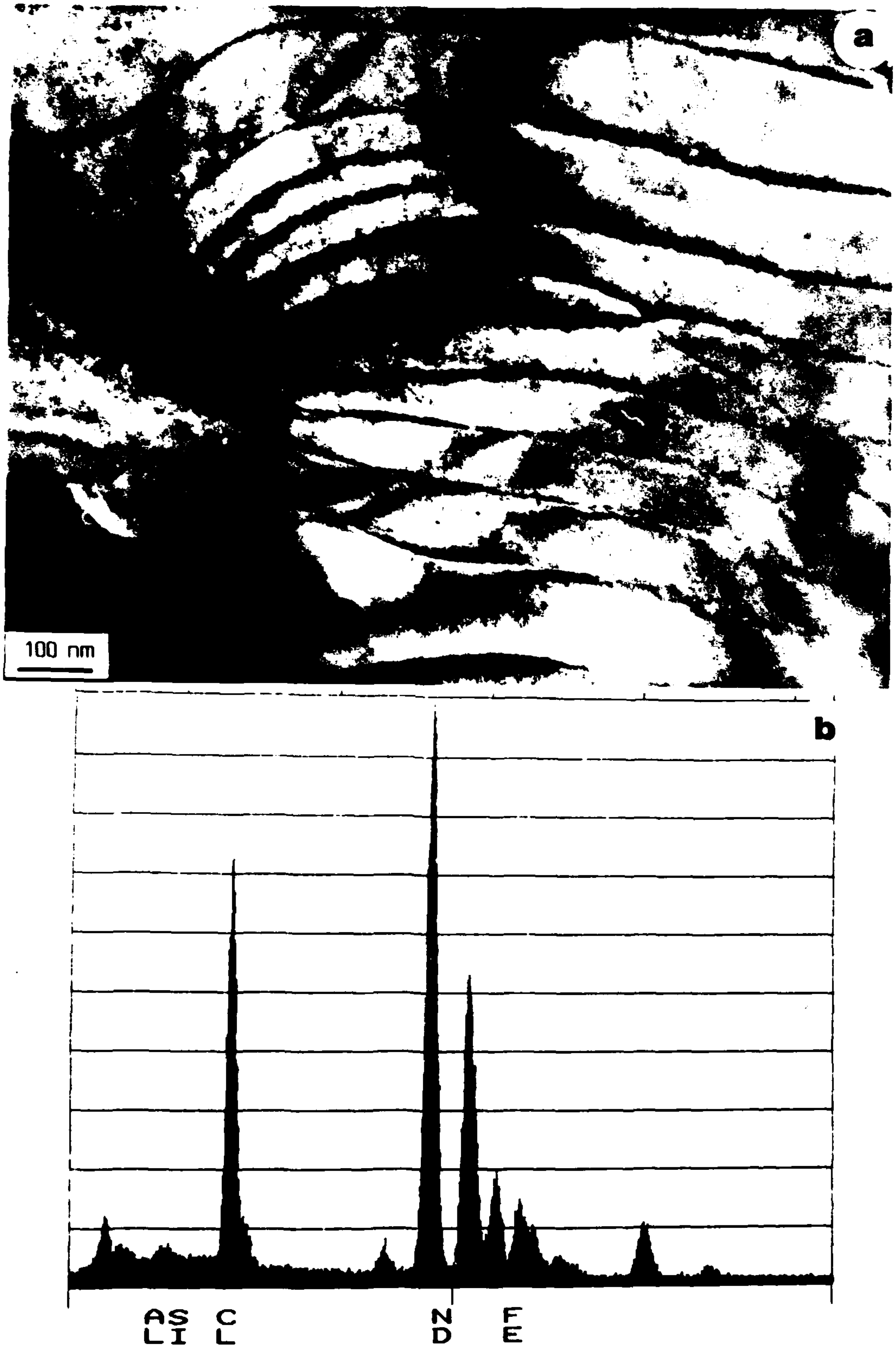

Fig.7: Transmission electron micrograph (a) and corresponding X-ray spectrum of a large precipitate found in Nd-Fe-B magnets. A net of dislocations in the precipitate interior is visible.

polishing and ionmilling procedures. The samples were investigated with a 200 kV electron microscope (JEOL 200CX) which is equipped with ahigh take-off angle energy dispersive (EDS) detector for STEM X-ray microanalysis. The spatial resolution for the microbeam analytical work to determine the composition of small precipitates or thin layer phaes. The beam broadening effect must be taken into account, which is smaller at higher accelerating voltages than lower voltages. Due to the beam broadening the effective area which can analytically be resolved is in the order of the specimen thickness (up to 200 nm) and is only secondary controlled by the spot size of the electron beam (~ 5 nm).

(5) RESULTS AND DISCUSSION

The optical micrographs of Fig.8,9 and 10 show the difference in grain size and the distribution of phases A,B and C in the different magnet materials. The grain size distribution varies from magnet to magnet (Table 3):

Table 3:

Magnet No	Grain size distribution (from - to)
SUM A2	31 - 245 μm^2
CRU 30H	8 - 61 μm^2
HIT 1-13	31 μm^2
4-13	
A1-11	
B4- 4	

The transmission electron microscope investigations reveal a similar microstructure in each of the specimens of the different magnets. Figure 11 and Table 4 show the results of the microanalytical characterization of different grains and precipitates of the magnet sample SUM A2. Analytical investigations of the grain boundary region did not show an increased neodymium content. Moreover in this magnet material occassionally a strong chlorine-peak was

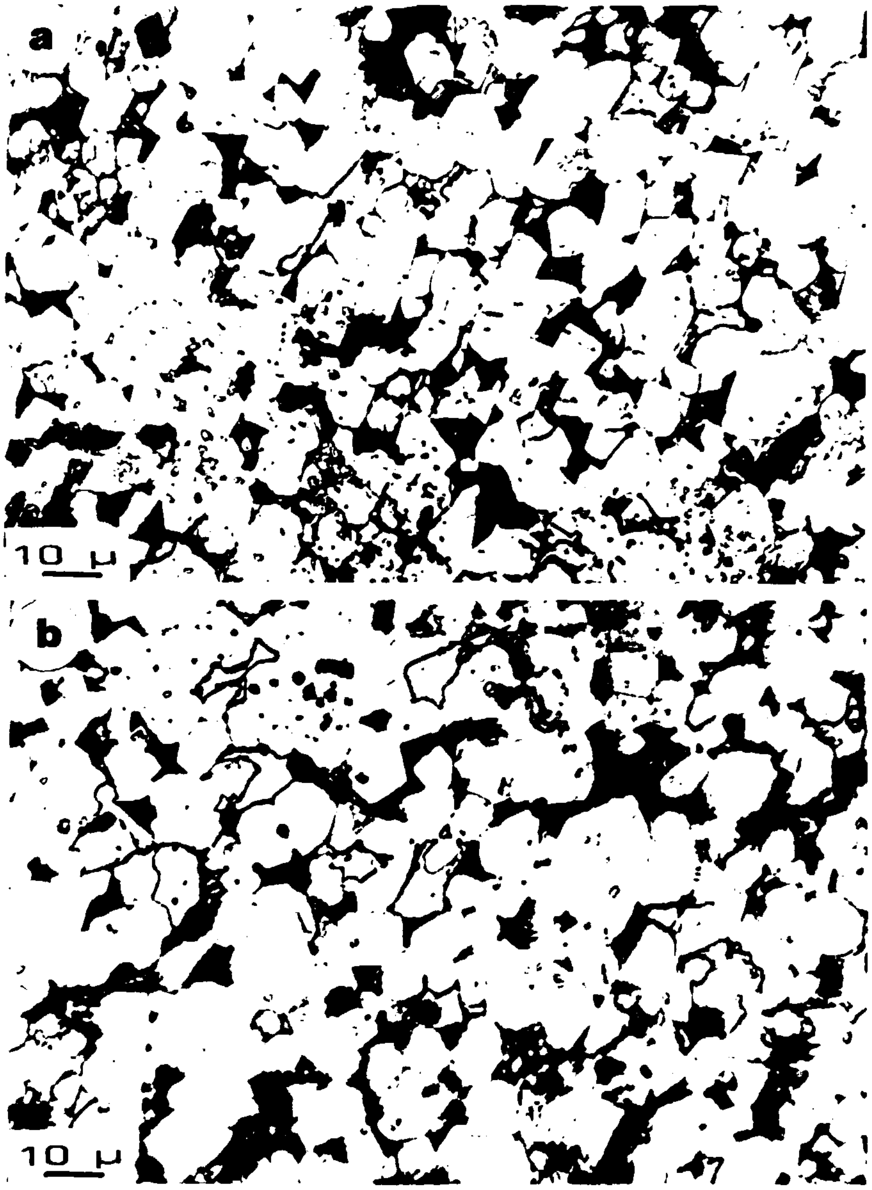

Fig.8: Optical micrographs showing the grain size and phase distribution of the SUM A2 manget. (a) is parallel and (b) is perpendicular to the alignment direction. ${}_JH_c$ = 12 kOe.

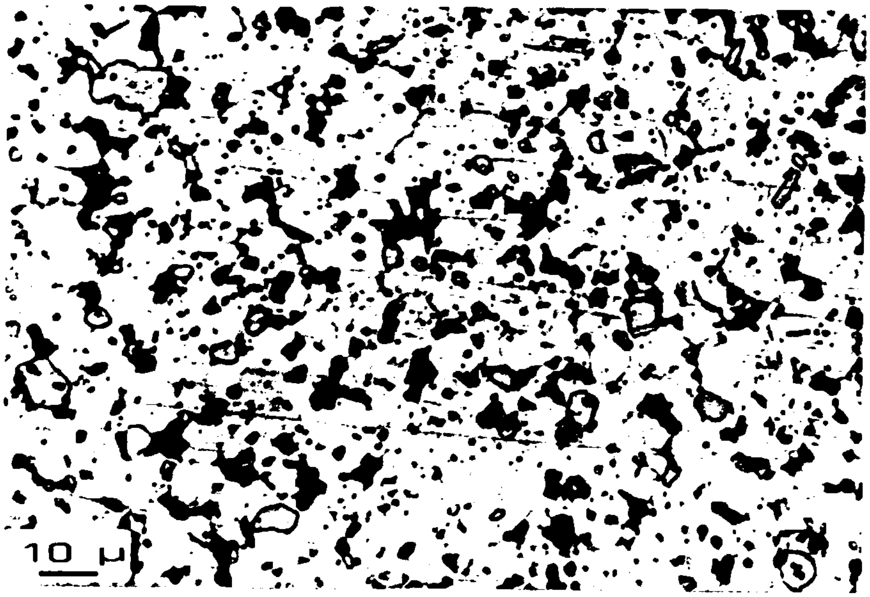

Fig.9: Optical micrograph of the high coercivity magnet CRU 30H. ${}_JH_c$ = 19 kOe.

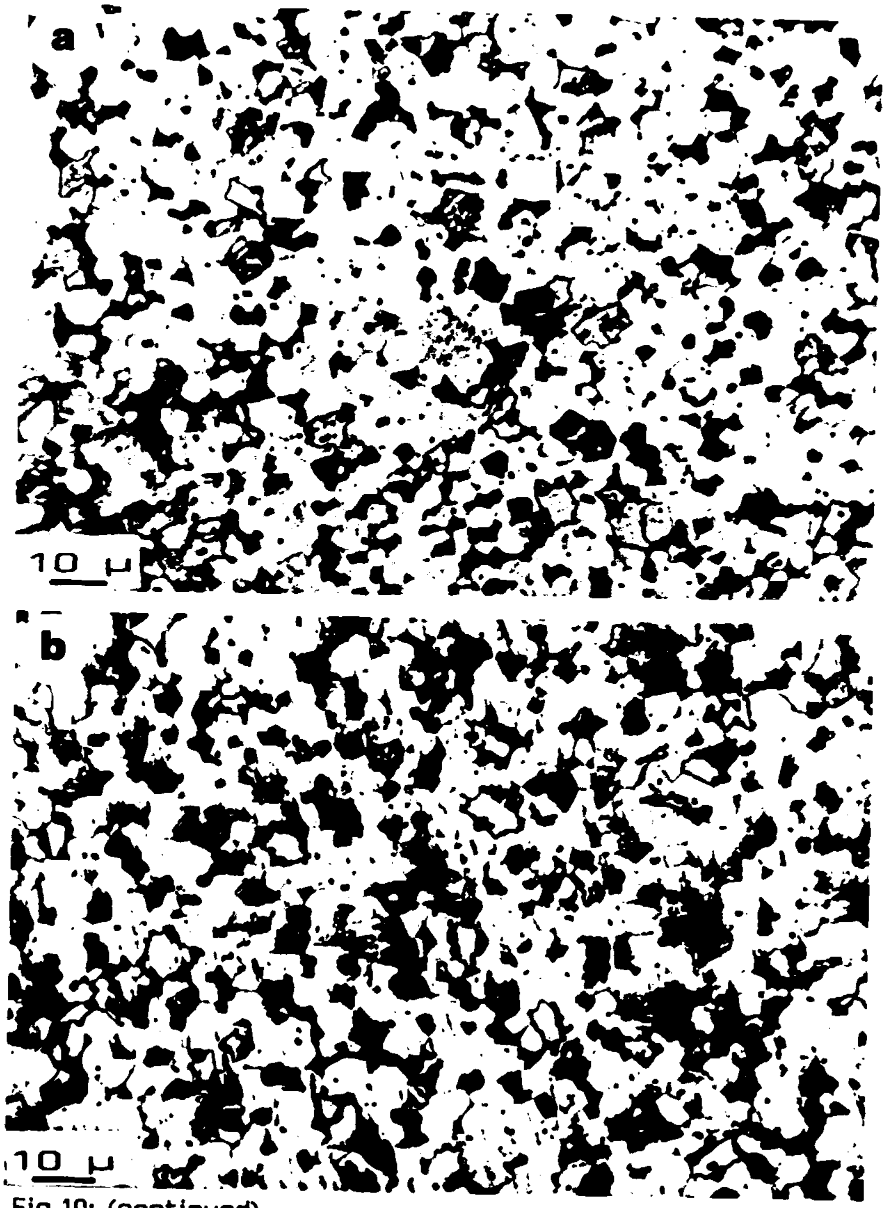

Fig.10: (continued)

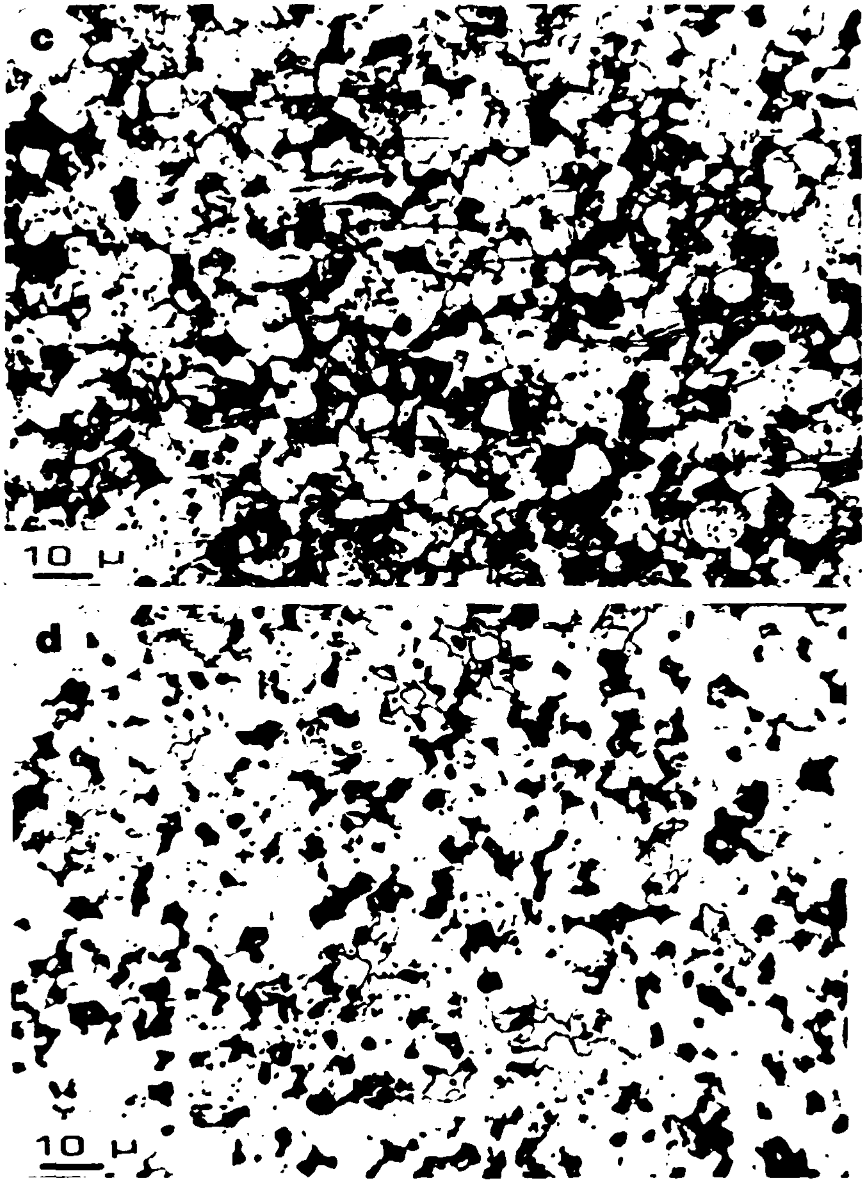

Fig.10: Optical micrographs of magnets (a) HIT 1-13, $_JH_c$ = 11 kOe, (b) HIT 4-13, $_JH_c$ = 12 kOe, (c) HIT A1-11, $_JH_c$ = 18.5 kOe, and (d) HIT B4-4, $_JH_c$ = 22 kOe.

detected in some of the C-phase spectra (Fig.7b). From the characteristic X-ray intensities (NdLA and FeKA) the ratio of iron to neodymium (in at%) was determined to be close to 7 according to the phase $Nd_2Fe_{14}B$. Remarkable is the high SiKA-intensity in some of the X-ray spectra of this phase.

The high coercivity "CRUMAX 30H" magnet exhibit a smaller grain size - in the order of a few microns - than the SUM A2 magnet. Our analytical electron microscope investigations show again a microstructure consisting of three main-phases A,B and C. Figure 13 shows a grain boundary junction of three hard magnetic grains. The chemical composition of these grains was determined by STEM X-ray microanalysis (Fig.12). Compared to the SUM A2 magnet material, the ratio of iron to neodymium is higher and in the order of 7.8 - 8.0. Corresponding to the approximate composition $(Nd_{.9}Dy_{.1})_2Fe_{14}B$ of the hard magnetic phase. Besides the hard magnetic grains also grains with a high density of crystal lattice defects are observed (Fig.14). From the corresponding X-ray spectrum the ratio of iron to neodymium (in at%) was determined as 4.4, which is higher than the value found in Nd-Fe-B magnet materials (3.6 to 3.9). The electron diffraction patterns taken from this phase also differ from previous ones and show a lattice plane periodicity of 0.32 nm and 3.2 nm. This is an evidence that the phase $(Nd,Dy)_{1+\varepsilon}$ Fe_4B_4 (16) occurs in various heavily faulted modifications from the compositional and the structural point of view. The $RE_{1+\varepsilon}$ Fe_4B_4 - compounds are built of incommensurate substructures of rare earth atoms (c_{Nd}=0.35nm), iron atoms (c_{Fe}=0.39nm) and boron atom pairs. The Fe-tetrahedra cains are periodically twisted around the c-axis (tetragonal crystal structure with a=0.71nm and c=14.5nm in the case of the neodymium compound). Fig.15 shows a grain boundary, separating two grains of the hard magnetic phase A. The thickness of the grain boundary layer phase was determined as about 20nm from the electron micrograph. Within the grain interiors also small precipitates with diameters less than 0.1µm are visible. From the X-ray spectrum taken at one of these precipitates we found a Nd-richer composition of this phase than in the surrounding matrix-phase. Because of the limited spatial resolution, i.e. the additional X-ray information from the surrounding matrix-phase, the exact composition of this phase could not be determined. Larger precipitates with diameters of 0.5µm and more,precipitated at the grain boundaries or in the interior of the hard magnetic grains

Table 4: CHEMICAL COMPOSITION

in at %

SUM A2	Fe/Nd	Fe/Al	Fe/Si	Fe+Si+Al/Nd	Fe/Cl	Fe/P+S	Nd/Fe	Nd/Dy	Nd/Cl
A2	6.89		27.8	7.14					
B2	3.77	-	58.4	3.84					
C1			15.6	0.23			4.64		
GB1	7.07		19.3	7.44					
GB2	7.08		27.3	7.34					
GB3	6.92	324	116	6.98					
GB4	6.87		275	6.89					

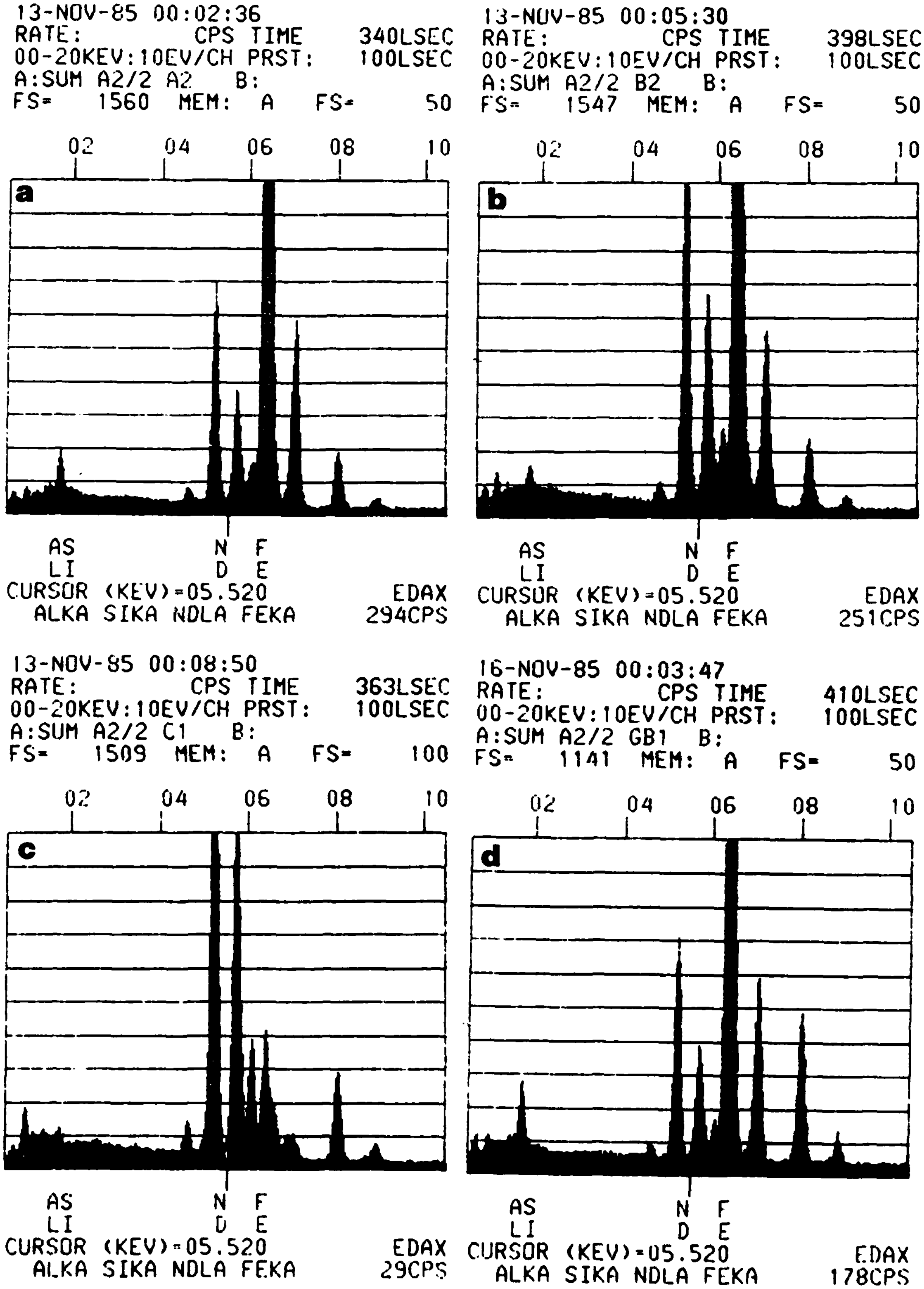

```
13-NOV-85 00:02:36
RATE:          CPS TIME    340LSEC
00-20KEV:10EV/CH PRST:     100LSEC
A:SUM A2/2 A2    B:
FS=    1560  MEM:  A    FS=     50

 AS              N  F
 LI              D  E
CURSOR (KEV)=05.520          EDAX
  ALKA SIKA NDLA FEKA       294CPS
```

```
13-NOV-85 00:05:30
RATE:          CPS TIME    398LSEC
00-20KEV:10EV/CH PRST:     100LSEC
A:SUM A2/2 B2    B:
FS=    1547  MEM:  A    FS=     50

 AS              N  F
 LI              D  E
CURSOR (KEV)=05.520          EDAX
  ALKA SIKA NDLA FEKA       251CPS
```

```
13-NOV-85 00:08:50
RATE:          CPS TIME    363LSEC
00-20KEV:10EV/CH PRST:     100LSEC
A:SUM A2/2 C1    B:
FS=    1509  MEM:  A    FS=    100

 AS              N  F
 LI              D  E
CURSOR (KEV)=05.520          EDAX
  ALKA SIKA NDLA FEKA        29CPS
```

```
16-NOV-85 00:03:47
RATE:          CPS TIME    410LSEC
00-20KEV:10EV/CH PRST:     100LSEC
A:SUM A2/2 GB1   B:
FS=    1141  MEM:  A    FS=     50

 AS              N  F
 LI              D  E
CURSOR (KEV)=05.520          EDAX
  ALKA SIKA NDLA FEKA       178CPS
```

Fig.11: (continued).

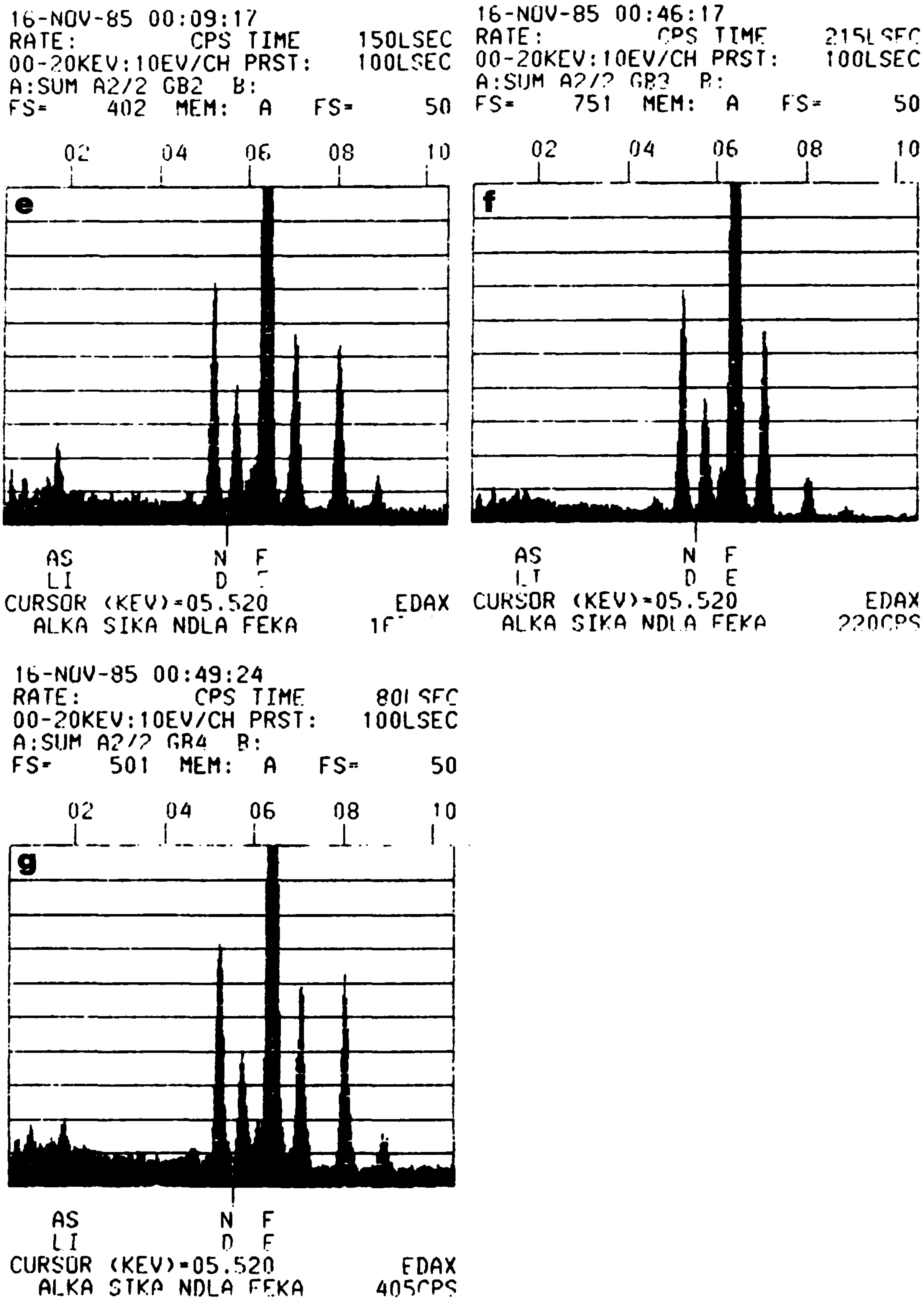

```
16-NOV-85 00:09:17
RATE:              CPS TIME     150LSEC
00-20KEV:10EV/CH PRST:       100LSEC
A:SUM A2/2 GB2  B:
FS=     402  MEM:  A    FS=       50

CURSOR (KEV)=05.520            EDAX
  ALKA SIKA NDLA FEKA        1F
```

```
16-NOV-85 00:46:17
RATE:              CPS TIME     215LSEC
00-20KEV:10EV/CH PRST:       100LSEC
A:SUM A2/2 GB3  B:
FS=     751  MEM:  A    FS=       50

CURSOR (KEV)=05.520            EDAX
  ALKA SIKA NDLA FEKA      220CPS
```

```
16-NOV-85 00:49:24
RATE:              CPS TIME      80LSEC
00-20KEV:10EV/CH PRST:       100LSEC
A:SUM A2/2 GB4  B:
FS=     501  MEM:  A    FS=       50

CURSOR (KEV)=05.520            EDAX
  ALKA SIKA NDLA FEKA      405CPS
```

Fig.11: Energy dispersive X-ray spectra taken from the SuM A2_magnet.

Table 5: CHEMICAL COMPOSITION

in at %

CRU 30H	Fe/Nd	Fe/Al	Fe/Si	$(Fe+Si+Al)/Nd$	Fe/Cl	$Fe/(P+S)$	Nd/Fe	Nd/Dy	Nd/P
A1	7.97		213	8.01					
A2	7.74	-235	22.1	8.13					
B1	4.42	134	28.9	4.60					
C1						2	5.33	9.6	10.1
C3			11.9				5.66	16.6	
C4							7.0	7.0	
GB1	8.21		53.3	8.36					
GB2	7.83	557	70.8	7.95					

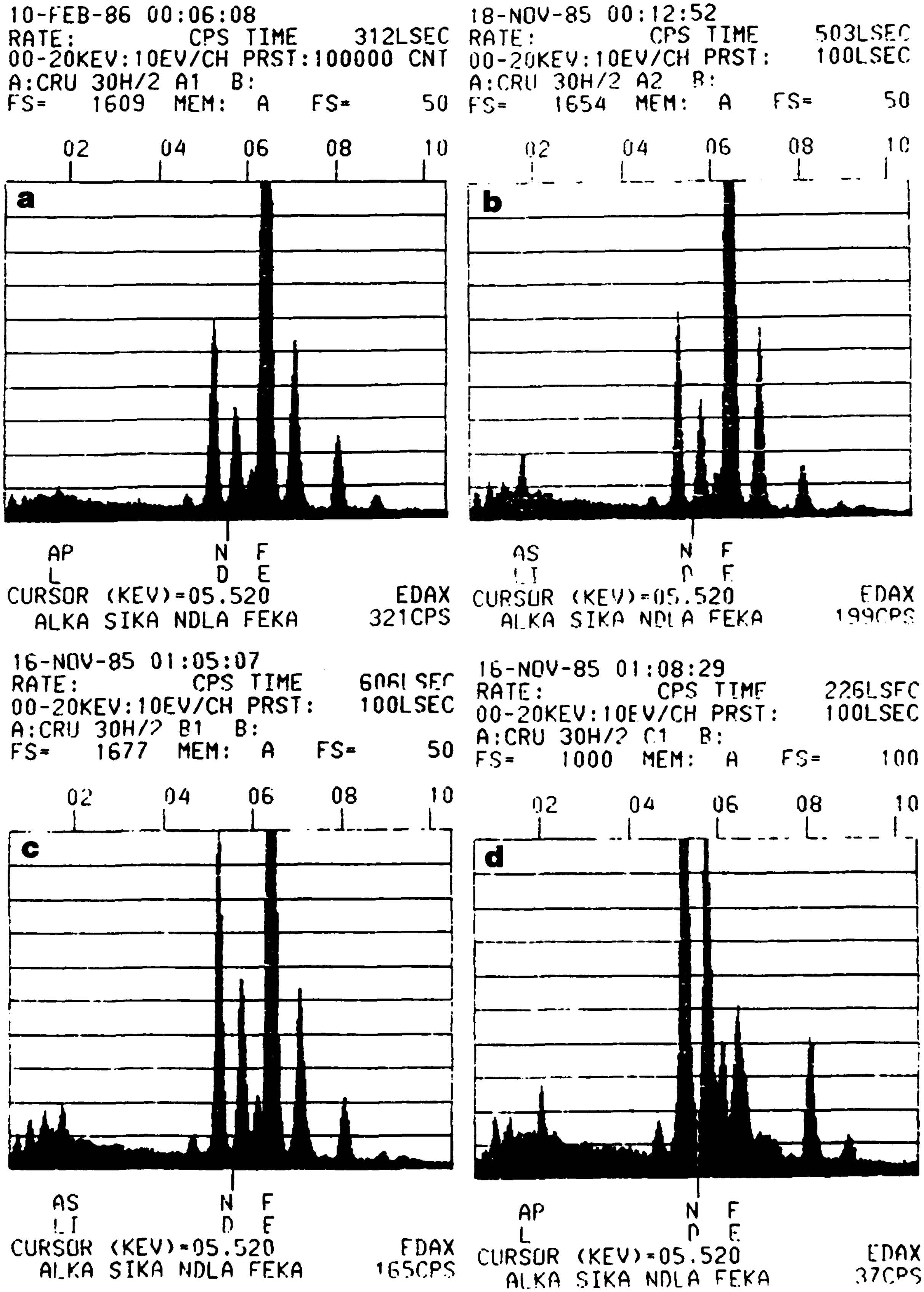

Fig.12: (continued).

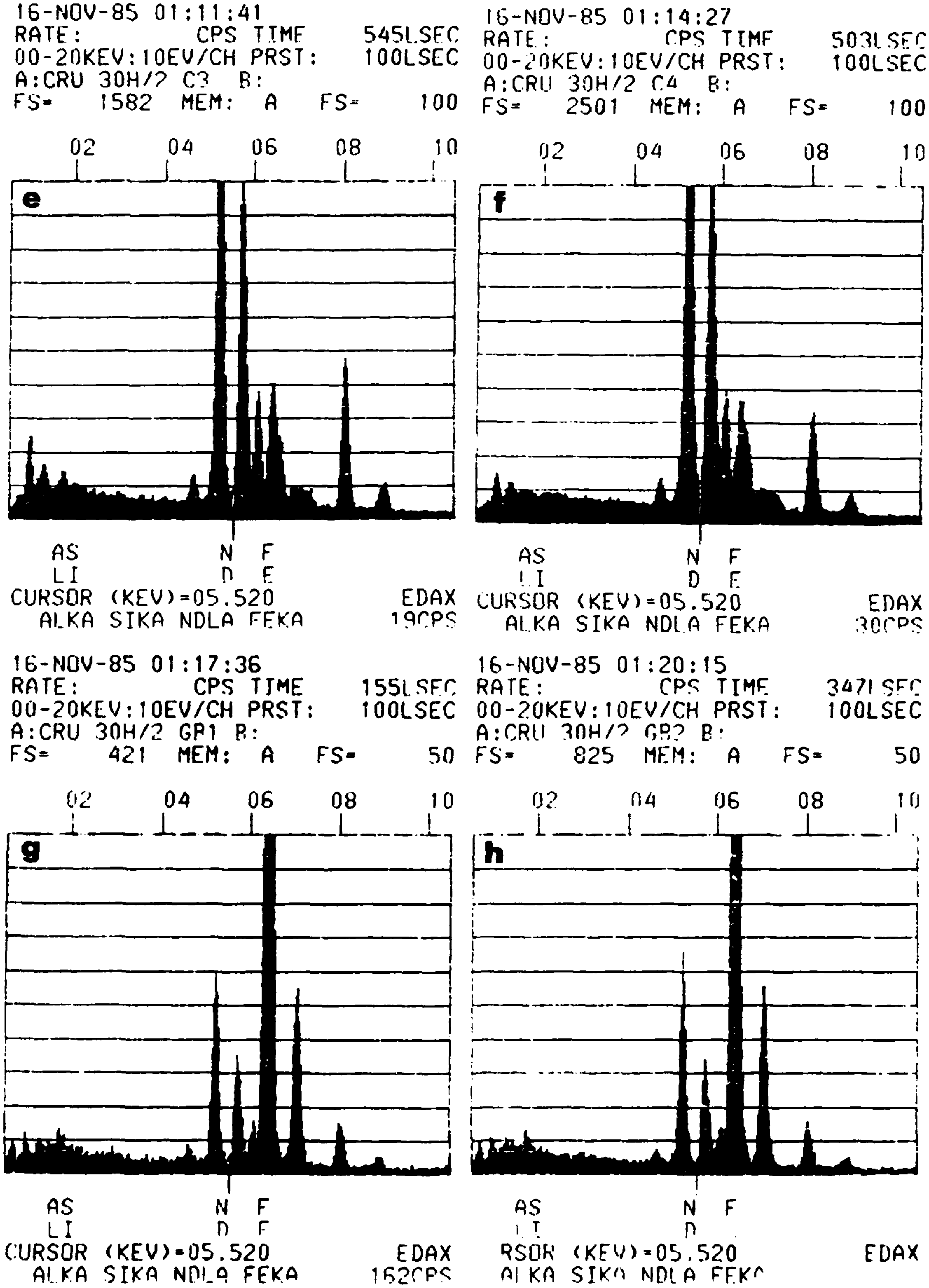

```
16-NOV-85 01:11:41
RATE:          CPS TIME     545LSEC
00-20KEV:10EV/CH PRST:      100LSEC
A:CRU 30H/2 C3  B:
FS=   1582  MEM:  A   FS=       100

AS                N  F
LI                D  E
CURSOR (KEV)=05.520            EDAX
  ALKA SIKA NDLA FEKA          19CPS
```

```
16-NOV-85 01:14:27
RATE:          CPS TIME     503LSEC
00-20KEV:10EV/CH PRST:      100LSEC
A:CRU 30H/2 C4  B:
FS=   2501  MEM:  A   FS=       100

AS                N  F
LI                D  E
CURSOR (KEV)=05.520            EDAX
  ALKA SIKA NDLA FEKA          30CPS
```

```
16-NOV-85 01:17:36
RATE:          CPS TIME     155LSEC
00-20KEV:10EV/CH PRST:      100LSEC
A:CRU 30H/2 GP1 B:
FS=    421  MEM:  A   FS=        50

AS                N  F
LI                D  F
CURSOR (KEV)=05.520            EDAX
  ALKA SIKA NDLA FEKA         162CPS
```

```
16-NOV-85 01:20:15
RATE:          CPS TIME     347LSEC
00-20KEV:10EV/CH PRST:      100LSEC
A:CRU 30H/2 GP2 B:
FS=    825  MEM:  A   FS=        50

AS                N  F
LI                D
 RSOR (KEV)=05.520             EDAX
  ALKA SIKA NDLA FEK
```

Fig.12: Energy dispersive X-ray spectra taken from the CRU 30H magnet.

Fig.13: Electron micrograph showing the precipitation of a B-phase. at the grain boundary junction of hard magnetic grains

Fig.14: Electron micrograph showing the disordered B-phase

Fig.15: Electron micrograph showing a grain boundary layer phase. separating two hard magnetic grains. An increased Si-content is found by at the grain boundary region.

show the X-ray spectrum of the Nd-rich phase C with about 16 at% Fe and 84 at% Nd. Comparing the results obtained by X-ray microanalysis of the "CRUMAX 30H" magnet with the ones of the "NEOMAX 35" magnet, instead of chlorine traces of phosphorus and sulfur were detected, especially in some C-phase regions, in the dysposium containing, highest coercivity "CRUMAX 30H" magnet.

In cooperation with HITACHI Metals Ltd., Japan, we have undertaken a systematic study of the microstrucutre in order to determine the influence of alloying small amounts of aluminium and of changing the heat treatments (12) on the magnetic hardness of non-dysprosium and dysprosium containing magnet materials. These investigations have not finished yet and the preliminary results of the metallographic and analytical microscope investigations show a similar microstructure in all of the magnet samples with an average grain size of about 31μm^2 (Fig.10). More than 100 grains and precipitates were analyzed by X-ray microanalysis, and it should be mentioned that no impurities containing chlorine, phosphorus or chlorine were found in the X-ray spectra of the different phases (Fig.16-19). This results from using high-purity raw materials for the preparation of the magnets.

More or less small amounts of silicon were found in all of the phases A,B and C. In the hard magnetic 2:14:1-borride phase there is a strong gradient of the silicon content from the centre of the grain towards the grain boundary. An increased amount of silicon is found in or near the grain boundary regions. High resolution electron microscopy of grain boundaries in sintered Nd-Fe-B magnets by Hiraga et al. (19) show a b.c.c. grain boundary layer phase. But it should also be mentioned that only a part of hard magnetic grains is separated by such a layer phase. We found that many grain boundaries (especially between grains within one particle after milling) did not show an interphase layer. The high resolution electron micrograph of Fig.20 shows a large angle (~40°) grain boundary without no layer phase and separating two hard magnetic grains (20).

By Lorentz electron microscopic investigations we found a strong domain wall pinning at grain boundaries (Fig.21), indicating a low domain wall energy and therefore a region of a low magnetocrystalline anisotropy near grain boundaries with a layer phase. Until know it was assumed that the boride phase B as well as the Nd-rich phase

Table 6: CHEMICAL COMPOSITION

in at %

HIT 1-13	Fe/Nd	Fe/Al	Fe/Si	(Fe+Si+Al)/Nd	Fe/Cl	Fe/S	Nd/Fe	Nd/Dy	Nd/S
A1	7.19		255						
A2	7.04	-	70.5			282			40.1
A3	6.81		70.1						
B1	4.44		637						
C1	0.85						1.16		
C2	0.54		39.2				1.84		
C3	0.42						2.33		
C4	0.22		40.5				4.38		
C5	0.28						3.50		
GB1	6.87		15.7			40.2			5.86

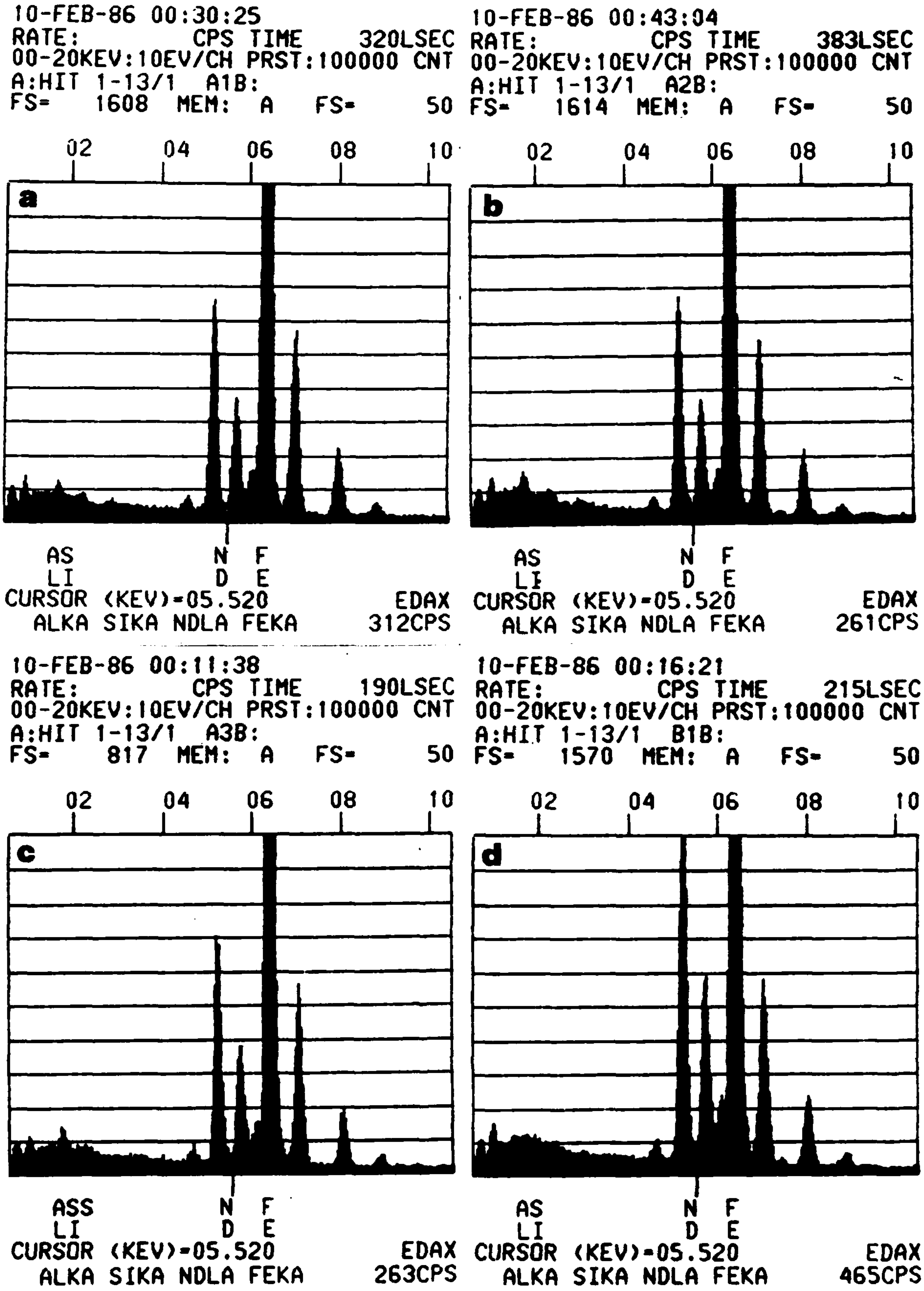

```
10-FEB-86 00:30:25
RATE:           CPS TIME    320LSEC
00-20KEV:10EV/CH PRST:100000 CNT
A:HIT 1-13/1  A1B:
FS=    1608  MEM:  A    FS=      50

   AS           N  F
   LI           D  E
CURSOR (KEV)=05.520          EDAX
  ALKA SIKA NDLA FEKA      312CPS
```

```
10-FEB-86 00:43:04
RATE:           CPS TIME    383LSEC
00-20KEV:10EV/CH PRST:100000 CNT
A:HIT 1-13/1  A2B:
FS=    1614  MEM:  A    FS=      50

   AS           N  F
   LI           D  E
CURSOR (KEV)=05.520          EDAX
  ALKA SIKA NDLA FEKA      261CPS
```

```
10-FEB-86 00:11:38
RATE:           CPS TIME    190LSEC
00-20KEV:10EV/CH PRST:100000 CNT
A:HIT 1-13/1  A3B:
FS=    817   MEM:  A    FS=      50

   ASS          N  F
   LI           D  E
CURSOR (KEV)=05.520          EDAX
  ALKA SIKA NDLA FEKA      263CPS
```

```
10-FEB-86 00:16:21
RATE:           CPS TIME    215LSEC
00-20KEV:10EV/CH PRST:100000 CNT
A:HIT 1-13/1  B1B:
FS=    1570  MEM:  A    FS=      50

   AS           N  F
   LI           D  E
CURSOR (KEV)=05.520          EDAX
  ALKA SIKA NDLA FEKA      465CPS
```

Fig.16: (continued).

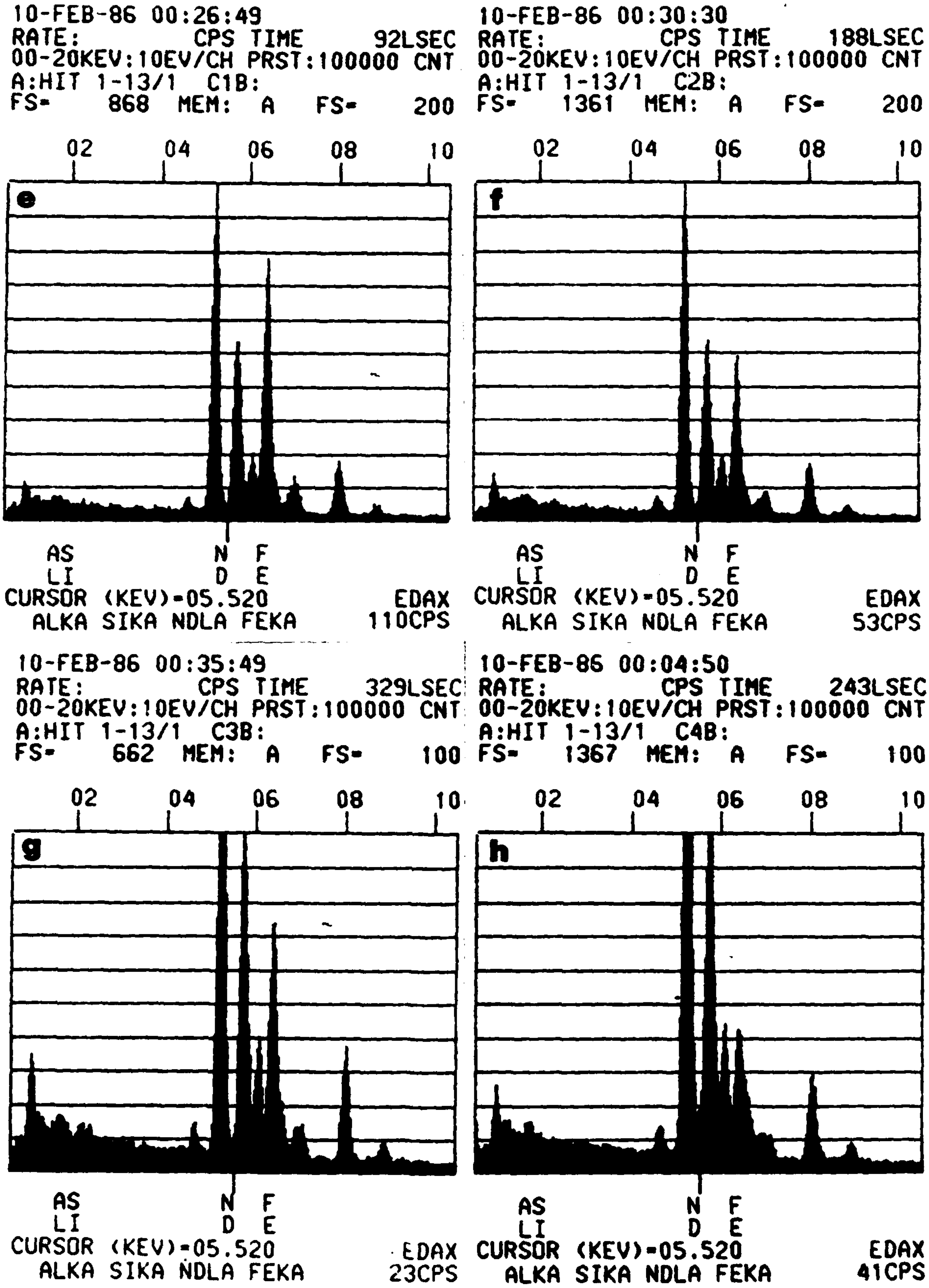

```
10-FEB-86 00:26:49
RATE:          CPS TIME      92LSEC
00-20KEV:10EV/CH PRST:100000 CNT
A:HIT 1-13/1  C1B:
FS-     868  MEM:  A    FS-     200
CURSOR (KEV)-05.520             EDAX
  ALKA SIKA NDLA FEKA         110CPS
```

```
10-FEB-86 00:30:30
RATE:          CPS TIME     188LSEC
00-20KEV:10EV/CH PRST:100000 CNT
A:HIT 1-13/1  C2B:
FS-    1361  MEM:  A    FS-     200
CURSOR (KEV)-05.520             EDAX
  ALKA SIKA NDLA FEKA          53CPS
```

```
10-FEB-86 00:35:49
RATE:          CPS TIME     329LSEC
00-20KEV:10EV/CH PRST:100000 CNT
A:HIT 1-13/1  C3B:
FS-     662  MEM:  A    FS-     100
CURSOR (KEV)-05.520             EDAX
  ALKA SIKA NDLA FEKA          23CPS
```

```
10-FEB-86 00:04:50
RATE:          CPS TIME     243LSEC
00-20KEV:10EV/CH PRST:100000 CNT
A:HIT 1-13/1  C4B:
FS-    1367  MEM:  A    FS-     100
CURSOR (KEV)-05.520             EDAX
  ALKA SIKA NDLA FEKA          41CPS
```

Fig.16: (continued).

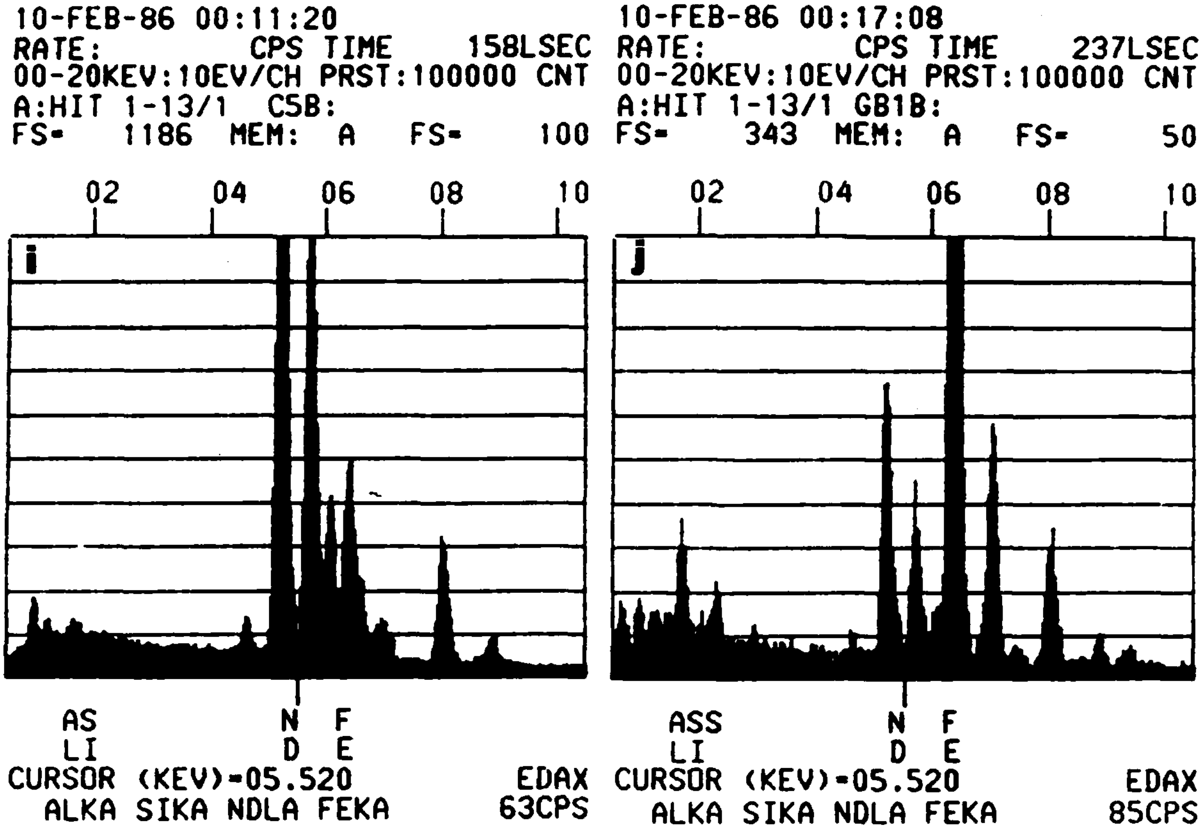

```
10-FEB-86 00:11:20
RATE:          CPS TIME     158LSEC
00-20KEV:10EV/CH PRST:100000 CNT
A:HIT 1-13/1  C5B:
FS=   1186  MEM:  A    FS=     100
```

```
AS            N  F
LI            D  E
CURSOR (KEV)=05.520          EDAX
  ALKA SIKA NDLA FEKA        63CPS
```

```
10-FEB-86 00:17:08
RATE:          CPS TIME     237LSEC
00-20KEV:10EV/CH PRST:100000 CNT
A:HIT 1-13/1 GB1B:
FS=     343  MEM:  A    FS=     50
```

```
ASS           N  F
LI            D  E
CURSOR (KEV)=05.520          EDAX
  ALKA SIKA NDLA FEKA        85CPS
```

Fig.16:Energy dispersive X-ray spectra taken from the HIT 1-13 magnet.

Table 7: CHEMICAL COMPOSITION

in at %

HIT 4-13	Fe/Nd	Fe/Al	Fe/Si	Fe+Si+Al/Nd	Fe/Cl	Fe/P+S	Nd/Fe	Nd/Dy	Nd/CL
A1	6.79		89.7						
A2	6.14	-	85.3						
A3	6.58	268	49.8	6.74					
A4	6.39		59.4						
B1	3.40		14.8						
B2	4.28		120						
C1	0.22		3.36				4.38		
C2	0.28		3.97				3.52		
C3	0.16		5.66				6.01		
GB1	6.30		64.6						
GB2	6.34	508	60.8	6.45					

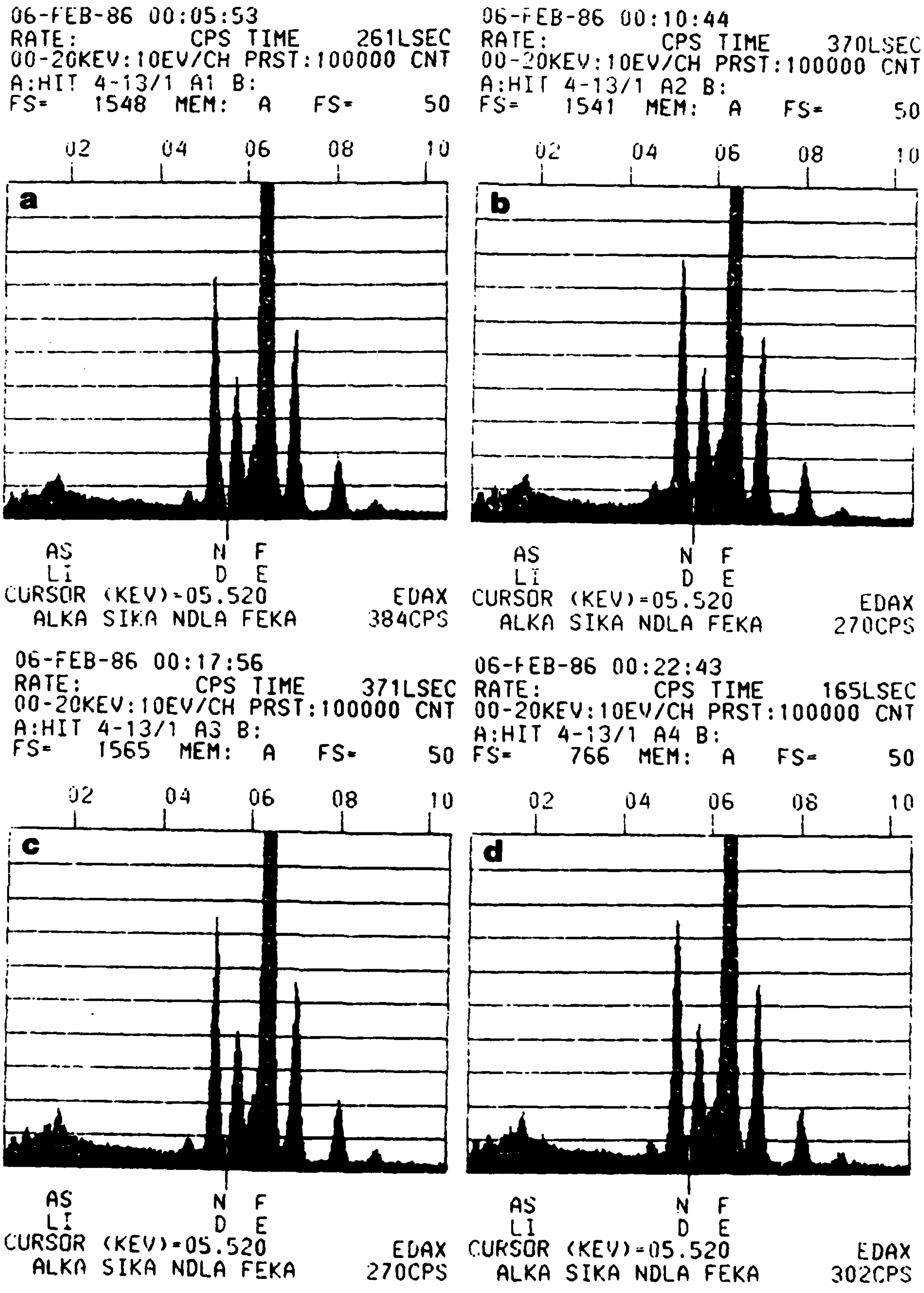

```
06-FEB-86 00:05:53
RATE:          CPS TIME     261LSEC
00-20KEV:10EV/CH PRST:100000 CNT
A:HIT 4-13/1 A1 B:
FS=    1548  MEM:  A    FS=      50
CURSOR (KEV)=05.520          EDAX
  ALKA SIKA NDLA FEKA       384CPS
```

```
06-FEB-86 00:10:44
RATE:          CPS TIME     370LSEC
00-20KEV:10EV/CH PRST:100000 CNT
A:HIT 4-13/1 A2 B:
FS=    1541  MEM:  A    FS=      50
CURSOR (KEV)=05.520          EDAX
  ALKA SIKA NDLA FEKA       270CPS
```

```
06-FEB-86 00:17:56
RATE:          CPS TIME     371LSEC
00-20KEV:10EV/CH PRST:100000 CNT
A:HIT 4-13/1 A3 B:
FS=    1565  MEM:  A    FS=      50
CURSOR (KEV)=05.520          EDAX
  ALKA SIKA NDLA FEKA       270CPS
```

```
06-FEB-86 00:22:43
RATE:          CPS TIME     165LSEC
00-20KEV:10EV/CH PRST:100000 CNT
A:HIT 4-13/1 A4 B:
FS=    766  MEM:  A    FS=      50
CURSOR (KEV)=05.520          EDAX
  ALKA SIKA NDLA FEKA       302CPS
```

Fig.17: (continued).

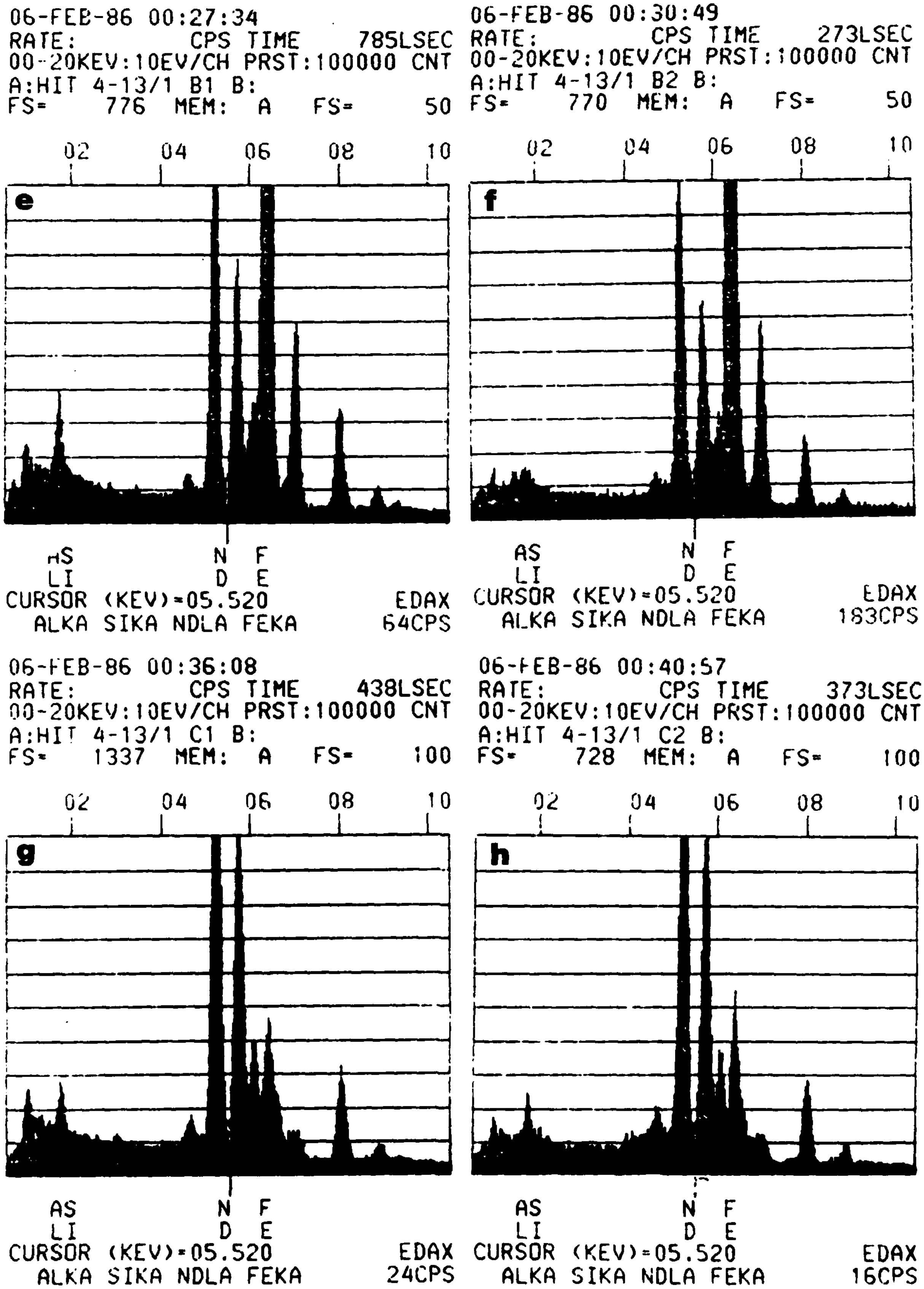

```
06-FEB-86 00:27:34
RATE:          CPS TIME      785LSEC
00-20KEV:10EV/CH PRST:100000 CNT
A:HIT 4-13/1 B1 B:
FS=    776  MEM:  A   FS=       50
```

```
CURSOR (KEV)=05.520           EDAX
  ALKA SIKA NDLA FEKA        64CPS
```

```
06-FEB-86 00:30:49
RATE:          CPS TIME      273LSEC
00-20KEV:10EV/CH PRST:100000 CNT
A:HIT 4-13/1 B2 B:
FS=    770  MEM:  A   FS=       50
```

```
CURSOR (KEV)=05.520           EDAX
  ALKA SIKA NDLA FEKA       183CPS
```

```
06-FEB-86 00:36:08
RATE:          CPS TIME      438LSEC
00-20KEV:10EV/CH PRST:100000 CNT
A:HIT 4-13/1 C1 B:
FS=   1337  MEM:  A   FS=      100
```

```
CURSOR (KEV)=05.520           EDAX
  ALKA SIKA NDLA FEKA        24CPS
```

```
06-FEB-86 00:40:57
RATE:          CPS TIME      373LSEC
00-20KEV:10EV/CH PRST:100000 CNT
A:HIT 4-13/1 C2 B:
FS=    728  MEM:  A   FS=      100
```

```
CURSOR (KEV)=05.520           EDAX
  ALKA SIKA NDLA FEKA        16CPS
```

Fig.17: (continued).

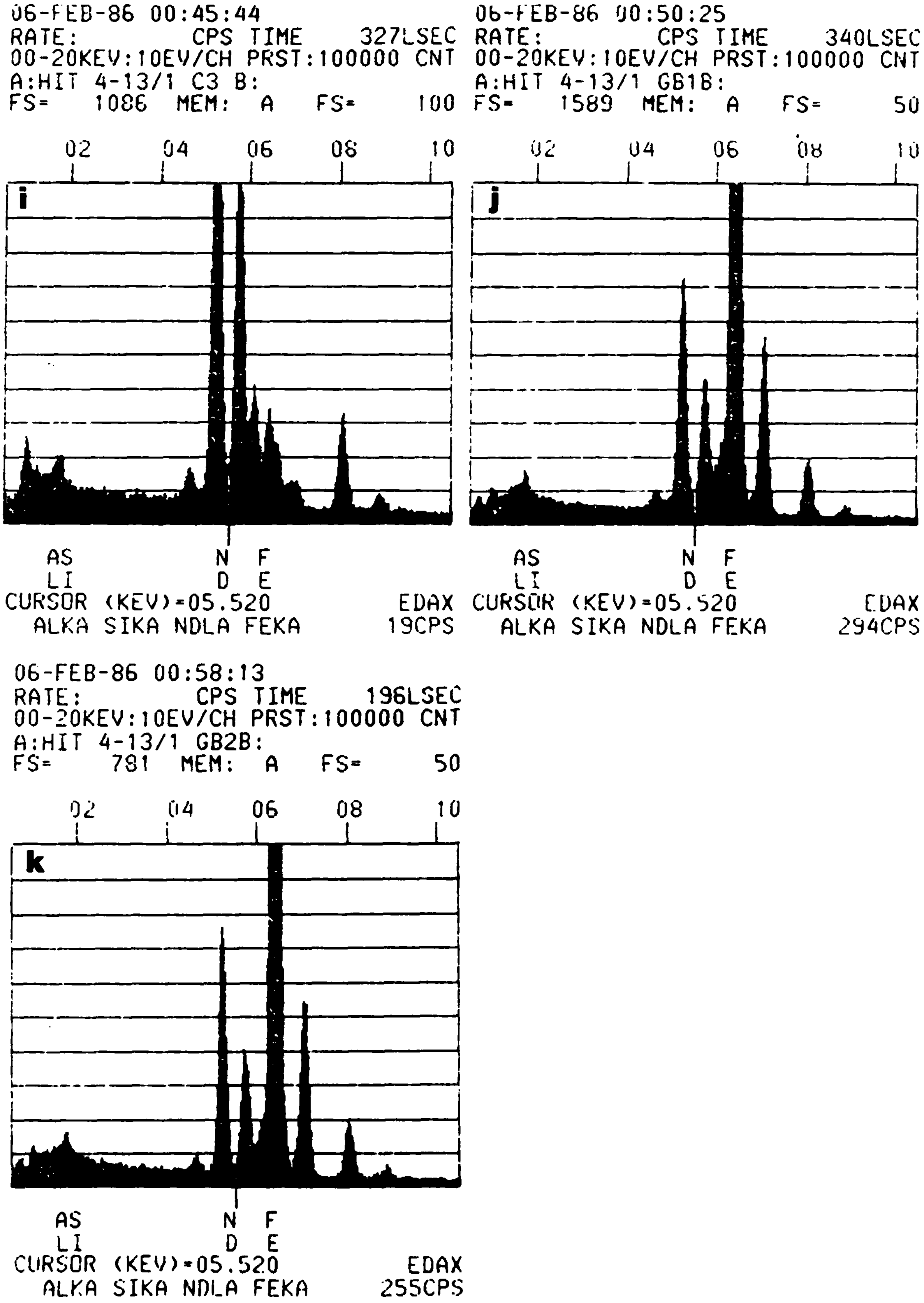

```
06-FEB-86 00:45:44
RATE:          CPS TIME    327LSEC
00-20KEV:10EV/CH PRST:100000 CNT
A:HIT 4-13/1 C3 B:
FS=   1086  MEM:  A   FS=      100
```

```
CURSOR (KEV)=05.520           EDAX
  ALKA SIKA NDLA FEKA        19CPS
```

```
06-FEB-86 00:50:25
RATE:          CPS TIME    340LSEC
00-20KEV:10EV/CH PRST:100000 CNT
A:HIT 4-13/1 GB1B:
FS=   1589  MEM:  A   FS=       50
```

```
CURSOR (KEV)=05.520           EDAX
  ALKA SIKA NDLA FEKA       294CPS
```

```
06-FEB-86 00:58:13
RATE:          CPS TIME    196LSEC
00-20KEV:10EV/CH PRST:100000 CNT
A:HIT 4-13/1 GB2B:
FS=    781  MEM:  A   FS=       50
```

```
CURSOR (KEV)=05.520           EDAX
  ALKA SIKA NDLA FEKA       255CPS
```

Fig.17: Energy dispersive X-ray spectra taken from the HIT-4-13 magnet.

Table 8: CHEMICAL COMPOSITION

in at %

HIT A1-11	Fe/Nd	Fe/Al	Fe/Si	Fe+Si+Al/Nd	Fe/Cl	Fe/S	Nd/Fe	Nd/Dy	Nd/S
A1	8.09		36.9						
A2	8.86	-	661						
B1	4.30		29.9			269			70.3
C1	0.16				39.9		5.98	2.06	
C2	0.14						7.00	7.00	

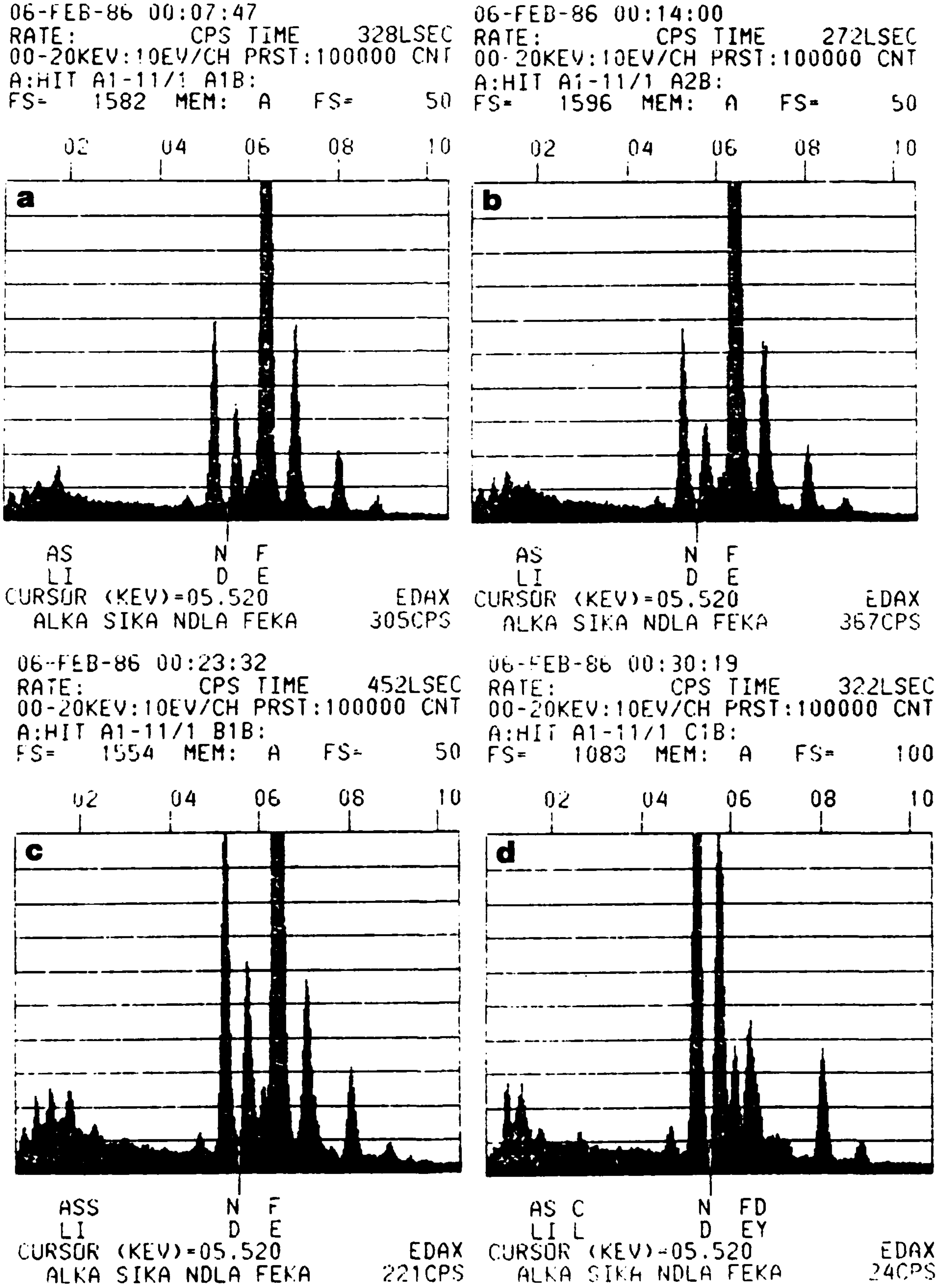

```
06-FEB-86 00:07:47
RATE:              CPS TIME     328LSEC
00-20KEV:10EV/CH PRST:100000 CNT
A:HIT A1-11/1 A1B:
FS=    1582  MEM:   A    FS=        50

   AS                    N  F
   LI                    D  E
CURSOR (KEV)=05.520               EDAX
  ALKA SIKA NDLA FEKA            305CPS
```

```
06-FEB-86 00:14:00
RATE:              CPS TIME     272LSEC
00-20KEV:10EV/CH PRST:100000 CNT
A:HIT A1-11/1 A2B:
FS=    1596  MEM:   A    FS=        50

   AS                    N  F
   LI                    D  E
CURSOR (KEV)=05.520               EDAX
  ALKA SIKA NDLA FEKA            367CPS
```

```
06-FEB-86 00:23:32
RATE:              CPS TIME     452LSEC
00-20KEV:10EV/CH PRST:100000 CNT
A:HIT A1-11/1 B1B:
FS=    1554  MEM:   A    FS=        50

   ASS                   N  F
   LI                    D  E
CURSOR (KEV)=05.520               EDAX
  ALKA SIKA NDLA FEKA            221CPS
```

```
06-FEB-86 00:30:19
RATE:              CPS TIME     322LSEC
00-20KEV:10EV/CH PRST:100000 CNT
A:HIT A1-11/1 C1B:
FS=    1083  MEM:   A    FS=       100

   AS C                  N  FD
   LI L                  D  EY
CURSOR (KEV)=05.520               EDAX
  ALKA SIKA NDLA FEKA             24CPS
```

Fig.18: (continued).

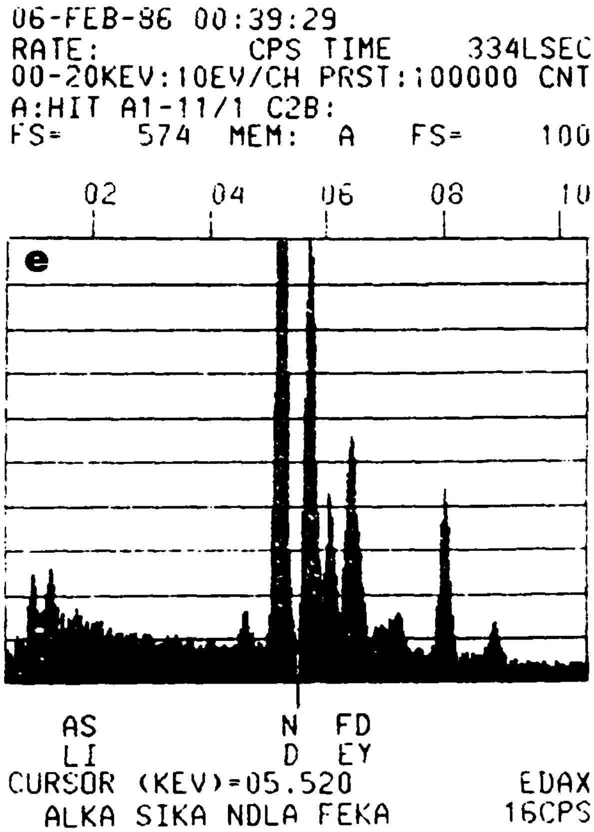

```
06-FEB-86 00:39:29
RATE:          CPS TIME     334LSEC
00-20KEV:10EV/CH PRST:100000 CNT
A:HIT A1-11/1 C2B:
FS=     574  MEM:  A    FS=     100
```

```
CURSOR (KEV)=05.520         EDAX
  ALKA SIKA NDLA FEKA       16CPS
```

Fig.18: Energy dispersive X-ray spectra taken from the HIT A1-11 magnet.

Table 9: CHEMICAL COMPOSITION

in at %

HIT B4-4	Fe/Nd	Fe/Al	Fe/Si	Fe+Si+Al/Nd	Fe/Cl	Fe/P+S	Nd/Fe	Nd/Oy	Nd/Cl
A1	8.37		22.6						
A2	7.67	-129	90.2						
A3	7.14	149	69.1						
A4	7.68	262	334						
A5	7.88	844	84.4						
A6	8.11	53.7	36.7						
B1	4.43	196	268						
B2	1.48		406						
C1							2.33	3.5	
C2							7.00	7.00	
GB1	7.83	63.2	11.9						

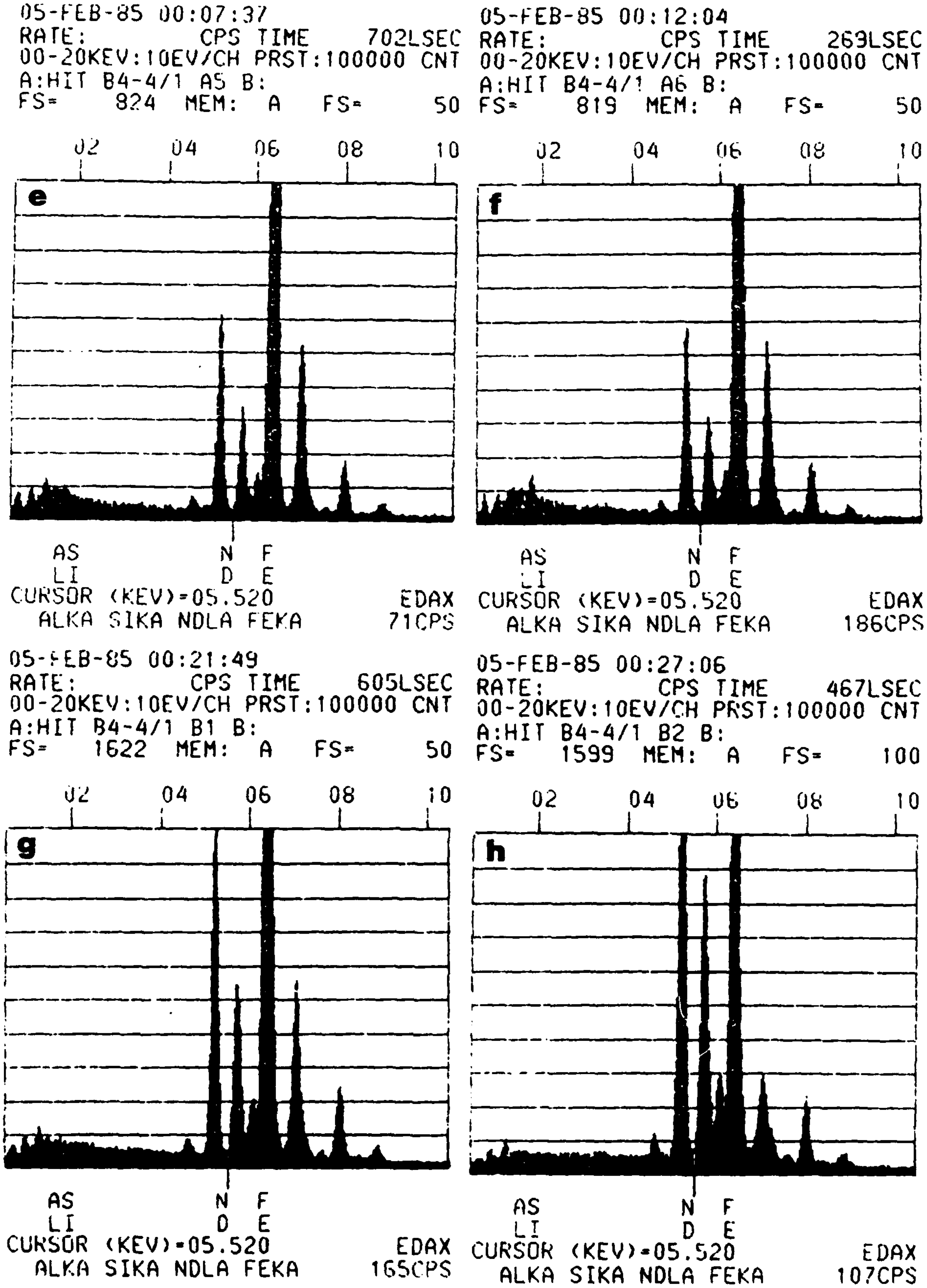

```
05-FEB-85 00:07:37                   05-FEB-85 00:12:04
RATE:          CPS TIME    702LSEC   RATE:          CPS TIME    263LSEC
00-20KEV:10EV/CH PRST:100000 CNT     00-20KEV:10EV/CH PRST:100000 CNT
A:HIT B4-4/1 A5 B:                   A:HIT B4-4/1 A6 B:
FS=    824  MEM:  A    FS=      50   FS=    819  MEM:  A    FS=      50
```

```
  AS            N  F                   AS            N  F
  LI            D  E                   LI            D  E
CURSOR (KEV)=05.520        EDAX      CURSOR (KEV)=05.520        EDAX
  ALKA SIKA NDLA FEKA      71CPS       ALKA SIKA NDLA FEKA      186CPS
05-FEB-85 00:21:49                   05-FEB-85 00:27:06
RATE:          CPS TIME    605LSEC   RATE:          CPS TIME    467LSEC
00-20KEV:10EV/CH PRST:100000 CNT     00-20KEV:10EV/CH PRST:100000 CNT
A:HIT B4-4/1 B1 B:                   A:HIT B4-4/1 B2 B:
FS=   1622  MEM:  A    FS=      50   FS=   1599  MEM:  A    FS=     100
```

```
  AS            N  F                   AS            N  F
  LI            D  E                   LI            D  E
CURSOR (KEV)=05.520        EDAX      CURSOR (KEV)=05.520        EDAX
  ALKA SIKA NDLA FEKA      165CPS      ALKA SIKA NDLA FEKA      107CPS
```

Fig.19: (continued).

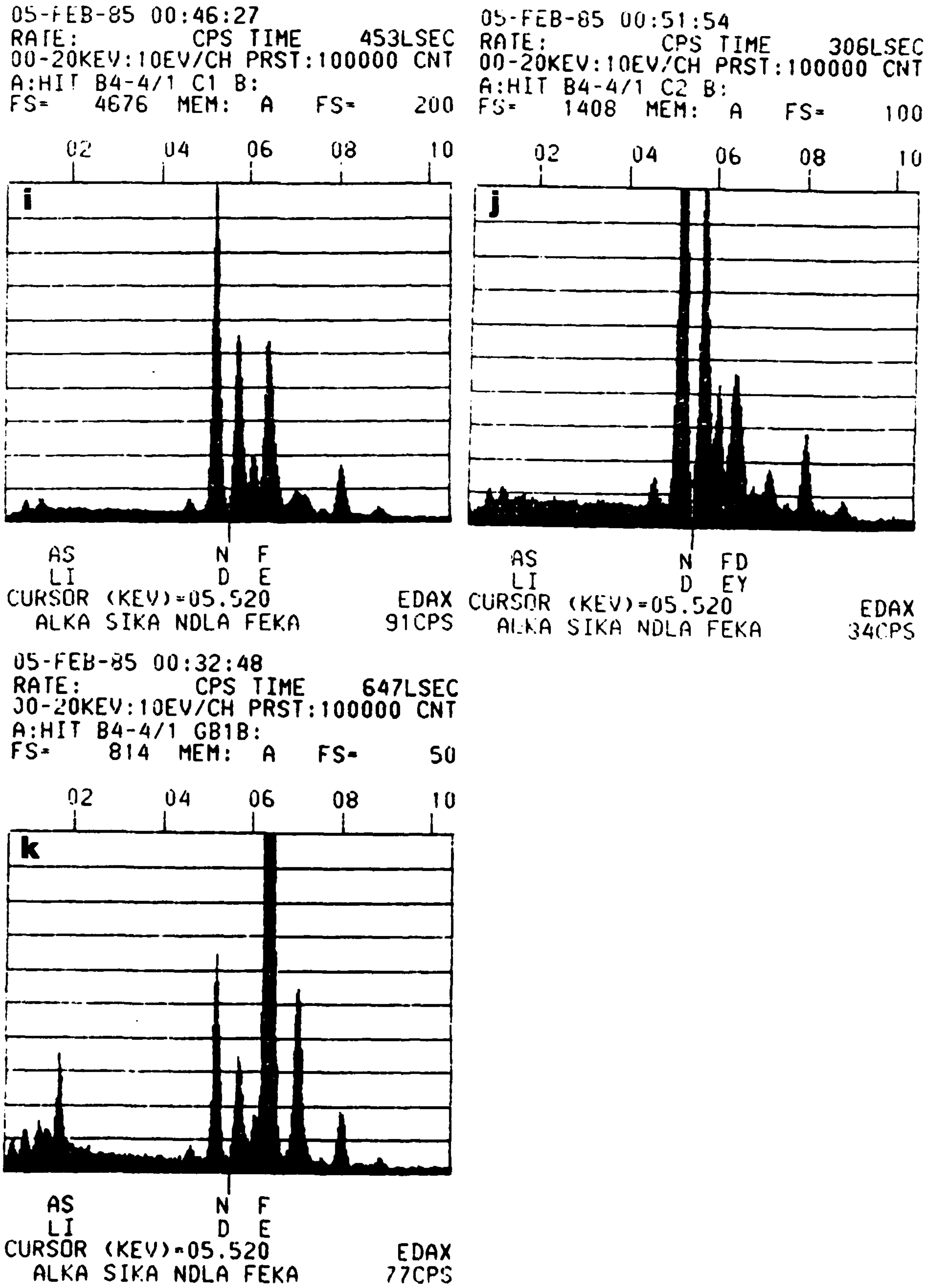

```
05-FEB-85 00:46:27
RATE:          CPS TIME     453LSEC
00-20KEV:10EV/CH PRST:100000 CNT
A:HIT B4-4/1 C1 B:
FS=   4676  MEM:  A    FS=     200

   AS             N  F
   LI             D  E
CURSOR (KEV)=05.520         EDAX
  ALKA SIKA NDLA FEKA       91CPS
```

```
05-FEB-85 00:51:54
RATE:          CPS TIME     306LSEC
00-20KEV:10EV/CH PRST:100000 CNT
A:HIT B4-4/1 C2 B:
FS=   1408  MEM:  A    FS=     100

   AS             N  FD
   LI             D  EY
CURSOR (KEV)=05.520         EDAX
  ALKA SIKA NDLA FEKA       34CPS
```

```
05-FEB-85 00:32:48
RATE:          CPS TIME     647LSEC
00-20KEV:10EV/CH PRST:100000 CNT
A:HIT B4-4/1 GB1B:
FS=    814  MEM:  A    FS=      50

   AS             N  F
   LI             D  E
CURSOR (KEV)=05.520         EDAX
  ALKA SIKA NDLA FEKA       77CPS
```

Fig.19: Energy dispersive X-ray spectra taken from the HIT B4-4 magnet.

Fig.20: High resolution electron micrograph showing a grain boundary separating two hard magnetic grains. No layer phase is detected.

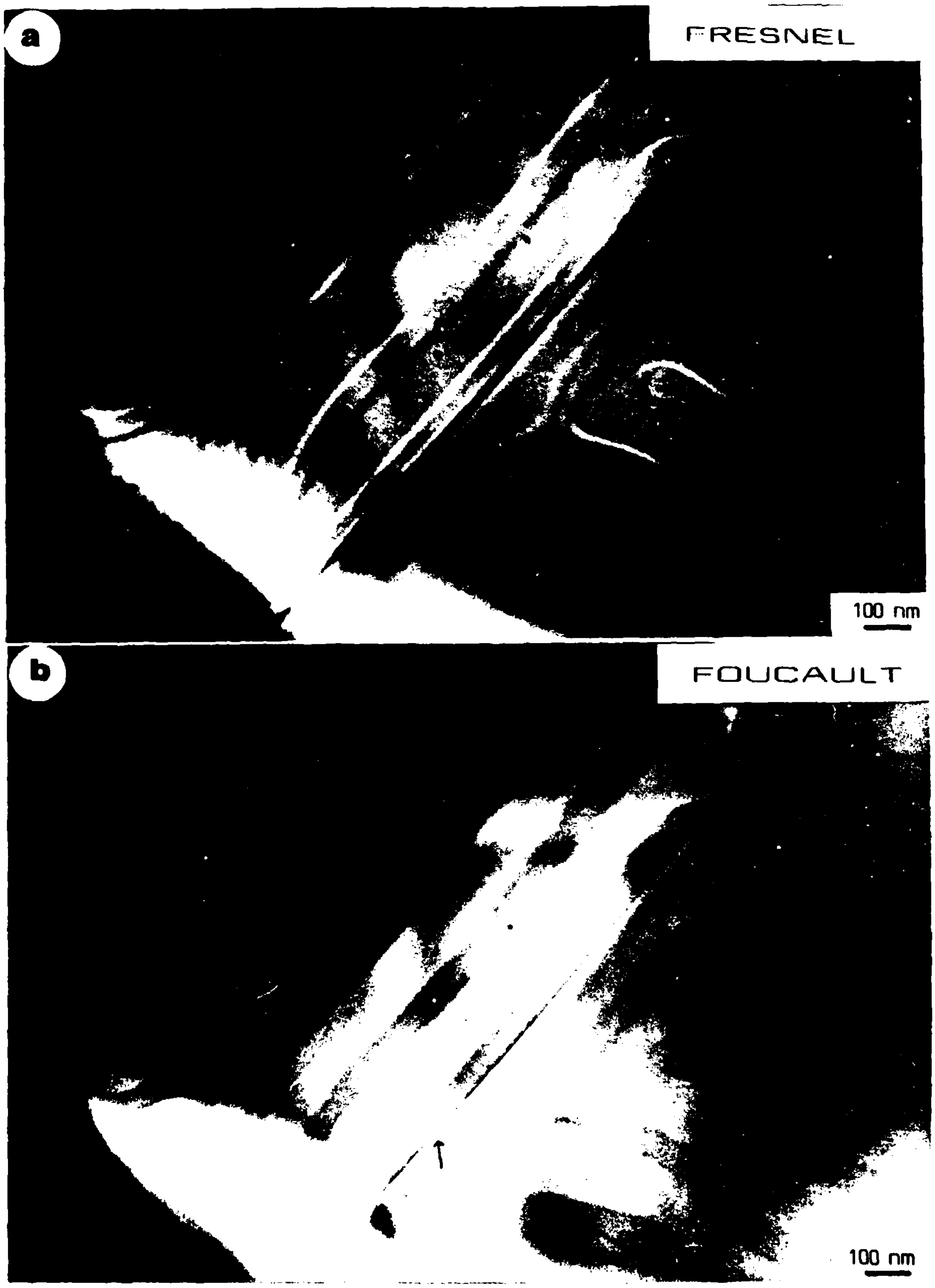

Fig.21: Lorentz electron micrographs showing a strong domain wall pinning at the grain boundary regions of the hard magnetic grains.

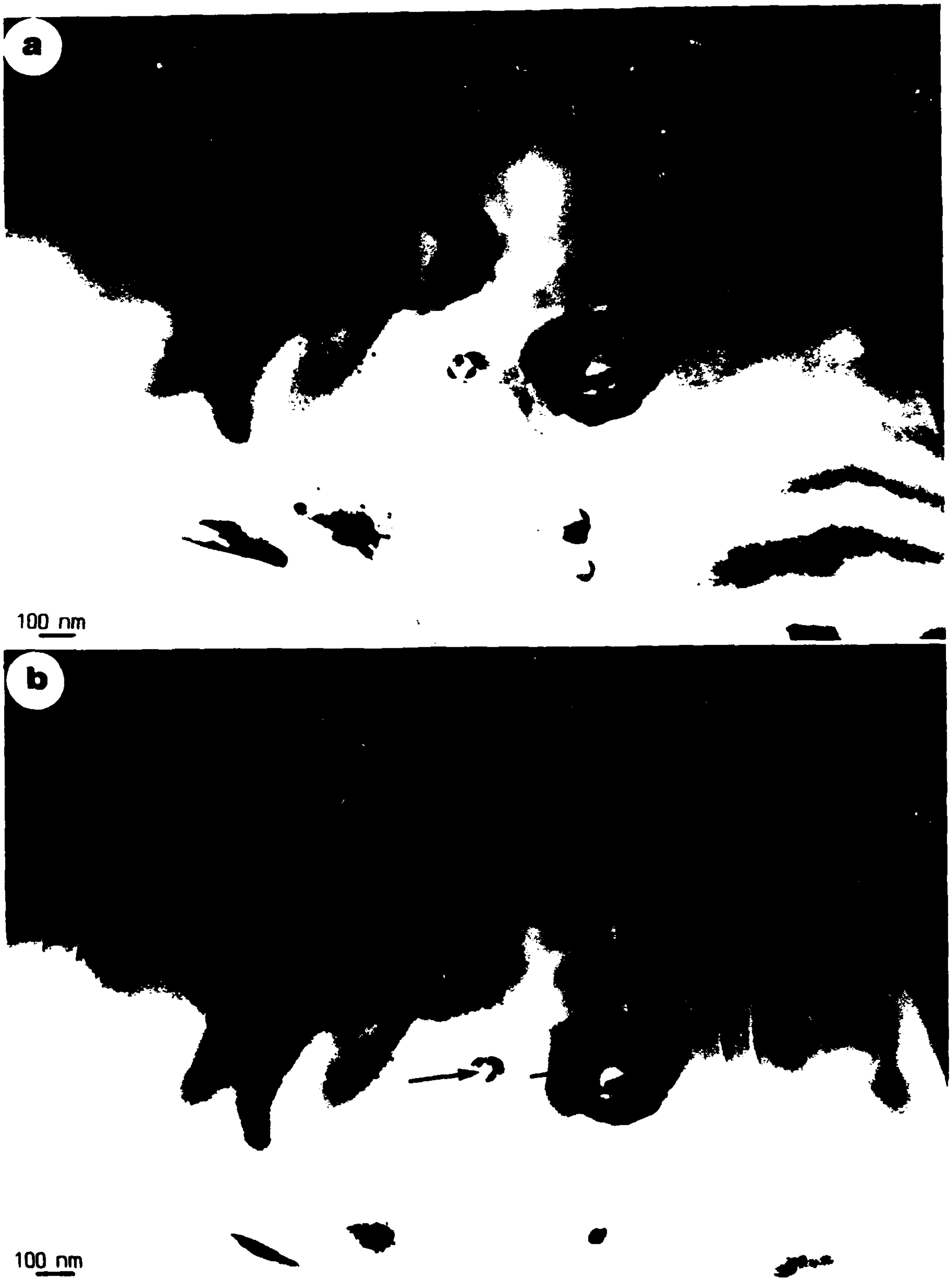

Fig.22: Precipitates within the grain interior of the hardmagnetic grain limit the magnetic hardness of the magnet. Magnetic domain walls (marked by arrows) are visible within the precipitates of the B-phase type. (a) is in focus and (b) is a defocused Fresnel micrograph.

do not show spontaneous magnetism at room temperature, but we found (20) a domain wall structure within small $Nd_{1+\varepsilon}Fe_4B_4$-inclusions within the hard magnetic grains of phase A (Fig.22). Such inclusions are centres for the nucleation of reversed domains. After the abrupt reversal of the magnetization in the individual grains with soft magnetic precipitates, the further expansion of the reversed magnetic domains can be hindered by the pinning of domain walls at grain boundary regions. Finally, the coercivity of the individual Nd-Fe-B magnet strongly depends on the processing parameters (milling and anealing) and is directly correlated to the microstructure and magnetocrystalline anisotropy of the material.

(6) FUTURE ELECTRON MICROSCOPE INVESTIGATIONS

Future investigations of rare earth-iron permanent magnet materials are necessary for the understanding of the microstructure and therefore for the understanding of the coercivity mechanism. Since very high coercivities at room temperature increase the operation temperature of the permanent magnet containing device, special emphasis must be laid on the factors leading to high coercivities. Especially the effect of alloying of small amounts of transition elements or of variing the post-sintering anealing parameters on the microstructure must be carefully studied. Besides the sintered magnetic materials also magnets based on micro-crystalline alloys should be investigated and compared. We intend to continue the analytical electron microscope investigation together with high resolution electron microsocopy and Lorentz electron microscopy of various rare earth-iron permanent materials.

References

1 J. Fidler and P. Skalicky, Metallurgie in print.

2 H. Kronmüller, Proc. VII. Int. Workshop RE-Co Perm. Magn., p.339, Beijing, 1983.

3 K.D. Durst and H. Kronmüller, 4th Int. Symposium on magnetic Anisotropy and Coercivity in rare earth transition metals alloys, Dayton, (ed. K.Strnat), 1985, p. 725.

4 J. Fidler and P. Skalicky, Mikrochimica Acta (Wien), Suppl.10, 315 (1983).

5 J. Fidler, P. Skalicky and F. Rothwarf, Microchimia Act (Wien), Suppl.11, 371 (1985).

6 J. Fidler, R. Grössinger, H. Kirchmayr and P.Skalicky Annual Report (1983) United States Army, Contract No. 37-82-C-0050.

7 J. Fidler, R. Grössinger, H. Kirchmayr and P.Skalicky, Annual Report (1985) United States Army, Contract No. 45-84-C-0010.

8 M. Sagawa, S. Fujimura, H. Yamamoto, Y. Matsuura and K. Hiraga, IEEE Trans. Magn., MAG-20, 1584 (1984).

9 K.S.V.L. Narasimhan, Intermag Conference 1984,Hamburg.

10 M. Sagawa, S. Fujimura, N. Togawa, H. Yamamoto and Y. Matsuura, J. Appl. Phys., 55, 2083 (1984).

11 R.W. Lee, E.G. Brewer and N.A. Schaffel, IEEE Trans.Magn., MAG-21, 1958 (1985).

12 M. Tokunaga, N. Meguro, M. Endoh, S. Tanigawa and H. Harada, IEEE Trans.Magn., MAG-21, 1964 (1985).

13 M. Ghandehari, Applied Physics Lett., submitted.

14 J. Fidler, IEEE Trans.Magn., MAG-21, 1955 (1985).

15 J. Fidler and Luo Yang, ibid Ref.3, p.647.

16 A. Bezinge, H.F. Braun, J. Muller and K. Yvon, Solid State Communications, 1985.

17 P. Falconnet, Report and Proceedings of a CEM Workshop, (ed. I.V. Mitchell), Brussels, 1984, p.15.

18 J. Omerod, ibid Ref.17, p. 69.

19 K. Hiraga, M. Hirabayashi, M. Sagawa and Y. Matsuura, Jap. J. Appl. Phys., 24, L30 (1985).

20 J. Fidler, J. Mat. Sci., submitted.

SECTION II

ANISOTROPY AND COERCIVITY OF Nd-Fe-B BASED MATERIALS

by

R. Grössinger, R. Krewenka, Ch. Schotzko and H. Kirchmayr

Institute for Experimental Physics
Technical University of Vienna
Karlsplatz 13, A-1040 Vienna, Austria.

1)Introduction

High quality permanent magnets are based on rare earth-3d intermetallic compounds. The large number of these compounds is reduced by the conditions which are necessary to fulfill in order to obtain a usefull material for permanent magnets. The most important intrinsic properties are:

i) A lattice with a crystallographic preferrential axis: e.g. hexagonal, rhomboedric or tetragonal.
ii) A high Curie temperature.
iii) A high saturation magnetization (especially at room temperature)
iiii)A high uniaxial anisotropy.

The most important materials which should be mentioned here are $SmCo_5$, Sm_2Co_{17} and $Nd_2Fe_{14}B$. Tablel summarises the above mentioned parameters.

Tablel: Crystallographic and magnetic parameters of R-3d compounds important for permanent magnets.

compound	lattice type	lattice const. a [Å]	c [Å]	$4\pi M_s$ (kG)	H_A[1] (kG)	T_C (K)	$_IH_C$[2] (kG)	$(BH)_{max}$[2] (MGOe)
$SmCo_5$	$CaCu_5$	4.937	3.978	11.2	290	1020	20	25
Sm_2Co_{17}	Th_2Zn_{17}	8.402	12.212	12.8	65	1195	12	30
$Nd_2Fe_{14}B$	$Nd_2Fe_{14}B$	8.756	12.185	16	75	580	10	40

1)...values at room temperature
2)...good values as published in literature (e.g.1)

The present report will be concentrated on the anisotropy and the coercivity behaviour of compounds based on Nd-Fe-B. This material had become prominent because it gives the possibilty to produce Co-free permanent magnets with the highest energy product published up to now. In this work first the properties of the basic compound $Nd_2Fe_{14}B$ will be surveyed. The theoretical background, necessary for the understanding of the tetragonal anisotropy, will be given. In order to understand the anisotropy of the Nd-sublattice the mixed crystal series $(Nd,R)_{15}Fe_{77}B_8$ (usual technical composition) were studied. For searching possible other canditates, the anisotropy of the boundary compounds $R_2Fe_{14}B$ (R...rare earth elements) were studied too. Finally a summary of the magnetic properties of R-Fe-B based technical permanent magnets will be given.

2)The magnetic properties of $Nd_2Fe_{14}B$

The hard magnetic properties of the new Nd-Fe-B permanent magnets are based on $Nd_2Fe_{14}B$, which is tetragonal and belongs to the space group $P4_2/mnm$ (2). $Nd_2Fe_{14}B$ is uniaxial at room temperature with an anisotropy field of about 75kG (3), however below 135K an easy cone appears (4). This change of the easy axis of magnetization was shown by single crystal measurements (4), by anisotropy studies (3) and also by initial susceptibility measurements (5). Due to this spinreorientation an anisotropy anomaly occurs, which is generally called a FOMP (First Order Magnetization Process) transition (6). The fundamental idea of such a transition is the occurence of additional relativ minima in the anisotropy energy surface according to the increasing importance of higher order anisotropy constants. This leads to jumps in the magnetization curve M(H) (see also Chapt.3.3). Such a behaviour was found first in $PrCo_5$(7). In $Nd_2Fe_{14}B$ a similar curiosity was detected (3,5).

3)Theoretical background

In this chapter the theoretical description of a tetragonal anisotropy, the definition of the anisotropy field H_A, the theory of the SPD-(Singular Point Detection) technique and the basic ideas of a FOMP transition will be shown. Additional a short survey of the theories correlating the anisotropy field with the coercivity will be given.

3.1)Tetragonal anisotropy

The series expansion of the anisotropy energy, generally used in this case can be written as:

$$F_A = K_1 \sin^2\theta + K_2 \sin^4\theta + K_3 \sin^4\theta \sin^2\varphi \cos^2\varphi \qquad (1)$$

θ...angle between the tetragonal axis and the magnetixation vector

φ...angle between the projection of the magnetization vector on the a,b-plane with the a-axis

It should be mentioned here, that this series expansion is only traditionary, a mathematical more correct development uses a set of orthogonal functions (e.g. spherical harmonical functions $Y_{lm}(\theta,\varphi)$. In this case F_A would follow the equation:

$$F_A = k_0^0 Y_0^0 + k_2^0 Y_2^0 + k_4^0 Y_4^0 + k_6^0 Y_6^0 + k_6^6 Y_6^6 \qquad (2)$$

The main advantage of this type of series expansion is, that in the case of a single ion anisotropy the temperature dependence of these anisotropy constants can be described analytically (8):

$$\frac{k_\ell(T)}{k_\ell(0)} = \frac{I_{\ell+1/2}(x)}{I_{1/2}(x)} \qquad (3)$$

$I_{\ell+1/2}$...modified Besselfunctions

This leads at low temperatures to the famous l(l+1) power law:

$$k_\ell(T) = k_\ell(0)\left[M(T)/M(0)\right]^{\ell(\ell+1)/2} \qquad (4)$$

Nevertheless the series expansion as given in formula (1) is the generally used one and therefore the following discussion is based on this expression, however assuming for simplicity $K_3=0$. The condition for an extremum in F_A is:

$$\partial F_A / \partial\theta = 0 \qquad (5)$$

This leads to:

$$2\sin\theta\cos\theta(K_1+2K_2\sin^2\theta)=0 \qquad (6)$$

Equation (6) has 3 solutions:

$$\begin{array}{ll} \sin\theta=0 & \theta=0 \\ \cos\theta=0 & \theta=\pi/2 \\ K_1+2K_2\sin\theta=0 & \theta=\arcsin\sqrt{(-K_1/2K_2)} \end{array} \qquad (7)$$

The condition for an easy axis of magnetization (minimum in F_A) is:

$$\partial^2F_A/\partial\theta^2>0 \qquad (8)$$

which means:

$$K_1-2(K_1-3K_2)\sin^2\theta-8K_2\sin^4\theta > 0 \qquad (9)$$

From this equation it can be concluded, that for the occurence of a certain direction of the easy axis of magnetization the following conditions have to be fulfilled:

easy c-axis	$\theta=0$	$K_1>0$
easy plane	$\theta=\pi/2$	$K_1+2K_2<0$
easy cone	$\theta=\arcsin\sqrt{(-K_1/2K_2)}$	$K_1<0$ $K_1+2K_2>0$

In table2 all conditions necessary for an easy or a hard direction of the magnetization is summarised.

Table2: Necessary conditions for the occurence of an easy or a hard direction of magnetization.

direction where an extremum in F_A exist	anisotropy field H_A 1)	*conditions for* extrem directions	
		easy	hard
c-axis	$2K_1/M_S$	$K_1>0$	$K_1<0$
basal plane	$-2(K_1+2K_2)/M_S$	$K_1+2K_2<0$	$K_1+2K_2>0$
cone with an angle $\theta=\arcsin\sqrt{(-K_1/2K_2)}$	$-2K_1(K_1+2K_2)$ K_2M_S	$K_1<0$ $K_1+2K_2>0$	$K_1>0$ $K_1+2K_2<0$

1) the definition of H_A will be given in chapt.3.2.

The values of F_A are given (assuming an easy c- axis, an easy basal plane or an easy cone):

$$F_A=0 \qquad (10)$$

$$F_A=K_1+2K_2 \qquad (11)$$

$$F_A=K_1\sin^2\theta_c+K_2\sin^4\theta_c \qquad (12)$$

If now a spinreorientation happens, at the transition the energies are equal. With this idea the equation of the boundary line for each transition can be calculated. These lines are given for a transition between the:

i) basal plane→cone: $K_1+2K_2=0$ (13)
ii) c-axis→basal plane: $K_1+K_2=0$ (14)
iii) c-axis→cone: $K_1=0$ (15)

The equations 13, 14 and 15 defines the phase diagram for the existence of the different easy axis for a tetragonal symmetry as shown in Fig.1. The different areas are characterised graphically. between the "easy c-axis" phase and the "easy plane" phase exist a metastable region.

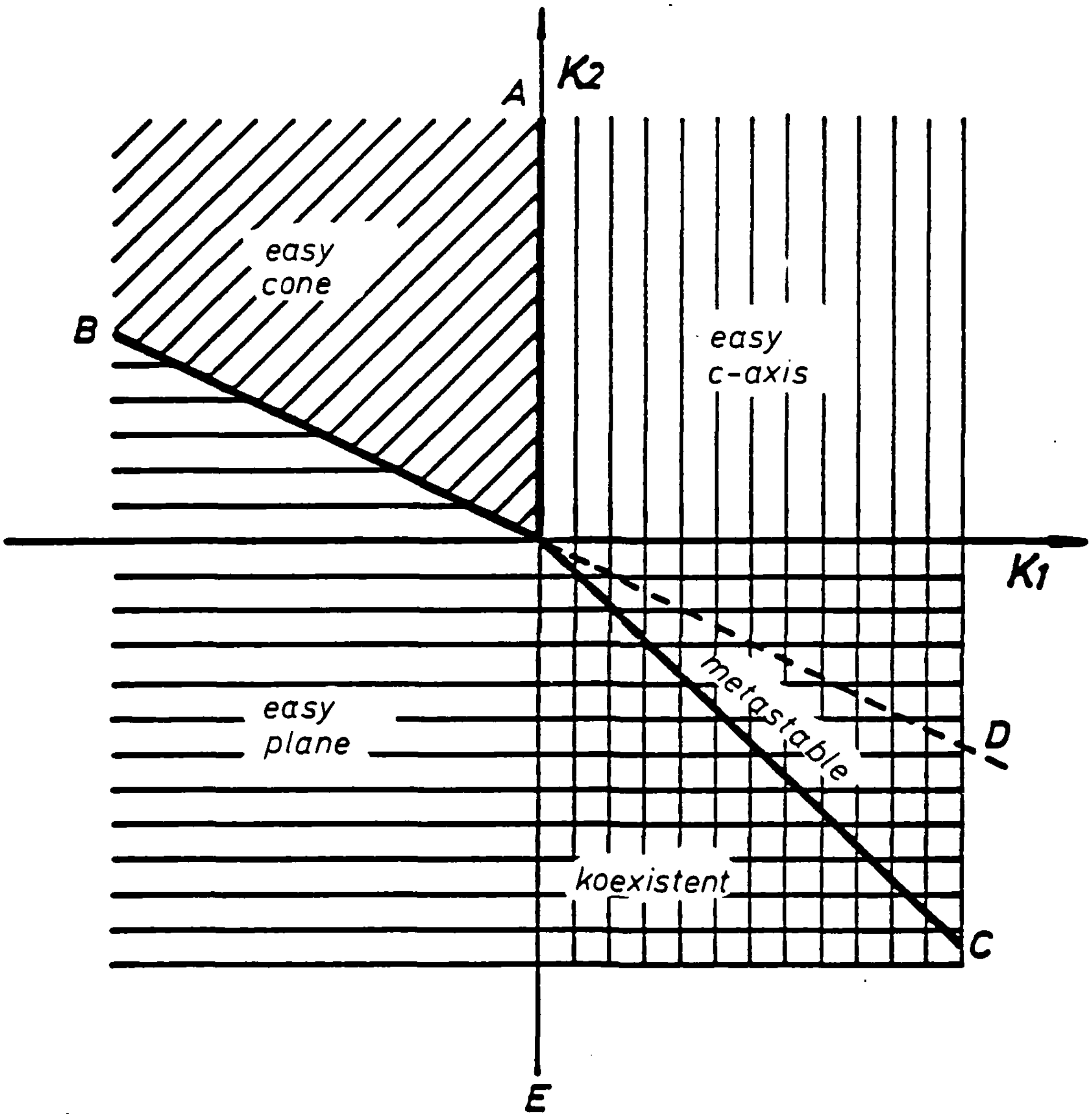

1. Phase diagram of the magnetic anisotropy of a tetragonal crystal.

3.2)Definition of the anisotropy field H_A

In the previous chapter the generally used description of the anisotropy energy was given. Another, possibly more relevant, description of the anisotropy behaviour is based on the anisotropy field H_A. Due to the confusion, which seams to exist in the definition of H_A , first the mathematical calculation leading to the anisotropy field H_A will be given.

3.2.1)Mathematical definition of H_A (tetragonal symmetry)

An external magnetic field H is assumed, which is orientated with respect to the lattice in a certain direction. The total energy is in this case:

$$F_t=F_A-M_S H\cos(\theta-\Psi) \qquad (16)$$

Ψ...angle between the field $\vec{H}$ and the c-axis
The equilibrium condition is there also described by:

$$\partial F_t/\partial\theta=0=\partial F_A/\partial\theta+M_S H\sin(\theta-\Psi) \qquad (17)$$

Formula (17) can be discussed as follows:

$M_S H\sin(\theta-\Psi)=\vec{M_S}\times\vec{H}$...torque caused by the external field.
$-\partial F_A/\partial\theta$...torque caused by the crystal anisotropy.

The different sign of both torques reflects that they compete with each other. H should cause an infinitesimal small deflection of the magnetization vector $\vec{M}$ from its equilibrium state which is described by a small deflection angle $\delta\theta$. Consequently the torque $-\partial F_A/\partial\theta$ is proportional to $\delta\theta$ and can be described:

$$-\partial F_A/\partial\theta=C\delta\theta \qquad (18)$$

where C has the meaning of an effective stiffness, which couples the magnetization vector with a certain crystallographic direction. From equation (18) C can be concluded to be:

$$C=(-\partial^2 F_A/\partial\theta^2)\big|_{\delta\theta\to 0} \qquad (19)$$

With this relation equation 17 can be written:

$$C\delta\theta+HM_S\sin\delta\theta=C\delta\theta+HM_S\delta\theta=0 \qquad (20)$$

This leads to the assumption of an external field which is caused by the magnetic anisotropy.

$$H=((1/M)(\partial^2 F_A/\partial\theta^2))\big|_{\delta\theta=0} \qquad (21)$$

This field is generally called the anisotropy field. It should be noted that θ is calculated with respect to a certain crystallographic direction. Assuming the usual series expansion of F_A (see equation 1;$K_3=0$) H_A can be written as shown in table3.

Table3: Definition of H_A.

H_A	condition	easy axis
$2K_1/M_S$	$K_1>0$	c-axis
$-2(K_1+2K_2)/M_S$	$K_1<-2K_2$	basal plane
$-2K_1(K_1+2K_2)/K_2M_S$	$K_1<0$ $K_1>K_2/2$	cone

3.2.2)Experimental determination of the anisotropy field

3.2.2.1)Extrapolation method

If the relevant samples are not available as single crystals the most common technique determining H_A is the magnetization measurement of powderised aligned material parallel ($M_{\parallel}(H)$) and perpendicular ($M_{\perp}(H)$) to the preferential axis. From a theoretical point of view the powder should be monodomainic grains which are perfectly aligned. Each misorientation or multidomainic grains lead to a curved $M_{\perp}(H)$, which makes the extrapolation very difficult. It is also desirable that the maximum external field is larger then the anisotropy field. One point, which might be additionally of some importance, is the influence of higher order anisotropy constants, as will be shown in the following calculation. Starting with the equation for the total energy:

$$F_t=K_1\sin^2\theta+K_2\sin^4\theta-M_S H\cos(\Psi-\theta) \qquad (22)$$

the equilibrium condition can be written:

$$\partial F_t/\partial\theta=0=2K_1\sin\theta\cos\theta+4K_2\sin^3\theta\cos\theta-M_S H\sin(\Psi-\theta) \qquad (23)$$

Applying the external field H perpendicular to the c-axis and introducing $\sin\theta=M_{\perp}/M_S$ ($M_{\perp}$...projection of $\vec{M}$ on the field direction) equation 23 gets the shape:

$$4K_2(M_{\perp}/M_S)^3+2K_1(M_{\perp}/M_S)-M_S H=0 \qquad (24)$$

which is a cubic equation in $M_{\perp}/M_S$.

It is easy to see that for small fields, small values of $M_{\perp}/M_S$ can be assumed. Consequently in a first approximation the cubic term can be neglected. This leads for not too high fields to the simple solution:

$$(M_{\perp}/M_S)=(M_s/2K_1)H \qquad (25)$$

respectively

$$M_{\perp}(H)\approx(M_S^2/2K_1)H \qquad (26)$$

In order to demonstrate the relative magnitude of the terms of equation 24, the following example, based on typical parameters of $Nd_2Fe_{14}B$ at room temperature ($\mu_0 M=1.6T$, $\mu_0 H=7T$, $K_1=1MJ/m^3$, $K_2=0.1MJ/m^3$), is given. Assuming an external field of 2T,which is typical if an electro-magnet is used, one gets:

$$\mu_0 M_{\perp}(H)=\mu_0 M_S(H/H_A)=0.48T$$

With $M_{\perp}/M_S=0.3$ and $(M_{\perp}/M_S)^3=0.027$ the terms of equation 24 are:

$$4K_2(M_{\perp}/M_S)^3=0.011MJ/m^3 \qquad (27)$$

$$2K_1(M_{\perp}/M_S)=0.6MJ/m^3 \qquad (28)$$

This means that in an external field of 2T the cubic term makes a 2% contribution only. The usual extrapolation leads therefore to H_A values neglecting K_2. An additional error results, as mentioned before, from a misorientation of the sample, which is difficult to correct. From this discussion it can be concluded, that the extrapolation procedure should only be applied, if high enough external fields were applied ($H>0.7H_A$).

3.2.2.2)The SPD-technique

A better method for determining the anisotropy field H_A is the SPD-(Singular Point Detection) technique as developed by (9). It was shown, that in a certain derivative of the magnetization with respect to the field (d^nM/dH^n ;n depends on the symmetry of the hard axis) a singularity appears exactly where $H=H_A$. For uniaxial crystals the second derivative is sufficient. The main advantage of this method is, that it works for polycrystalline materials, but external fields higher then H_A are necessary. Therefore such measurements are generally performed in pulsed field systems, where such high fields are easier to obtain and where the formation of derivatives is no problem. In this chapter a brief review of the theoretical background of this technique is given. First the principles of this method should be explained in a simple manner. If the external field is perpendicular to the easy axis, the magnetization is in a first order approximation a linear function of H as was shown in chapt.3.2.2.1 (see formula 26). If now H is equal to H_A then $M_\perp(H)=M_S$; saturation is achieved. Consequently $M_\perp(H)$ has for $H<H_A$ a slope $M_S^2/2K_1$ and for $H>H_A$ the slope is zero. The magnetization curve of a polycrystalline material is the superposition of the M(H) curves of all grains, which means that all directions between the easy axis and the external field are possible. The M(H) of the grains with an easy axis perpendicular to the external field behaves as discussed above. Differentiating this M(H) curve two times gives a singularity exactly at $H=H_A$, as demonstrated in Fig.2. In a polycrystalline material this singularity is superimposed on the d^2M/dH^2 of all other crystallites and broadened. Consequently measuring d^2M/dH^2 vs H (or $d^2M/dt^2 = {}$ $=d^2M/dt^2 . dt^2/dH^2$; H(t) should be a regular function) a "peak" at $H=H_A$ should appear. This is for uniaxial materials indeed the case. For compounds where the easy axis of magnetization is in the basal plane or in a cone, higher derivatives have to be considered (9).

In the following a more exact description of this technique is given. A polycrystalline, uniaxial material which consists of a large number of noninteracting, randomly orientated crystallites is assumed. Due to the fact, that only the magnetization at $H \rightarrow H_A$ is of interest, the analysis can be restricted on a small intervall located around the hard axis and at fields close to H_A. First a reduced field γ

$$\gamma=(H-|H_A|)/|H_A| \qquad (29)$$

and a reduced magnetization t is introduced.

$$t=M_S(1-\cos(\vec{M}\vec{H}))/M_S=1-\cos(\vec{M}\vec{H}) \qquad (30)$$

Assuming that the external field is orientated close to a hard direction, the reduced magnetization can be calculated:

$$\langle t(\gamma)\rangle=\int t(a,\gamma)W_{\gamma}(a)da \qquad (31)$$

a...angle between the external field and the hard axis.

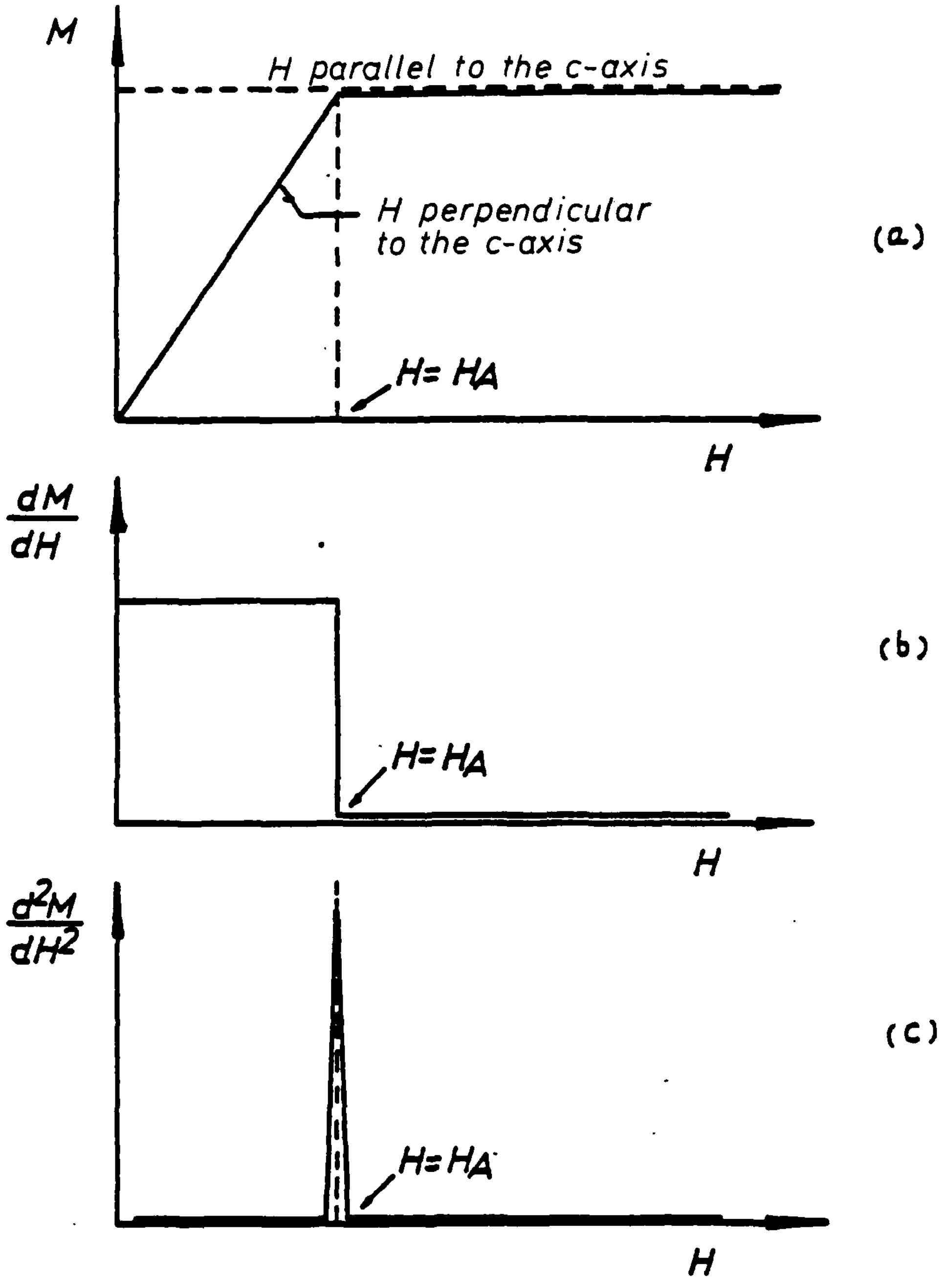

2. Magnetization curve M (H) of an ideal uniaxial crystal as well as their first and second derivative.

W_σ...distribution function of the crystallites.
respectively

$$\langle t(\gamma)\rangle=\int t(x,\gamma)W_\sigma(0)(da/dx)dx \qquad (32)$$

x...angle between the magnetization vector and the external field.

Assuming an easy c-axis and an external field which is orientated in the basal plane, the calculation is continued in the following manner. The total energy is:

$$F_t=K_1\sin^2\theta+K_2\sin^4\theta-HM_s\cos(\varphi-\theta) \qquad (33)$$

from Fig.3 it can be concluded:

$$x=\varphi-\theta\ ;\ \theta=\varphi-x=\pi/2-(a-x)\ ;\ \varphi=\pi/2-a \qquad (34)$$

Introducing the relations 34 into equation 33 leads to:

$$F_t=K_1\cos^2(a+x)+K_2\cos^4(a+x)-M_sH\cos x \qquad (35)$$

Using the normal series expansion for cosx, $\cos^2x$ and $\cos^4x$ gives:

$$F_t=K_1(1-(a+x)^2+(a+x)^4.1/3)+K_2(1-2(a+x)^2+(a+x)^4.(5/3)- \\ -HM_s(1-x\ (1/2)x^2+(1/24)x^4) \qquad (36)$$

From the equilibrium condition $\partial F_t/\partial\theta=0$ and from equation 36 follows:

$$2K_1(a+x)-(4/3)K_1(a+x)^3+4K_2(a+x)-(20/3)K_2(a+x)^3- \\ -HM_sx+(1/6)HM_sx^3=0 \qquad (37)$$

Equation 29 can be written:

$$H=|H_A|(1+\gamma)=(1+\gamma)2(K_1+2K_2)/M_s \qquad (38)$$

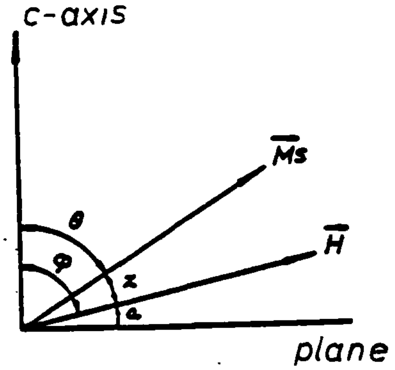

3. Orientation between H and M for the case that H lies approximately in the basal plane.

Due to the fact that H is nearly parallel to the basal plane a=0 is valid; consequently $(x+a)^3\sim x^3+3x^2a$ can be written. Introducing these into $\partial F_t/\partial\theta=0$ gives:

$$a-\gamma x-L_1x^2a-L_2x^3=0 \qquad (39)$$

with

$$L_1=2(K_1+5K_2)/(K_1+2K_2)$$
$$L_2=(K_1+6K_2)/2(K_1+2K_2)$$

The term da/dx is

$$da/dx\approx(\gamma+3L_2x^2)/(1-L_1x^2) \qquad (40)$$

where the approach $xa\ll x^2$ was used. Close to the saturated state the reduced magnetization is:

$$t=1-\cos x\approx x^2/2 \qquad (41)$$

The equations 40,41 and 31,32 gives for the reduced magnetization:

$$\langle t(\gamma)\rangle = W(\pi/2)\int_{x_0}^{x_1} x(da/dx)dx = 2\pi W_\sigma(\pi/2)\{-(\gamma/L_1+3L_2/L_1)(x_1-x_0)- -(L_2/L_1)(x_1^3-x_0^3)+(\gamma/L_1+3L_2/L_1^2)[(1/2\sqrt{L_1})(\ln((1+x_1\sqrt{L_1})/(1-x_1\sqrt{L_1}))- -\ln((1+x_0\sqrt{L_1})/(1-x_0\sqrt{L_1}))]\} \quad (42)$$

The lower integration limit x_0 (which means $a=0$) can be obtained from equation 39 :

$$-\gamma x - L_2x^2 = 0 \quad (43)$$

which gives

$$x_0 = \sqrt{(-\gamma/L_2)} = ((|\gamma|-\gamma)/2L_2)^{1/2} \quad (44)$$

The upper integration limit is free. The reduced magnetization can now be written:

$$\langle t(\gamma)\rangle = 2\pi W_\sigma(\pi/2)\{A_1((|\gamma|-\gamma)/2)^{1/2}+A_2((|\gamma|-\gamma)/2)^{3/2}- -A_3\ln(1+((|\gamma|-\gamma)L_1/2L_2)^{1/2})/(1-((|\gamma|-\gamma)L_1/2L_2)^{1/2}) + f(\eta) \quad (45)$$

The new variables A_1, A_2 and A_3 have the meaning:

$$A_1 = ((\gamma/L_1)+(3L_2/L_1^2)).(1/\sqrt{L_1}) \quad (46)$$

$$A = 1/L_1\sqrt{L_2} \quad (47)$$

$$A_3 = (1/2\sqrt{L_1})((\gamma/L_1)+(3L_2/L_1^2)) \quad (48)$$

From equation 45 it can be concluded that at $\gamma=0$ $(H=H_A)$ in the first derivative of the first term and the second derivative of the second and of the third term a singularity appears. The relative magnitude of these singularities depend on the ratio of the corresponding coefficients A_1 , A_2 and A_3 which are:

$$A_1/A_2 = (3/4)((1+6\eta)/(1+5\eta)) \quad (49)$$

$$A\ /A\ = (3/2)((1+6\eta)/(4+20\eta)) \quad (50)$$

with $\eta = K_2/K_1$. The dependences of (A_1/A_2) and (A_3/A_2) of η are shown in Fig.4. From this picture it can be seen that usual the singularity of the first derivative is small compared with that of the second derivative, except the point $\eta = -0.2$ and for $\eta \to \pm\infty$.

If the symmetry of the hard axis is different it can be shown that the order of the derivative where a singularity appears is larger than two. Consequently if the easy axis lies in a cone or in the basal plane the third derivative have to be considered. This is due to the with the order of the derivative increasing signal to noise ratio extremely difficult to measure. Therefore the SPD-technique is a very usefull technique for determinig the anisotropy field of uniaxial materials, but it cannot so easely applied for other symmetries.

3.3)FOMP transition.

A FOMP transition (First Order Magnetization Process) transition occurs if in the shape of the anisotropy energy function additional relative minima appears, leading to a jump in the M(H) curve. This can happen at a certain temperature where higher order anisotropy constants becomes large compared to K_1. Consequently this effect is expected approaching a spinreorientation where K_1 changes its sign. A

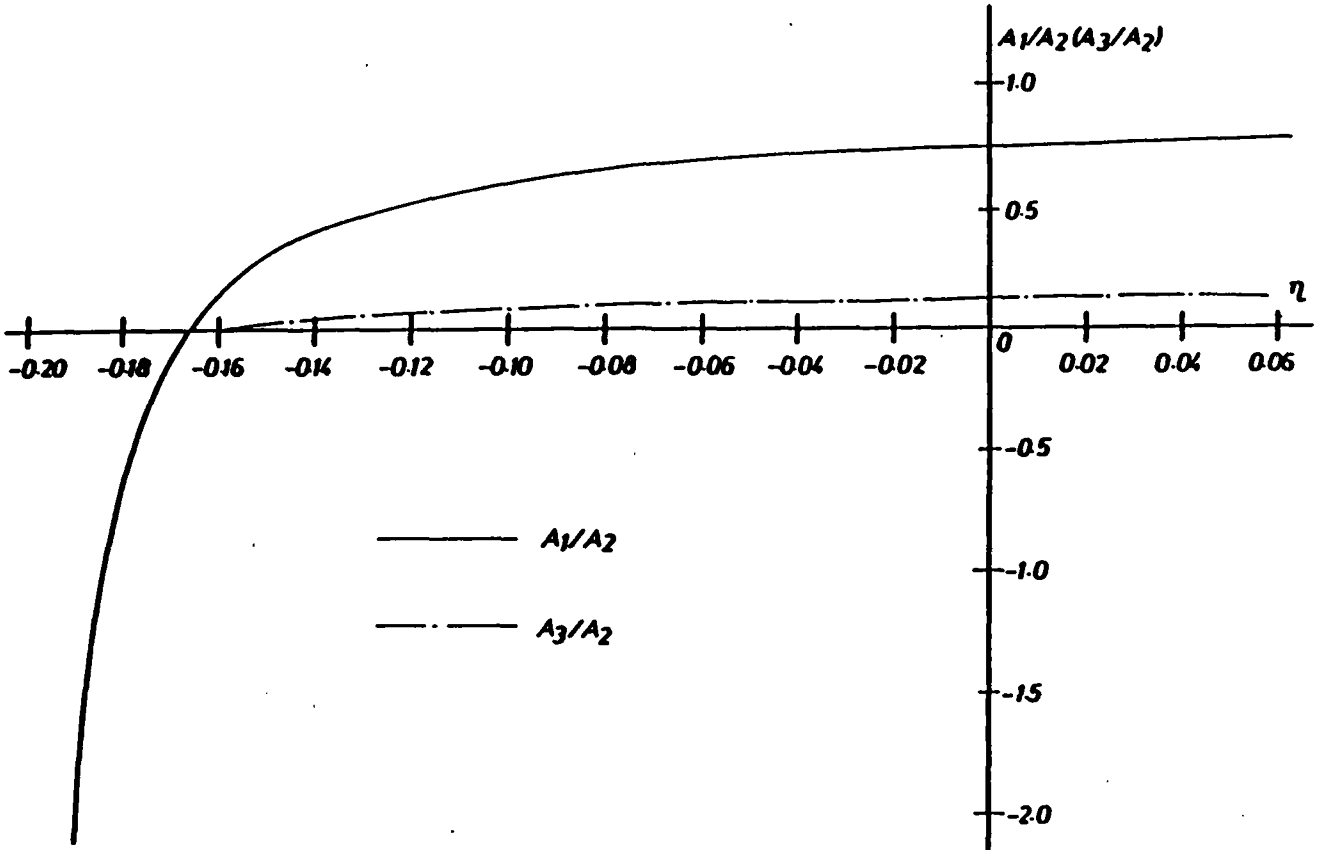

4. Dependence of the amplitude ratios (A_1/A_2) and (A_3/A_2) on η.

good example for this purpose is $PrCo_5$, where at 107K a change of the easy axis to an easy cone occurs. Between 107K and 155K a FOMP was detected. In order to demonstrate this the temperature dependence of K_1, K_2 and K_3 of $PrCo_5$ is shown in Fig.5 (7). It is obvious that below 150K the contribution of K_2 and K_3 to F_A is no longer negligible. The general theory of a FOMP transition was developed by (6). In Fig.6 the the different shapes of the anisotopy functions causing such a FOMP and consequently jumps in M(H) according to (6) are shown. In $Nd_2Fe_{14}B$ between 135K and 180K a similar behaviour was found (10);at 135K a spinreorientation from the c-axis to an easy cone occurs (4). Fig.7 shows $K_1(T)$ and $K_2(T)$ of a $Nd_{16.7}Fe_{75.5}B_{7.8}$ sample according to (11). The large influence of K_2 on F_A below 200K is evident. It should be mentioned there that a spinreorientation is not a necessary condition for the occurence of a FOMP. It is due to the change of the sign of K_1 only favourable for this effect.

In order to clearify the situation in $Nd_2Fe_{14}B$ the theory of a FOMP transition is here for the first time given for a tetragonal symmetry, following (12). Starting again with the free energy of a tetragonal crystal:

$$F_t = K_1 \sin^2\theta_M + K_2 \sin^4\theta_M + K_3 \sin^4\theta_M \sin^2\phi_M \cos^2\phi_M - \vec{H}\vec{M}_s \qquad (51)$$

The meaning of the angles can be obtained from Fig.8, which can be used to calculate $\vec{H}\vec{M}_s$.

$$\vec{H}\vec{M}_s = HM_s \sin\theta_H \cos\phi_H \sin\theta_M \cos\phi_M + \\ + HM_s \sin\theta_H \sin\phi_H \sin\theta_M \sin\phi_M + HM_s \cos\theta_H \cos\theta_M \qquad (52)$$

With the above given equations and the equilibrium condition $\partial F_t / \partial\theta_M = 0$ and $\partial F_t / \partial\phi_M = 0$ the basic equation for the discussion of a FOMP can be written:

$$2K_1 \sin\theta_M \cos\theta_M + 4K_2 \sin^3\theta_M \cos\theta_M + 4K_3 \sin^3\theta_M \cos\theta_M \sin^2\phi_M \cos^2\phi_M - \\ - HM_s(\sin\theta_H \cos\phi_M \cos\theta_H \cos\phi_M + \sin\theta_H \sin\phi_H \cos\theta_M \sin\phi_M - \\ - \cos\theta_H \sin\theta_M) = 0$$

$$2K_3 \sin^4\theta_M \sin\phi_M \cos\phi_M (\cos^2\phi_M - \sin^2\phi_M) - HM_s(\sin\theta_H \sin\phi_H \sin\theta_M \cos\phi_M - \\ - \sin\theta_H \cos\phi_H \sin\theta_M \sin\phi_M) = 0 \qquad (53)$$

The solution of these equations is naturally not simple. In principle two cases may be of interest:

i) H perpendicular to the c-axis (P-case)

ii) H parallel to the c-axis (A-case)

i)P-case: This means $\theta_H = \pi/2$. Taking into account that the final state of the magnetization is equal to M_s (FOMP typel) leads to a free energy of the final state:

$$F_t^f = K_1 + K_2 + K_3 \sin^2\phi_H \cos^2\phi_H - HM_s(\cos^2\phi_H - \sin^2\phi_H) \qquad (54)$$

The free energy of the initial state is:

$$F_t^i = K_1 \sin^2\theta_M + K_2 \sin^4\theta_M + K_3 \sin^4\theta_M \sin^2\phi_M \cos^2\phi_M - \\ - HM_s(\cos\phi_H \sin\theta_M \cos\phi_M + \sin\phi_H \sin\theta_M \sin\phi_M) \qquad (55)$$

The transition occurs where $F_t^i = F_t^f$. This leads to an equation which is fundamental for the existence of a FOMP of the typel in the tetragonal structure. Unfortunately it is to complicated for an analytical solution.Therefore $K_3 = 0$ is assumed. It is now a 2-dimensional problem with the

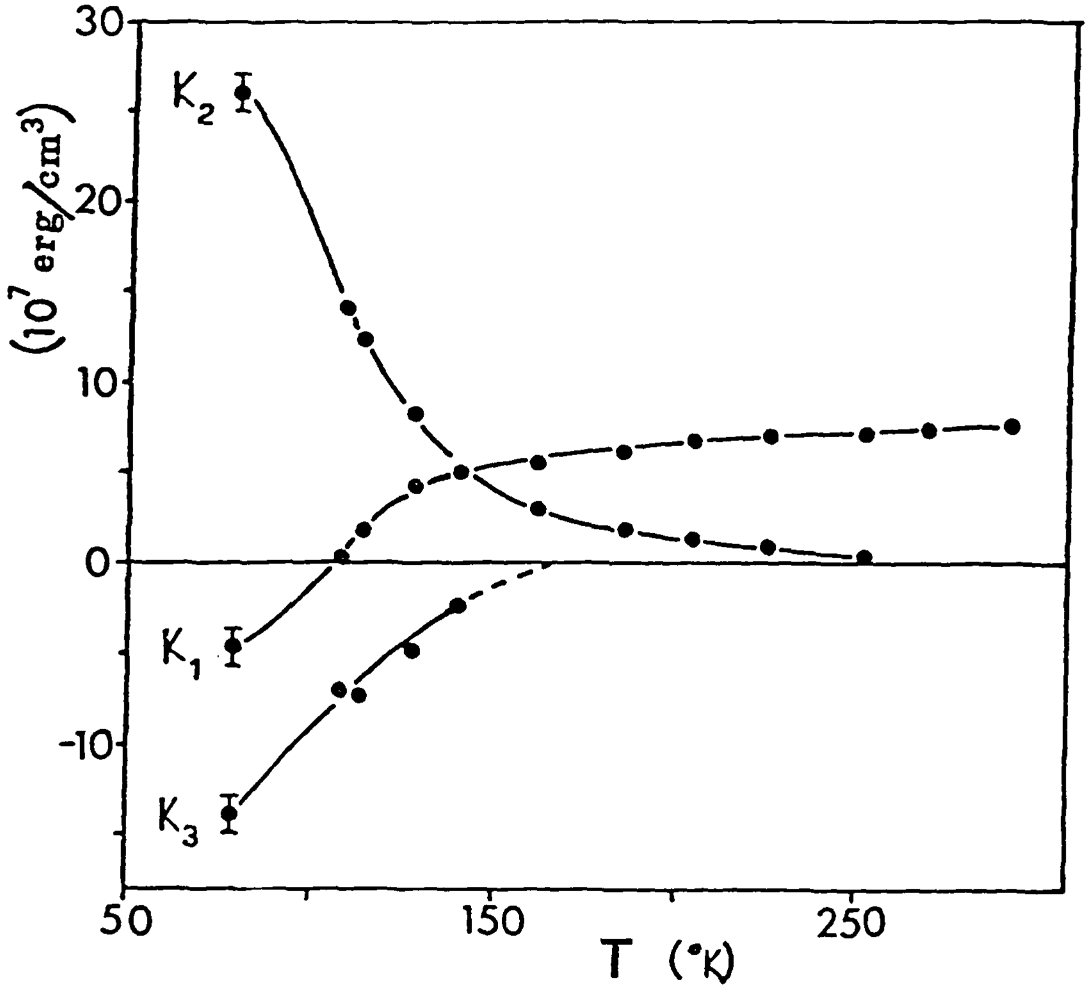

5. $K_1(T)$, $K_2(T)$ and $K_3(T)$ of $PrCo_5$ according to (7).

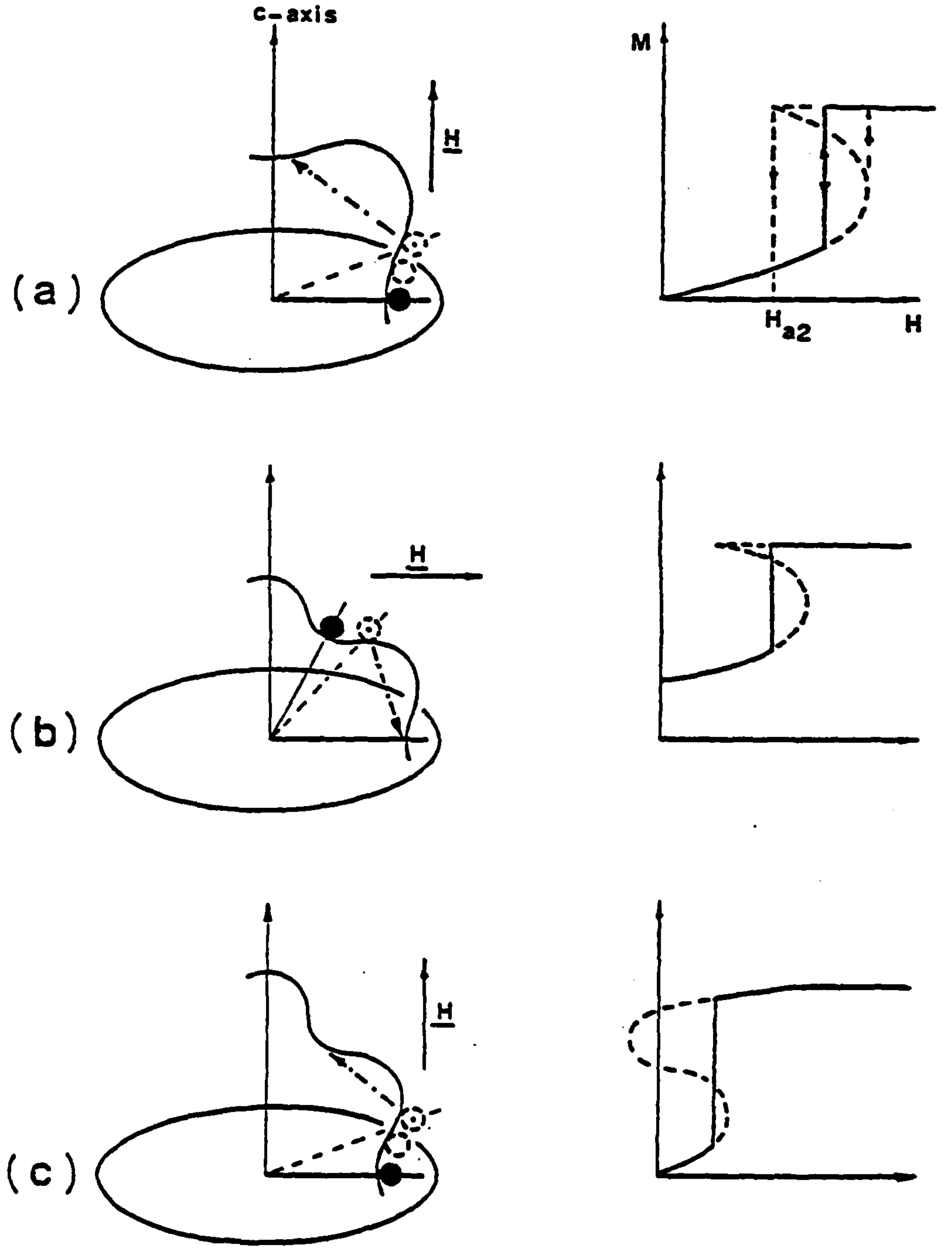

6. Examples of FOMPs of different types (on the right side)
a)type 1,
b)type 2 with an easy cone,
c)type 2.
The diagrams on the left are cross sections of the anisotropy energy surface (according to (6)).

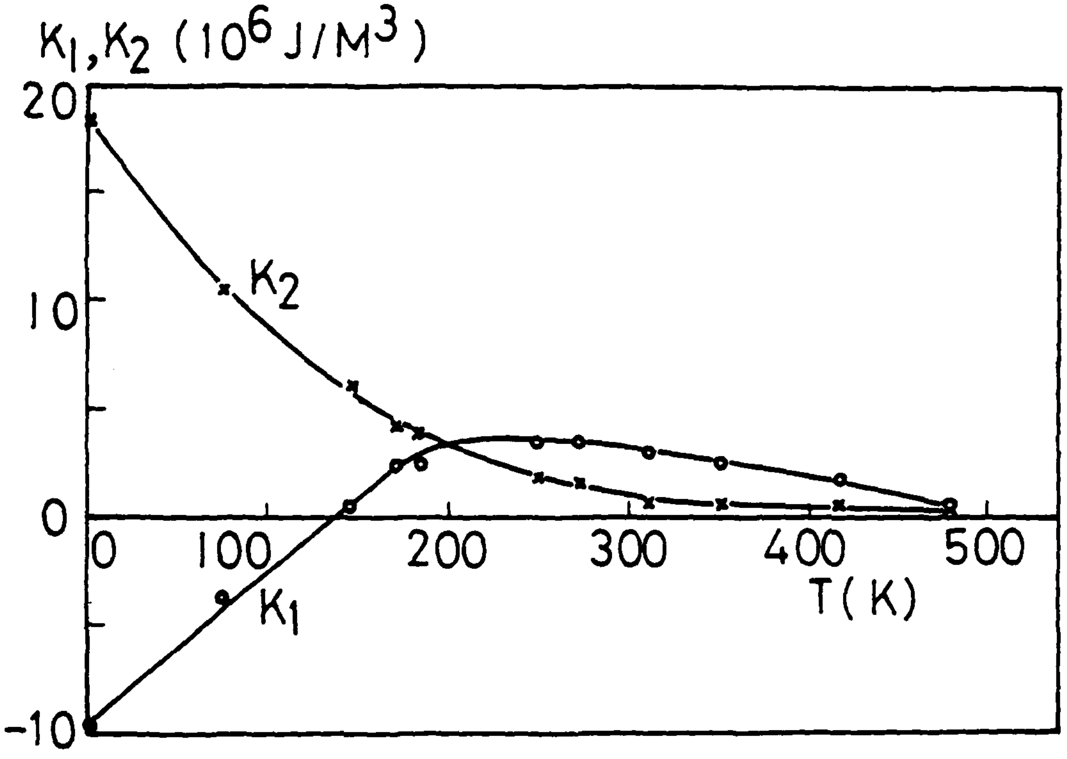

7. $K_1(T)$ and $K_2(T)$ of $Nd_{16.7}Fe_{75.5}B_{7.8}$ due to (11).

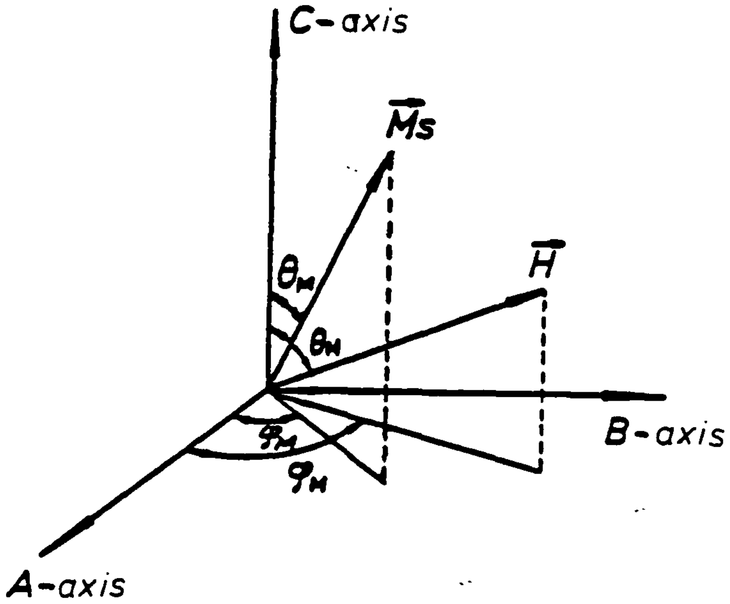

8. Scetch of M and H in a tetragonal system.

equations:

$$\begin{aligned}&(\sin\theta-1)(K_1(\sin\theta+1)+K_2(\sin^2\theta+1)(\sin\theta+1)-HM_s)=0\\&2\sin\theta(K_1+2K_2\sin^2\theta)=HM_s\end{aligned}\tag{56}$$

Introducing

$$\begin{aligned}&h=2H/|H_A|\\&H_A=2K_1/M_s\\&\eta=K_2/K_1\end{aligned}\tag{57}$$

and reducing the two equations 56 to one gives:

$$(1+\eta)+2\eta\sin\theta+3\eta\sin^2\theta=0\tag{58}$$

with $$\sin\theta=(-1/3)\pm(-3\eta-2\eta^2)^{1/2}/3\eta\tag{59}$$

This expression gives a critical value for $\sin\theta$ with $\sin\theta=M_{cr}/M_s$ from which the critical magnetization can be deduced. The critical field where the transition occurs can be deduced from the equations 56 and 59. From equation 59 follows also the condition for the anisotropy constants where a FOMP transition from the typel is expected:

$$-1.5\leqslant\eta\leqslant 0\tag{60}$$

A similar calculation can be performed applying the external field parallel to the c-axis (A-case), which leads to the critical angle:

$$\cos\theta=((-1/3)\pm(3\eta+4\eta^2))^{1/2}/3\eta\tag{61}$$

The condition for the occurence of this FOMP is:

$$0\leqslant\eta\leqslant 0.75\tag{62}$$

In the case of a type2 FOMP (see Fig.6) it can be shown that the basis anisotropy is no longer neglectable. The principle of the calculation is similar as shown before. Unfortunately it gives a system of equations which can be solved numerically only, which was not yet done.

From an experimental point of view a FOMP transition is not so easy to detect. Measuring M(H) of a polycrystalline sample generally no step can be observed due to the averaging effect of such a sample. But if one uses the differentiating technique, as neccesary applying the SPD-technique (see Chapt.3.2.2.2) even in polycrystalline materials a significant change of the shape of the singularity in d^2M/dt^2 vs H is detectable if a FOMP exists. In order to demonstrate this Fig.9 shows the singularity as measured on $Nd_2Fe_{14}B$ at 300K (usual peak at $H=H_A$) in comparison to the singularity as obtained at 135K. The first derivative at this temperature is there also drawn. The remarkable difference of the shape of the singularity is obvious. A carefull analysis which type of FOMP exist in this compound is not yet possible. High field measurements at 4.2K performed on an aligned sintered $Nd_{15}Fe_{77}B_8$ magnet showed a not well pronounced change of the slope in the M(H) curve applying the external field perpendicular to the c-axis, exactly at the field where due to pulsed field measurements the FOMP anomaly is expected ($\mu_0 H_{cr}$=16.3T) (13).

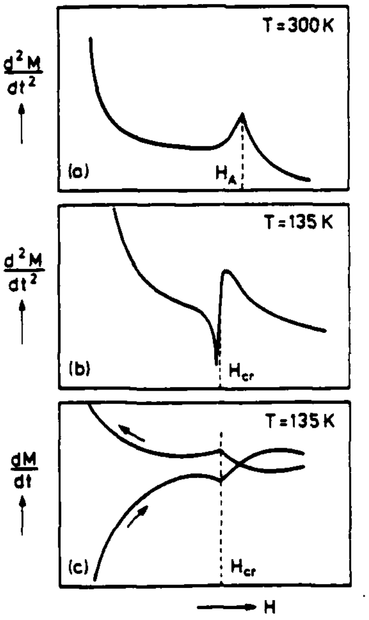

9. Field dependence of d^2M/dt^2 in $Nd_2Fe_{14}B$ at T=300K (a) and T=135K (b), and field dependence of dM/dt at T=135K (c).

3.4) Theoretical aspects of the coercivity

It is well known that a high uniaxial anisotropy is a necessary condition for the formation of a high coercivity in a permanent magnet. In the case of a monodomainic single particle magnet the hysteresis loop looks as shown in Fig.10. At $H={}_{I}H_c$ the magnetization jumps from $-M_r$ to $+M_r$, consequently the free energy of the system goes from a minimum to a maximum. Therefore the coercivity is in this case determined by the condition $\partial F_t/\partial\theta=0$ and $\partial^2 F_t/\partial\theta^2=0$. Using the formula for the free energy (see equation 33) the previous given condition leads to the equation (H parallel to the easy c-axis, $\psi=0$):

$$2K_1\sin\theta+4K_2\sin^3\theta\cos\theta+HM_s\cos\theta=0, \quad (63)$$

$$2K_1\cos^2\theta-2K_1\sin^2\theta+12K_2\sin^2\theta\cos^2\theta-$$
$$-4K_2\sin^4\theta+HM_s\cos\theta=0 \quad (64)$$

The solution gives the coercivity ${}_{I}H_c$:

$${}_{I}H_c=2K_1/M_s \quad (65)$$

Assuming an easy basal plane a similar calculation leads to a coercivity value of:

$${}_{I}H_c=2(K_1+2K_2)/M_s \quad (66)$$

From these simple calculations it is clear that for ideal monodomainic particles the coercivity field is equal to the anisotropy field (see table 3). Consequently the temperature dependence of the coercivity field must correspond to that of the anisotropy field. This is for

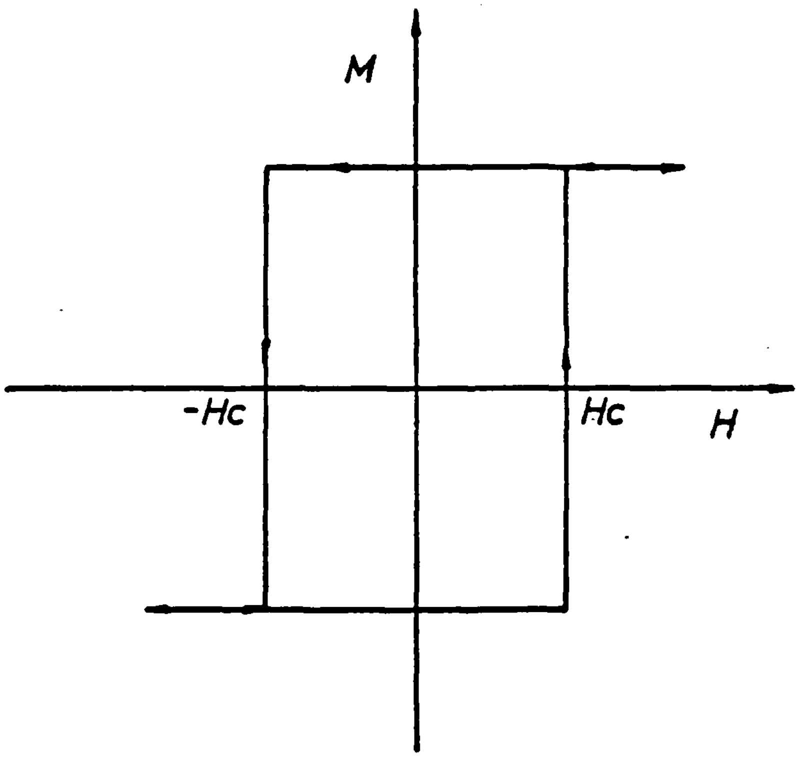

10. Hysteresis loop of an ideal monodomainic grain.

technical permanent magnets not the case. The reason is that the grains in sintered magnets does not correspond ideal single particles. The critical diameter of single domain particles is:

$$D_c = 1.4\gamma / M_s^2 \qquad (67)$$

using the relation for γ (14):

$$\gamma = 2\sqrt{AK_1}\{1 + [(1+\eta)/\eta^{1/2}]\sin^{-1}(\eta/\eta+1)^{1/2} \qquad (68)$$

A...average exchange constant; $\eta = K_2/K_1$.

The critical diameter of superparamagnetic particles is:

$$d_c = (kT/2K_1)^{1/3} \qquad (69)$$

In the case of the there interesting $Nd_2Fe_{14}B$,according to (15), the room temperature values are: $A = 7.7 \times 10^{-7}$ erg/cm, $D_c = 0.2 \mu m$, $d_c = 7.9 Å = 0.00079 \mu m$. The average grain size of a sintered magnet is between 5 and 10μm (15), that of a rapidly quenched material is approximately 0.02 up to 0.08μm (16). This means that the grains of a sintered magnet are much larger then D_c and that of a rapidly quenched compound smaller then D_c. In both cases $_IH_c$ values far below the anisotropy field where measured (10). For sintered Nd-Fe-B magnets according to the above made comparisons no simple correlation between $_IH_c$ and H_A is expected. However there exist theories describing the temperature dependence of the coercivity, which were applied to $SmCo_5$ successfully (17). In the foolowing the main ideas of these considerations are presented.

Kronmüller and Hilzinger (18) have shown that in the case of incoherent nucleation the coercivity field is determined either by the nucleation of reversed domains in the magnetically soft phase or by the expansion of these reversed domains into the magnetically hard matrix. In both cases $_IH_c$ is approximately given by

$$_IH_c \sim K_1/M_s \qquad (70)$$

In the first case, however, we have to insert into equation (70) the anisotropy of the perturbed region, whereas in the second case K_1 means the anisotropy constant of the hard magnetic matrix. Another possibility is that the coercive force is caused by a pinning of domain walls at grain boundaries. It is expedient to distinguish two cases corresponding to the thickness D of the grain boundaries with respect to the wall with $d = \pi\delta_0$. In the case of thin grain boundaries compared with the wall width $_IH_c$ is given by

$$_IH_c \sim (1/3\sqrt{3})(2K_1/M_s)(D/\delta_0)((A/A') - (K'/K)) \qquad (71)$$

Provided the relative variations A'/A and K'/K of exchange and anisotropy energy at the grain boundary are independent of T, the temperature dependence of $_IH_c$ follows from equation (71) as

$$_IH_c(T) \sim (K/M_s)^{3/2} \qquad (D \ll \delta_0) \qquad (72)$$

For extended deffects we find a dependence according to (17)

$$_IH_c(T) \sim K/M_s \qquad (D \gg \delta_0) \qquad (73)$$

The domain walls in hard magnetic materials are extemaly narrow due to the large magnetic anisotropy. In such materials atomic defects act as effective pinning centres. Nearly all permanent magnets deviate from the exact stochiometry, therefore the existence of such defects can be assumed. The temperature dependence of ${}_IH_c$ following from a pinning of domain walls by atomic disorder is due to (19)

$$ {}_IH_c(T) \sim M_s^2 (K/M_s)^{5/4} \qquad (74) $$

In materials with not so high coercivity fields it was assumed that ${}_IH_c$ is determined by volume pinning. The pinning forces are supposed to originate from statistically distributed defects. Due to the larger wall area the statistical fluctuations of the defect density are less important. An extended wall may respond to the interaction force of the defects, i.e. vaulting of the domain wall occur. If this vaulting happens in only two dimensions the coercivity field is determined as

$$ {}_IH_c = 1.10^{-2} (E_0^2 \rho / 4\pi\rho M_s \gamma \delta_0^2) \qquad (75) $$

E_0...interaction energy of the wall with a single defect
ρ...density;γ...specific wall energy.

Since the interaction of the wall with the defect is caused by a local perturbation of anisotropy and exchange energy, it is assumed that E_0 reveals the same temperature dependence as K_1 (19). Equation (75) then leads to a temperature dependence according to

$$ {}_IH_c(T) \sim (K_1/M_s)^{5/2} \qquad (76) $$

At low temperatures, however, the pinning force of the defects may approach a constant value just like the anisotropy, whereas the experimental determined coercivity is still strongly temperature dependent. In this case the coercivity can be described by the movement of narrow domains where the mobility depend on the position of the domain wall centre with respect to the crystal lattice. This movement is determined by an intrinsic Peierls potential (20). In this case no relations exist describing ${}_IH_c(T)$ as given above.

Summarising due to (17) a correlation between ${}_IH_c$ and H_A is expected in many cases. It is therefore usefull to test the above given formulas. From an experimental point of view we are able to measure both: ${}_IH_c(T)$ and $H_A(T)$ (SPD-method) on the same sample! This gives the possibility to examine the validity of the different models by plotting $\ln({}_IH_c(T))$ vs $\ln(H_A(T))$ in order to determine the power "k" (slope of this plot) of the general relation:

$$ {}_IH_c \sim (H_A)^k \qquad (77) $$

4)Experimental methods

The hysteresis as well as the anisotropy measurements were performed in a pulsed field system. A condensator battery of 8mF with a maximum charging voltage of 2500V (stored energy: 25kJ) is discharged through a N_2 -cooled, reinforced copper-magnet. The pulse duration depends on the inductivity of the magnet; generally a pulse of 4ms (sin half wave) was used. The maximum available field is 28T (sin half wave). A sin full wave (hysteresis measurements) was generally restricted to a maximum field of 15T. This was necessary in order to avoid dielectric losses in the condensators, which might be dangerous for them. The second amplitude was at room temperature due to the resistivity of the magnet 50% of the first one. For accurate hysteresis measurements a new magnet was optimized with a maximum field of only 10T but with a pulse duration of 30ms and with a second amplitude of 80% of the first one. All measurements can be performed from 4.2K up to 800K. A more detailed description of the equipment can be found in (21,22). The magnetization as well as the field is measured by a pick-up coil system using the law of induction. The measuring principle was discussed in (23). The main improvement was reached in the data equipment. The analogous signals are buffered in a digital storage oscilloscope (type VUKO modell VKS 22-16). This storage oscilloscope is linked to a micro-computer (type sinclair ZX spectrum). The software is written in BASIC, tests on a IBM-personal computer proved the generality of the programs. Theses procedures alows the subtraction of the "zero-signal", the calculation of M(H), B(H) and B(H)max in selectable physical units.

The accuracy of pulsed field measurements are restricted by two problems:

i) The calibration procedure.
ii) Eddy current problems.

The field calibration was performed using the singularity at H_A of well known samples (e.g. $BaFe_{12}O_{19}$ at room temperature or YCo_5 and $PrCo_5$). The absolute accuracy in H is therefore 5%. This rather poor accuracy is caused by the finite broadness of the "peak" of the singularity as well as by uncertainties of the published H_A data. The relative accuracy is 0.5% (the ADC of the storage oscilloscope has 8 bits). The magnetization calibration was performed using a plastic bonded Fe-powder (mean grain size 10μm) sample, which was measured in a static magnetometer with an accuracy of better then 1%. The pulsed field magnetization measurements are therefore accurate, from this point of view, to about 2%.

The error which can occure due to eddy currents in the sample can be estimated calculating the skin depth according to (24):

$$\delta = \sqrt{2\varrho/\omega\mu_r\mu_o} \tag{78}$$

ϱ...Specific electrical resistivity (Ωm)
$\omega = 2\pi f$...radial frequency;μ_r...relative permeability
$\mu_o = 4\pi 10^{-7}$Vs/Am...vacuum permeability

The skin depth is the depth where the external time dependent magnetic field is weakened with a factor 1/e=0.37.

For sintered as well as for polycrystalline Nd-Fe-B samples the specific elelctrical resistivity is $1.5\times10^{-6}\Omega$m at room temperature respectively $0.3\times10^{-6}\Omega$m at 4.2K. The puls duration is approximately 5ms which corresponds a frequency of 100Hz. For a permanent magnet μ_r is close to 3. These assumptions give for δ a value of 3.5cm at room temperature respectively 1.6cm at 4.2K. The samples measured usually in the pulsed field system have a dimension of 2mm. Consequently the extenal field is at room temperature in the centre 3% at 4.2K 6% smaller. This is however the case only in the field range where the slope of the M(H) curve is largest (near to ${}_IH_c$). Approaching the saturation this error becomes smaller. This shielding effect due to eddy currents causes a smoothening near ${}_IH_c$. However only a small part of the sample is here involved. The mean error due to these eddy currents is of the order of 1%. Up to now the errors caused by the troubles of the calibration procedure are expected to be more important. Therefore improvements of the calibration method are necessary to develope.

All mixed crystal series were prepared by high frequency melting under an argon atmosphere using a water cooled copper boat. All compounds were annealed at 950°C for 1 week. The phase homogeneity was checked by X-ray Debye-Scherrer patterns of pulverised material. All samples were polycrystalline. The technical permanent magnets were sintered aligned materials supplied by Colt Industries (samples: "Colt 1", Crumax 30A, Crumax 35, Crumax 40) and by Sumitomo Special Metals (samples: "Sum 1", 30H and a $Pr_{15}Fe_{77}B_8$ magnet). The latter magnet was produced from 99.9% Pr metal, 99.5% electric Fe and metallic B. The induction melted polycrystalline sample was ballmilled down to 2.3 μm (measured with a Fisher subsieveseizer). After aligning and pressing it was sintered at 1060°C for 1.5 hours and post heat treated at 630°C for one hour. From all other commercial magnets no detailed production procedures were available.

5)Experimental results

5.1) The mixed crystal series $(Nd,R)_{15}Fe_{77}B_8$ (R=Y,La,Ce)

The composition 15/77/8 was choosen because it corresponds to that which is generally the technically one. Fig.11 shows the temperature dependence of $\mu_0 H_A$ of $(Nd_xY_{1-x})_{15}Fe_{77}B_8$, fig.12 of $(Nd_xLa_{1-x})_{15}Fe_{77}B_8$ and fig.13 of $(Nd_xCe_{1-x})_{15}Fe_{77}B_8$ according to (25). In the picture with the La substituted compounds the results of the $La_2Fe_{14}B$ sample was drawn for comparison. In all cases the anisotropy field decreases with increasing Nd substitution. For all Nd-containing samples a change of the shape of the singulariry at low temperatures was observed, indicating a

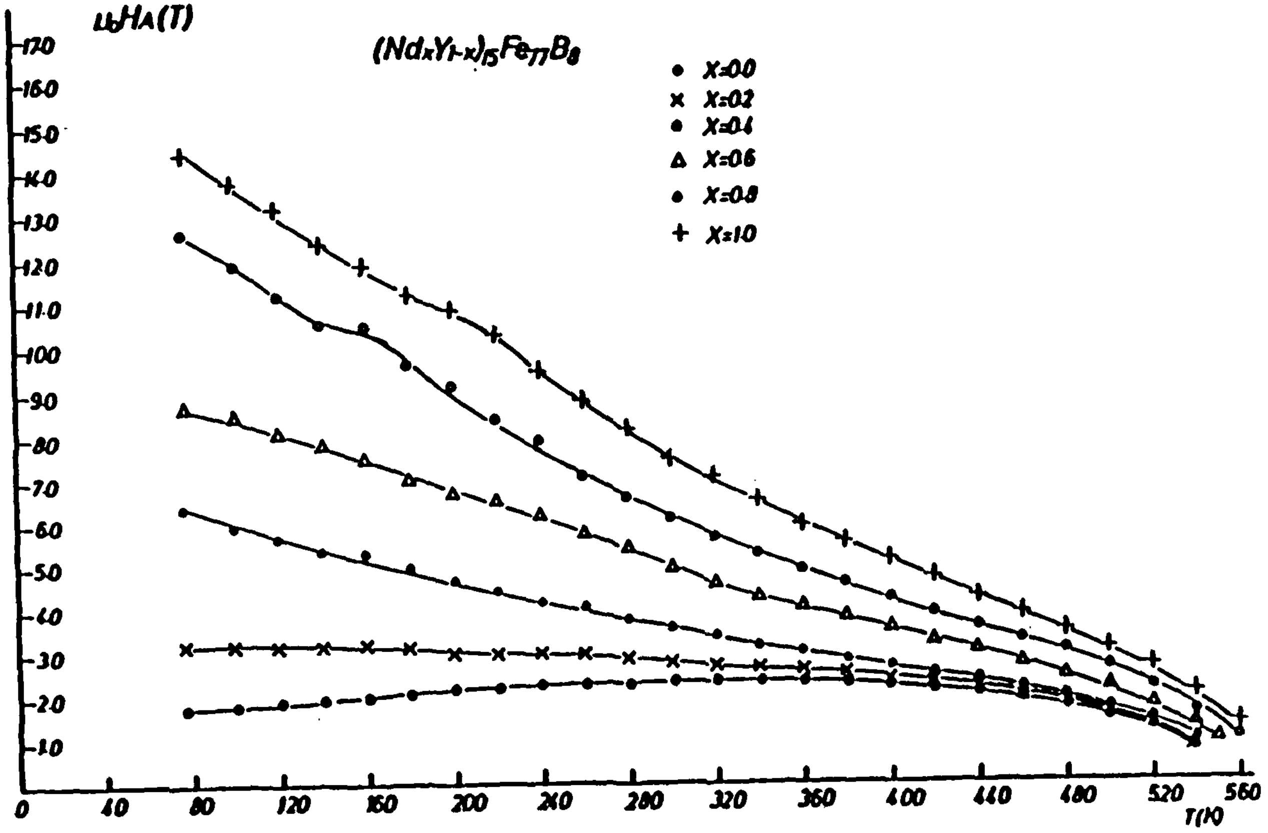

11. Temperature dependence of the anisotropy field of $(Nd_xY_{1-x})_{15}Fe_{77}B_8$.

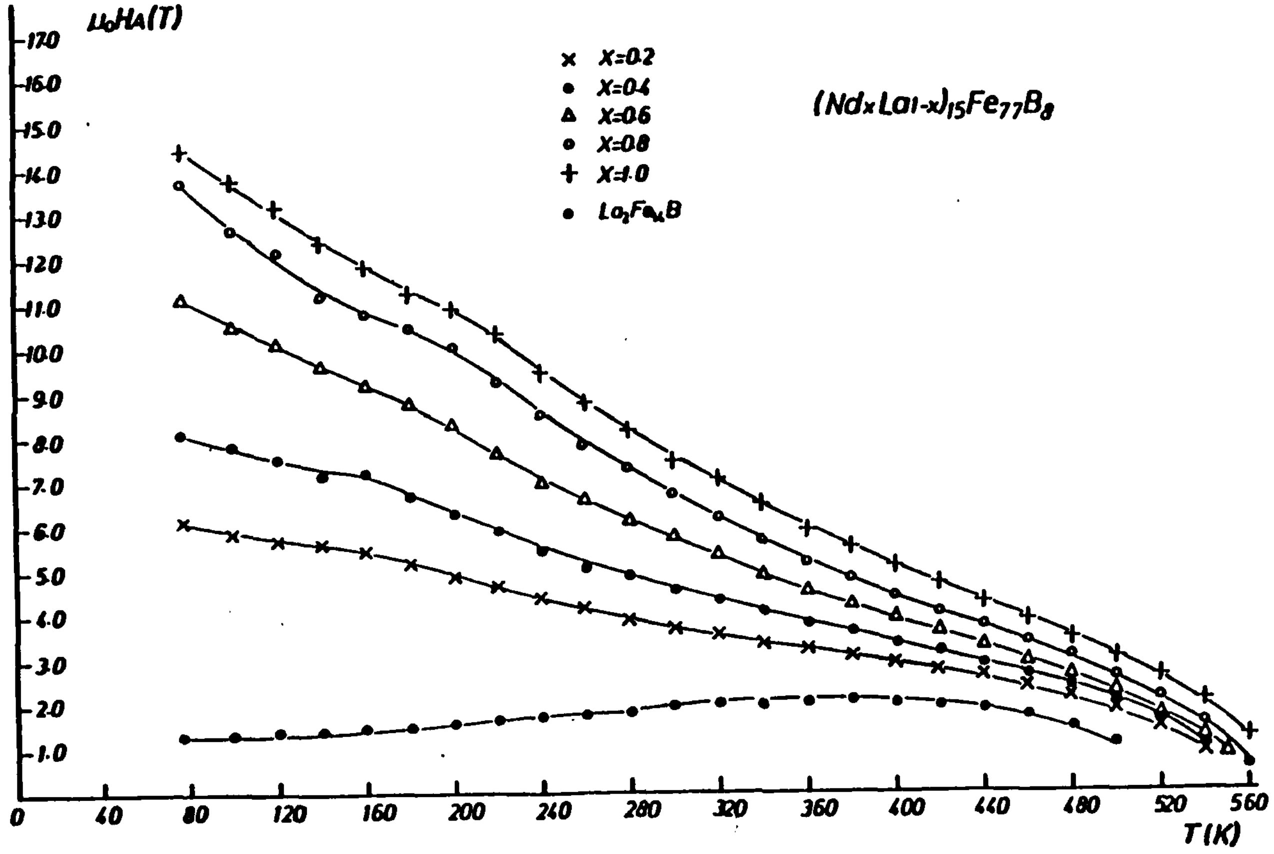

12. Temperature dependence of the anisotropy field of $(Nd_xLa_{1-x})_{15}Fe_{77}B_8$.

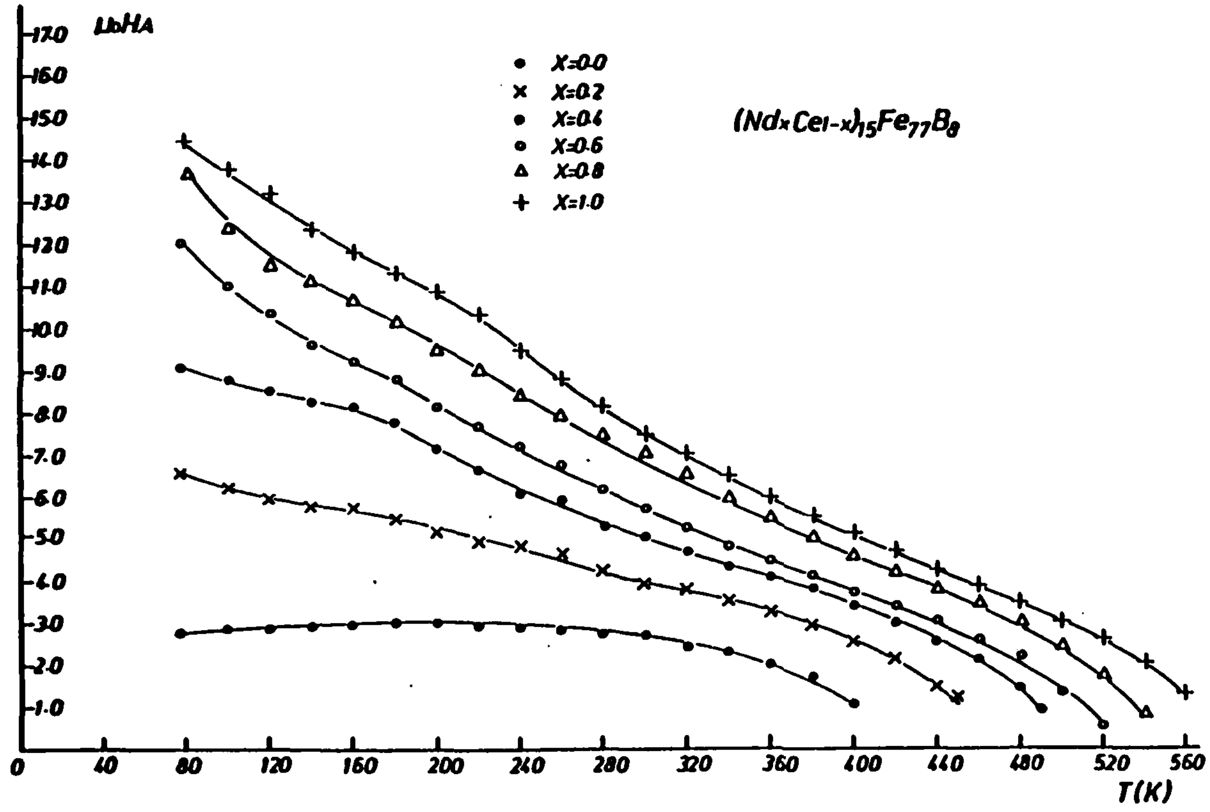

13. Temperature dependence of the anisotropy field of $(Nd_xCe_{1-x})_{15}Fe_{77}B_8$.

FOMP transition which leads possibly to an easy cone at lower temperatures. AC-susceptibility measurements between 4.2K and room temperature performed on all compounds give evidence for the existence of a magnetic transition in all Nd-containing samples at low temperatures too. The transition temperatures are given in table 4.

Table 4: Transition temperatures T_P of $(Nd_xR_{1-x})_{15}Fe_{77}B_8$ as measured with the ac-susceptibility.

Alloy R=Y x	T_P(K)	Alloy R=La x	T_P(K)	Alloy R=Ce x	T_P(K)
0.0	-	0.0	-	0.0	-
0.2	100	0.2	119	0.2	90
0.4	114	0.4	123	0.4	109
				0.5	115
0.6	126	0.6	128	0.6	120
		0.7	130	0.7	124
0.8	131	0.8	131	0.8	127
		0.9	132	0.9	130
1.0	136				

It should be noted that T_P as obtained from ac-susceptibility measurements lies always below the temperature where due to the pulsed field results a FOMP tranisition starts. This can be explained by the fact that the cusp in $\chi_i(T)$ marks the spinreorientation whereas the high field anomaly starts where K_1 becomes small.
Subtracting the $H_A(T)$ of the corresponding boundary compound with a nonmagnetic R-ion (Y,La,Ce) which represents the anisotropy of 3d-sublattice, gives the temperature dependence of the Nd-sublattice. A simple analysis based on the One Ion model showed in a first order approximation its validity for the Nd-anisotropy (25).

5.2)The $R_2Fe_{14}B$ compounds

The temperature dependence of the anisotropy field H_A of various $R_2Fe_{14}B$ compounds are compared in Fig. 14. In general one expects the anisotropy field to decrease with increasing temperature. This behaviour is only observed for these $R_2Fe_{14}B$ samples in which the R component has an orbital moment and where one may assume that the anisotropy originates from crystal field effects. In the $R_2Fe_{14}B$ compounds in which R is nonmagnetic (R=Y,La,Lu,Ce or Th) the anisotropy is due to the 3d sublattice magnetization. It is interesting to note that the temperature dependence of H_A in these materials shows the opposite behaviour to those referred above, i.e. the anisotropy field slightly increases

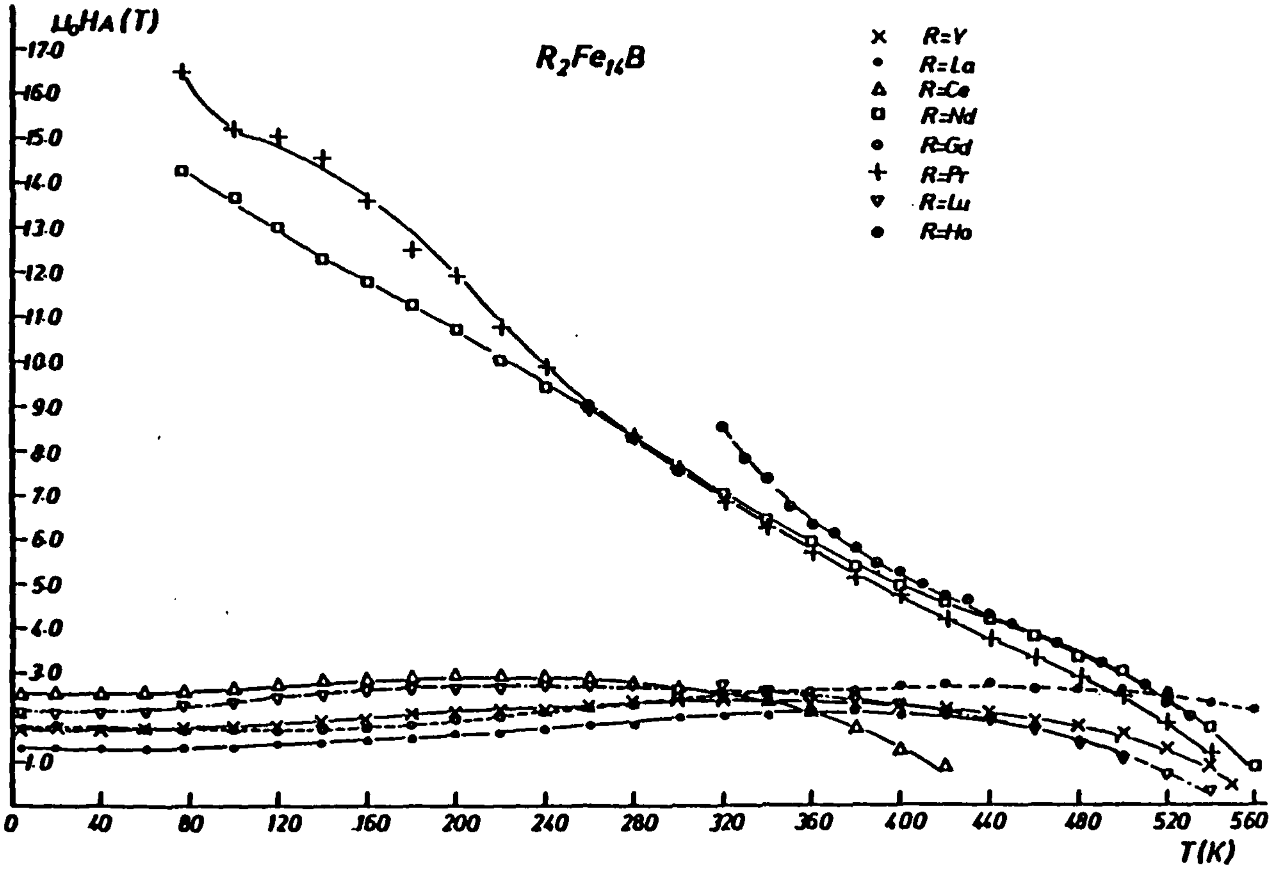

14. Temperature dependence of the anisotropy field of the $R_2Fe_{14}B$ compounds.

with increasing temperature (at least at temperatures well below the Curie temperature). These results suggests that the Fe atoms at the different crystallographic Fe sites contribute differently to H_A and also that the temperature dependence of these contributions is not the same. A similar situation was assumed to exist in Y_2Co_{17} (26). Attempts were made to describe the 3d sublattice anisotropy in uniaxial intermetallic compounds in terms of the second order crystal field parameters B_2^0 (27). In this model a correlation between the anisotropy energy and the factor $(1-(3/8)(c/a)^2)$ would be expected, where a and c are the lattice constants. The values of H_A obtained in the course of the work (28) are compared with values of the factor $(1-(3/8)(c/a)^2)$ in table5 using data for a and c reported elsewhere (29). When interpreting the data shown in the table one has to take account of the fact that the situation in compounds where R is trivalent may be slightly different from that in compounds where R is tetravalent. In general the correlation appears to be quite satisfactory.

Table 5: Comparison between the values of $(1-(3/8)(c/a)^2)$ derived from the lattice constants a and c and values of the anisotropy field H_A (at room temperature) in various $R_2Fe_{14}B$ compounds.

Compound	$1-3/8(c/a)^2$	$\mu_0 H_A$(T)	R valency
$Lu_2Fe_{14}B$	0.302	2.64	3+
$Y_2Fe_{14}B$	0.293	2.35	3+
$Gd_2Fe_{14}B$	0.291	2.36	3+
$Ce_2Fe_{14}B$	0.284	2.64	4+
$Th_2Fe_{14}B$	0.278	2.03	4+
$La_2Fe_{14}B$	0.167	1.97	3+

The occurence of an easy c-axis magnetization at room temperature as well as at 4.2K was proposed for compounds $R_2Fe_{14}B$ in which R is one of the heavy rare earth metals Gd, Tb,Ho or Dy (29). There is at most a small contribution to the anisotropy by Gd, which can be deduced from the fact that H_A in $Gd_2Fe_{14}B$ is about the same as in compounds where R is nonmagnetic. In the remaining compounds with heavy rare earth elements the H_A values expected for temperatures below 300K are to high to be measured by our pulsed field equipment. This is propably the reason that attempts to measure the high temperature behaviour of $H_A(T)$ in $R_2Fe_{14}B$ with R=Dy or Tb were unsuccessfull even at temperatures close to the Curie temperature. Results obtained for $Ho_2Fe_{14}B$ above room temperature are included in Fig. 14.

Results of the measurements of the temperature dependence of the ac-susceptibilty ($\chi_i(T)$) are shown in Fig. 15 for various $R_2Fe_{14}B$ compounds in which R is nonmagnetic (R=La,Y,

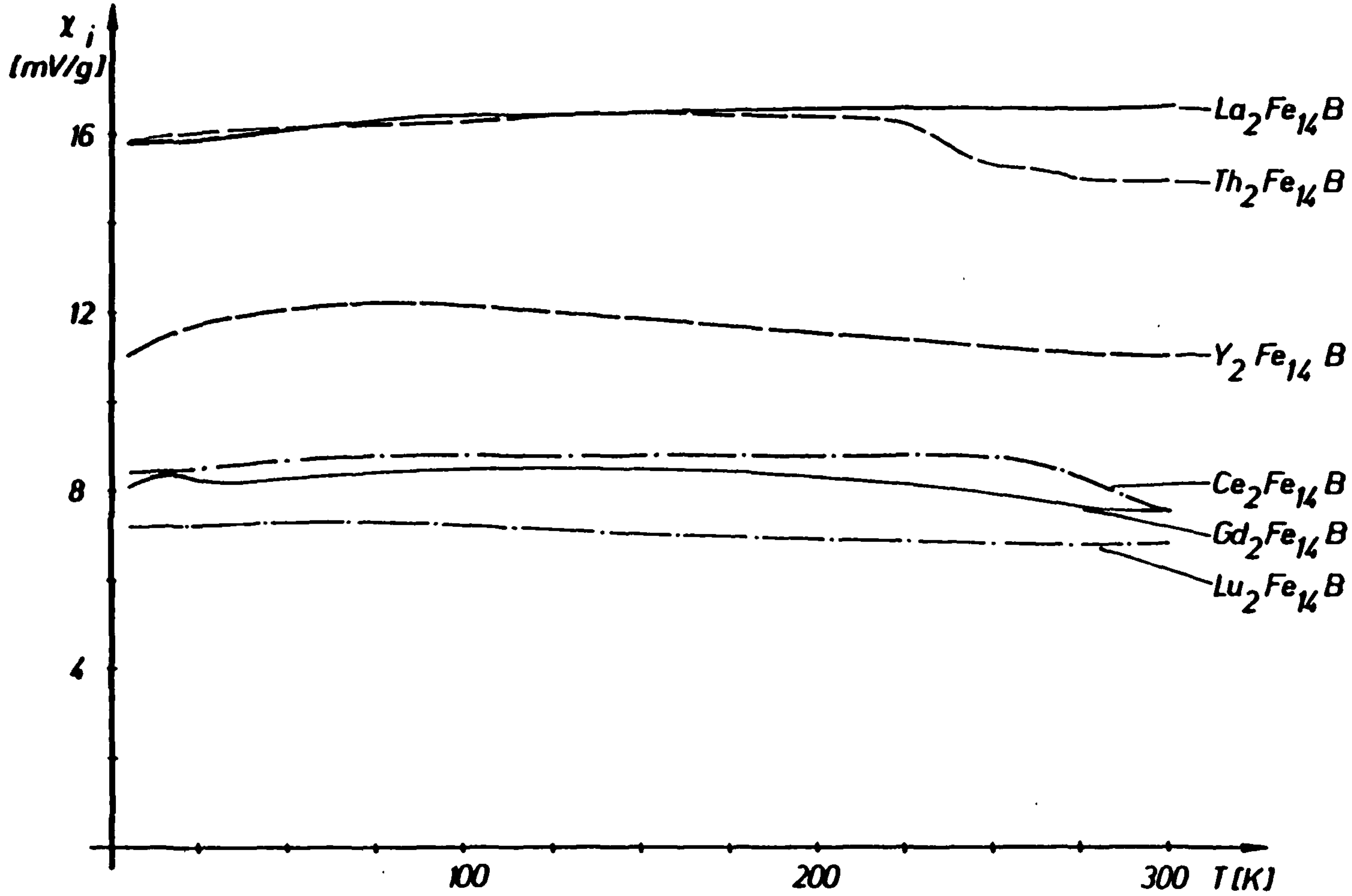

15. Temperature dependence of the initial susceptibility of $R_2Fe_{14}B$ (R=La,Ce,Gd,Lu,Y,Th).

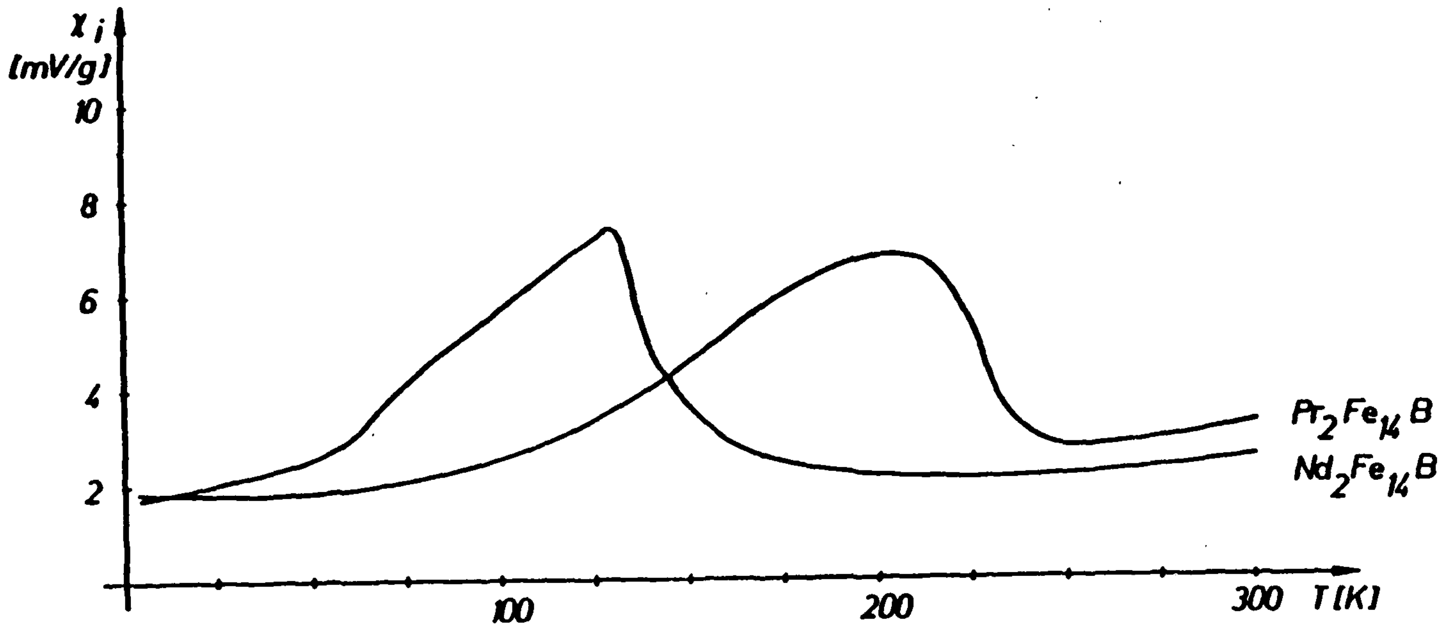

16. Temperature dependence of the initial susceptibility of $R_2Fe_{14}B$ (R=Pr,Nd).

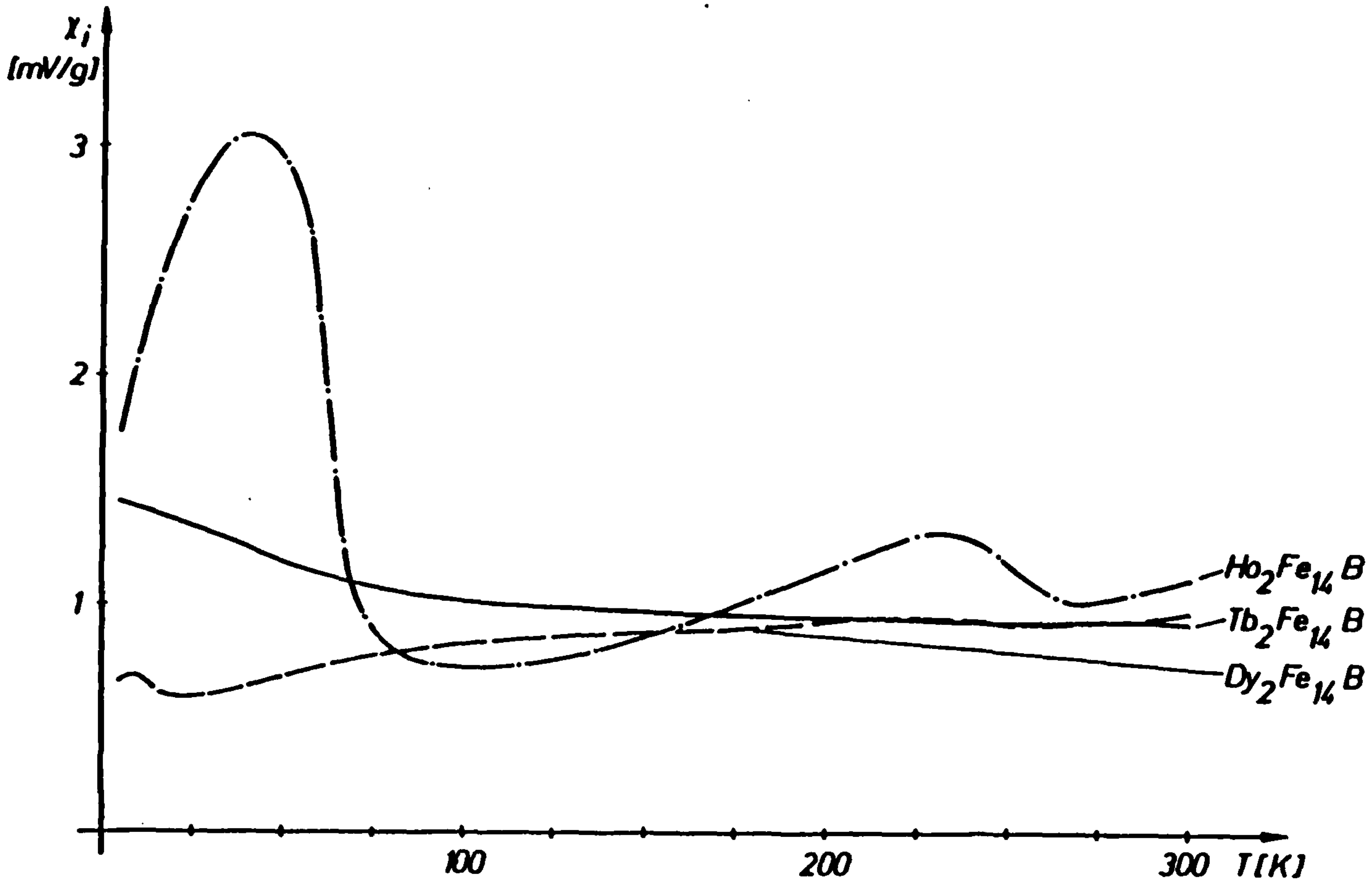

17. Temperature dependence of the initial susceptibility of $R_2Fe_{14}B$ (R=Ho,Tb,Dy).

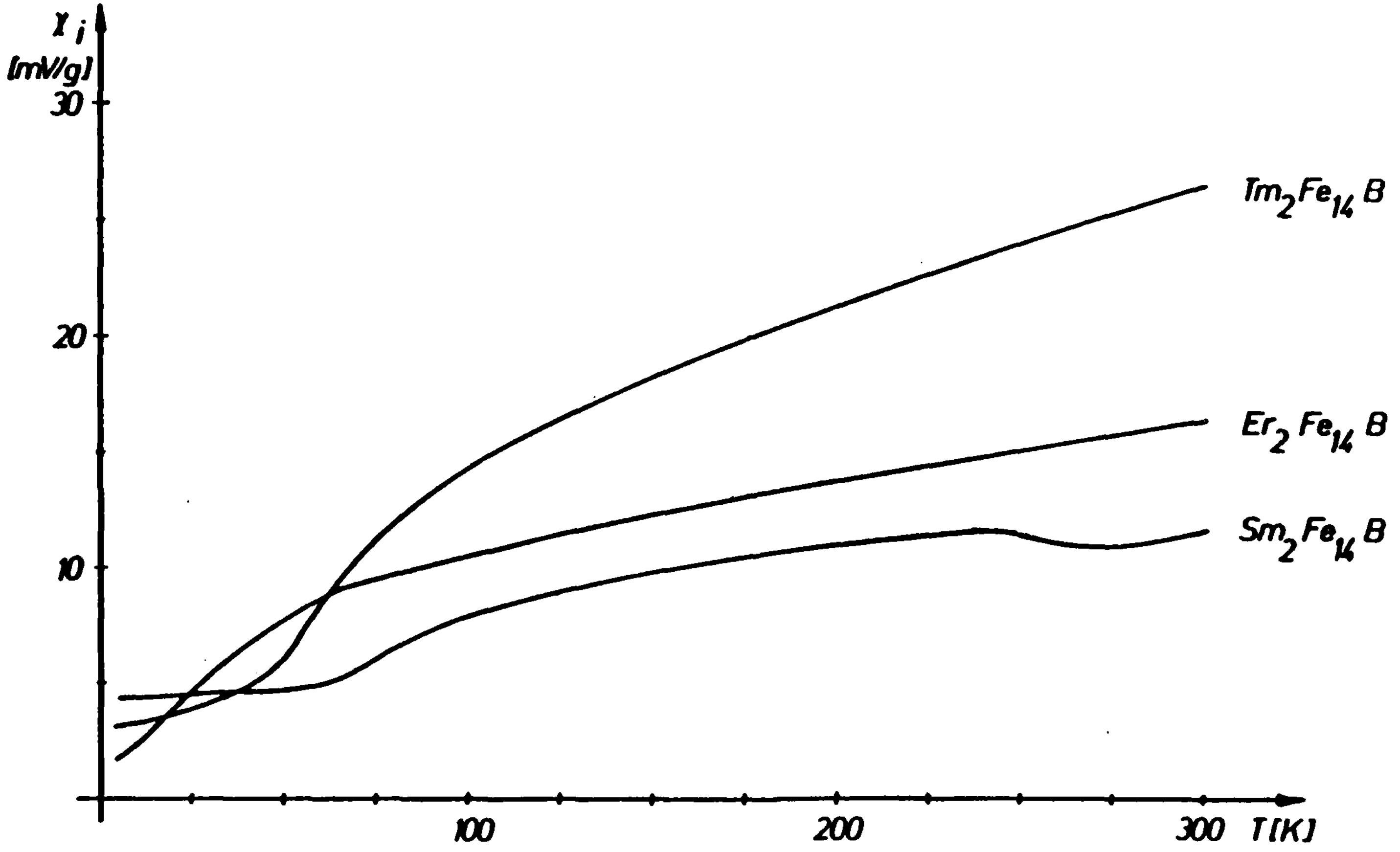

18. Temperature dependence of the initial susceptibility of $R_2Fe_{14}B$ (R=Sm,Tm,Er).

Th,Ce,Lu) or where the 4f moments consists exclusively of a spin moment (R=Gd). In all cases the values of χ_i varies only slightly with the temperature. Considerable more variation with temperature has been observed in the $\chi_i(T)$ curves of the compounds $Pr_2Fe_{14}B$ and $Nd_2Fe_{14}B$ (see Fig.16) and $Ho_2Fe_{14}B$ while in $Tb_2Fe_{14}B$ and $Dy_2Fe_{14}B$ the variation of χ_i with T is rather modest (see Fig. 17). In all compounds mentioned above X-ray diffraction studies on aligned powder have shown that the c-axis is the easy axis of magnetization at room temperature. $\chi_i(T)$ curves of compounds where an easy plane of magnetization was found ($Sm_2Fe_{14}B$, $Er_2Fe_{14}B$ and $Tm_2Fe_{14}B$) are shown in Fig. 18). The initial susceptibilty χ_i is defined as follows:

$$\chi_i = \lim(\Delta M/\Delta H_i)|_{\Delta H_i \to 0} \qquad (79)$$

where H_i the intenal field is. Due to the presence of a demagnetizing field (which is described by the demagnetizing factor N) the experimentally measured initial susceptibility $\chi_i$eff has the form:

$$\chi_i \mathrm{eff} = [(1/\chi_i)+N]^{-1} \qquad (80)$$

The intenal initial susceptibility χ_i is small when the material has either a large magnetic anisotropy or a large magnetoelastic energy. In such cases $N \ll \chi_i$ and the effect of the demagnetizing field can be neglected.

A crude estimate of χ_i for three different cases of easy directions of magnetizations can be obtained, assuming that only rotational magnetization processes occure (30):

$$\chi_i = M_s^2/(3K_1+(9/2)\lambda\sigma) \qquad \text{(easy c-axis)} \qquad (81)$$

$$\chi_i = M_s^2/(6(K_1+2K_2)+9\lambda\sigma) \qquad \text{(easy plane)} \qquad (82)$$

$$\chi_i = M_s^2/((2K_1+3\lambda\sigma)-2K_1F(\eta)) \qquad \text{(easy cone)} \qquad (83)$$

where $F(\eta)$ is defined as follows:

$$F(\eta)=(5+6\eta)/(1+2\eta) \qquad \eta = K_2/K_1 \qquad (84)$$

and where λ and σ represemts the magnetostriction and the intenal stresses, respectively.

Equation 81 shows that the temperature dependence of χ_i should be proportional to M_s^2 and reciprocal proprtional to K_1. Compounds where the anisotropy is exclusively due to the 3d sublattice magnetization (R=La,Th,Y,Ce,Gd,Lu) show a with increasing temperature slightly increasing H_A (see Fig. 14). Substituting $H_A = 2K_1/M_s$ into equ. 81 and neglecting magnetoelastic effects one expects the initial susceptibility to vary with temperature as $\chi_i = M_s/H_A$. Since M_s as well as H_A are nearly temperature independent between 4.2K and room temperature in these materials the $\chi_i(T)$ curves as given in Fig. 15 are in satisfactory agreement with the theoretical predictions.

For compounds where the easy axis of magnetization is at room temperature the c-axis, it is possible to compare the observed χ_i values with according to equ. 81 calculated data as given in table 6.

AD-A170 788 ANISOTROPY AND MICROSTRUCTURE OF RARE EARTH PERMANENT MAGNET MATERIALS..(U) TECHNISCHE UNIV VIENNA (AUSTRIA) INST OF APPLIED AND TECHNICA.. P SKALICKY ET AL. 2/2

UNCLASSIFIED JAN 86 R/D-4060A-R-MS DAJA45-84-C-0010 F/G 20/3 NL

END

DATE FILMED

9-86

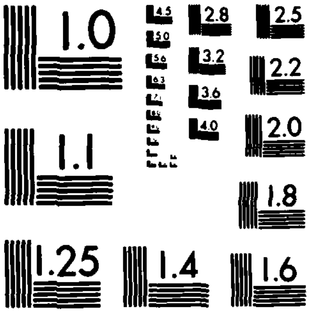

MICROCOPY RESOLUTION TEST CHART
NATIONAL BUREAU OF STANDARDS-1963-A

Table 6. Saturation magnetization (M_S), anisotropy field ($\mu_0 H_A$) and the experimental and theoretical initial susceptibility which are in order to be comparabel normalised to the χ_i value of $Y_2Fe_{14}B$. All values are taken at room temperature.

Compound	M_S (Am^2/kg)	$\mu_0 H_A$ (T)	χ_i exp	χ_i calc
$Y_2Fe_{14}B$	154	2.35	1	1
$La_2Fe_{14}B$	149	1.97	1.51	1.16
$Ce_2Fe_{14}B$	119	2.64	0.72	0.68
$Pr_2Fe_{14}B$	150	7.5	0.28	0.31
$Nd_2Fe_{14}B$	147	7.5	0.23	0.30
$Gd_2Fe_{14}B$	84	2.36	0.68	0.54
$Ho_2Fe_{14}B$	83	9.2	0.10	0.15
$Lu_2Fe_{14}B$	111	2.64	0.62	0.64

According the fact that χ_i signals as measured by ac-susceptibilty are generally difficult to calibrate, the two last columns of table 6 are normalised to the values of $Y_2Fe_{14}B$. These values are now easy to compare. The trend of the data is in agreement comparing the theoretical and experimentally obtained values, indicating that the simple model as given by the equations 81,82 and 83 is basically correct.
Fig. 16 and Fig. 17 shows that cusps in the $\chi_i(T)$ curves of the compounds $Nd_2Fe_{14}B$, $Pr_2Fe_{14}B$ and $Ho_2Fe_{14}B$ are visible. In $Nd_2Fe_{14}B$ this cusp is due to the low temperature spinreorientation which was found with other methods too. According to equ.81 and 83 χ_i passes through a maximum when the easy axis changes from the c-axis (K_1>0) to an easy cone (K_1<0). However in $Pr_2Fe_{14}B$ single crystal investigations showed that no anisotropy anomaly exists (31). Therefore the cusp in $\chi_i(T)$ might be due to a second magnetic phase. In $Ho_2Fe_{14}B$ the low temperature situation of the anisotropy is not yet clear. In $Dy_2Fe_{14}B$ and $Tb_2Fe_{14}B$ the values of χ_i are particular low, which might be a consequence of the rather high anisotropy fields of these compounds. Low χ_i values are due to the low magnetization of the $R_2Fe_{14}B$ (R=Sm,Er,Tm) expected. The reason why these compounds have nevertheless quite appriciable χ_i values (see Fig. 18) stems from the fact that all these materials exhibit an easy plane of magnetization, which might enhance the domain mobility drastically.

5.3) Stochiometry studies

All compounds in these materials are always based on $R_2Fe_{14}B$. The magnetic anisotropy is a sensitive tool in order to study any change of the local surrounding. Investigations performed on $Sm(Co,Fe,Cu,Zr)_{7.5}$ magnets with various heat treatments showed a remarkable change of the $H_A(T)$ behaviour (32). In the 2/17 structure changes of the

Th,Ce,Lu) or where the 4f moments consists exclusively of a spin moment (R=Gd). In all cases the values of χ_i varies only slightly with the temperature. Considerable more variation with temperature has been observed in the $\chi_i(T)$ curves of the compounds $Pr_2Fe_{14}B$ and $Nd_2Fe_{14}B$ (see Fig.16) and $Ho_2Fe_{14}B$ while in $Tb_2Fe_{14}B$ and $Dy_2Fe_{14}B$ the variation of χ_i with T is rather modest (see Fig. 17). In all compounds mentioned above X-ray diffraction studies on aligned powder have shown that the c-axis is the easy axis of magnetization at room temperature. $\chi_i(T)$ curves of compounds where an easy plane of magnetization was found ($Sm_2Fe_{14}B$, $Er_2Fe_{14}B$ and $Tm_2Fe_{14}B$) are shown in Fig. 18). The initial susceptibilty χ_i is defined as follows:

$$\chi_i = \lim(\Delta M/\Delta H_i)\big|_{\Delta H_i \to 0} \qquad (79)$$

where H_i the intenal field is. Due to the presence of a demagnetizing field (which is described by the demagnetizing factor N) the experimentally measured initial susceptibility $\chi_i$eff has the form:

$$\chi_i \mathrm{eff} = [(1/\chi_i)+N]^{-1} \qquad (80)$$

The intenal initial susceptibility χ_i is small when the material has either a large magnetic anisotropy or a large magnetoelastic energy. In such cases $N \ll \chi_i$ and the effect of the demagnetizing field can be neglected.

A crude estimate of χ_i for three different cases of easy directions of magnetizations can be obtained, assuming that only rotational magnetization processes occure (30):

$$\chi_i = M_s^2/(3K_1+(9/2)\lambda\sigma) \qquad \text{(easy c-axis)} \qquad (81)$$

$$\chi_i = M_s^2/(6(K_1+2K_2)+9\lambda\sigma) \qquad \text{(easy plane)} \qquad (82)$$

$$\chi_i = M_s^2/((2K_1+3\lambda\sigma)-2K_1F(\eta)) \qquad \text{(easy cone)} \qquad (83)$$

where $F(\eta)$ is defined as follows:

$$F(\eta)=(5+6\eta)/(1+2\eta) \qquad \eta = K_2/K_1 \qquad (84)$$

and where λ and σ represemts the magnetostriction and the intenal stresses, respectively.

Equation 81 shows that the temperature dependence of χ_i should be proportional to M_s^2 and reciprocal proprtional to K_1. Compounds where the anisotropy is exclusively due to the 3d sublattice magnetization (R=La,Th,Y,Ce,Gd,Lu) show a with increasing temperature slightly increasing H_A (see Fig. 14). Substituting $H_A=2K_1/M_s$ into equ. 81 and neglecting magnetoelastic effects one expects the initial susceptibility to vary with temperature as $\chi_i=M_s/H_A$. Since M_s as well as H_A are nearly temperature independent between 4.2K and room temperature in these materials the $\chi_i(T)$ curves as given in Fig. 15 are in satisfactory agreement with the theoretical predictions.

For compounds where the easy axis of magnetization is at room temperature the c-axis, it is possible to compare the observed χ_i values with according to equ. 81 calculated data as given in table 6.

local symmetry are possible, which influences naturally H_A. It is an interesting question to look if a similar behaviour is detectable in the $R_2Fe_{14}B$ too.
Therefore the system $Nd_{15}Fe_{85-x}B_x$ was studied. Fig.19 shows the concentration dependence of the Curie temperature of this sery. For x⩽4 the ordering temperature is typical for that of Nd_2Fe_{17}, whereas for x>4 a concentration independent Curie temperature typical for $Nd_2Fe_{14}B$ was found. Fig. 20 shows the temperature dependence of the anisotropy field of the usual $Nd_{15}Fe_{77}B_8$ in comparison with $Nd_{15}Fe_{83}B_2$ in the as cast state and after an annealing procedure. The $H_A(T)$ behaviour is very similar. In Fig.21 $H_A(T)$ of $Nd_{15}Fe_{77}B_8$ is compared with that of $Nd_{15}Fe_{82}B_3$, Fig.22 shows the same for $Nd_{15}Fe_{85}B_5$. In all cases nearly no stochiometry dependence of $H_A(T)$ was detected, indicating a very small homogeneity range of the $Nd_2Fe_{14}B$ compound.

Another attempt fot this purpose is given in Fig.23a where the $H_A(T)$ curves of some $R_2Fe_{14}B$ with that of $R_{15}Fe_{77}B_8$ (R=Y,Ce,Nd) are compared. The stochiometry is also there of no influence. Fig. 23b gives $H_A(T)$ of the same compounds but above room temperature. The much lower ordering temperature of the Ce-compound due to the tetravalent Ce is obvious.

Another game which might be interesting for technical applications is the partial substitution of the Nd by the cheaper Ce or by a mixture of Ce and La. Fig. 24a shows $H_A(T)$ of such highly substituted compounds

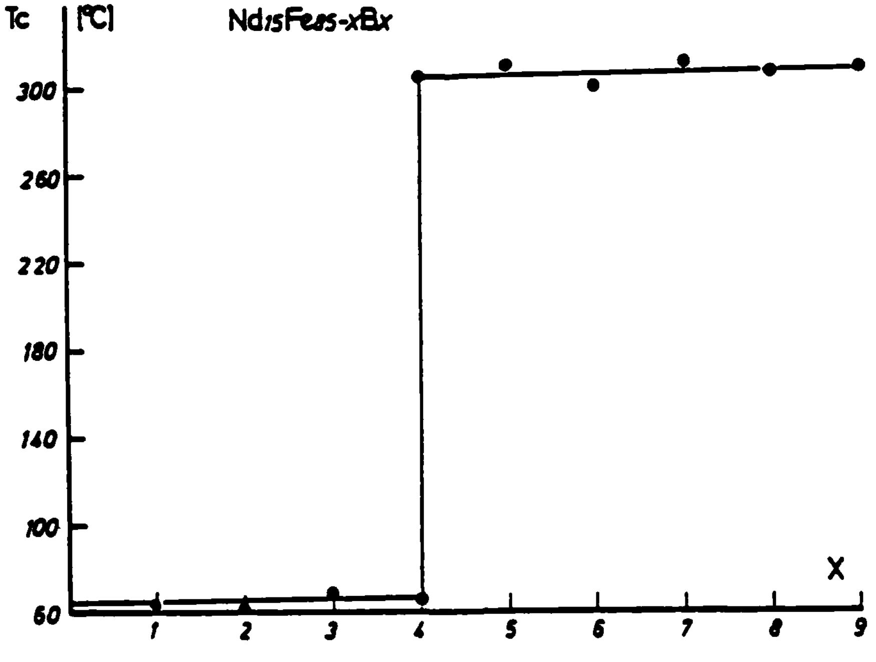

19. Concentration dependence of the Curie temperature of $Nd_{15}Fe_{85-x}B_x$.

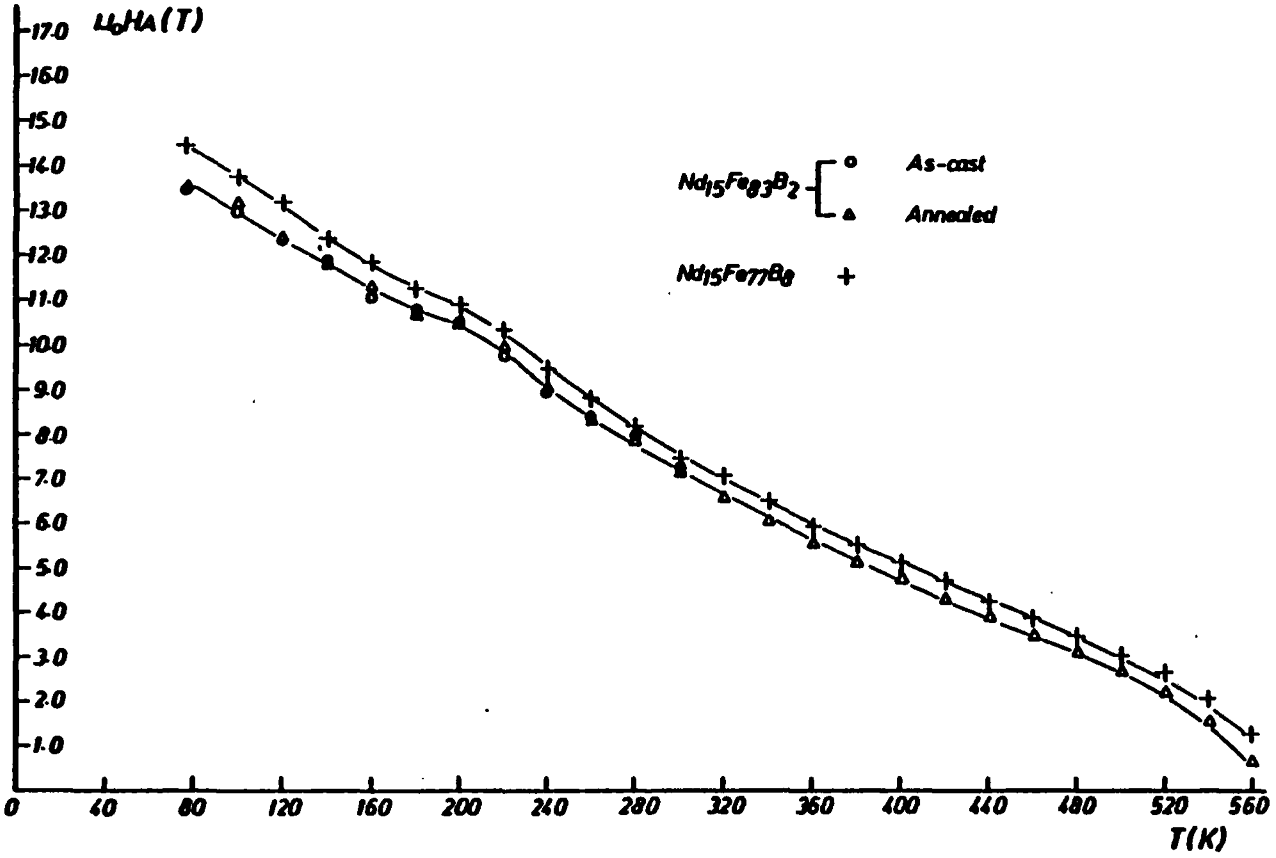

20. Temperature dependence of the anisotropy field of $Nd_{15}Fe_{77}B_8$ and $Nd_{15}Fe_{83}B_2$ (as cast and annealed).

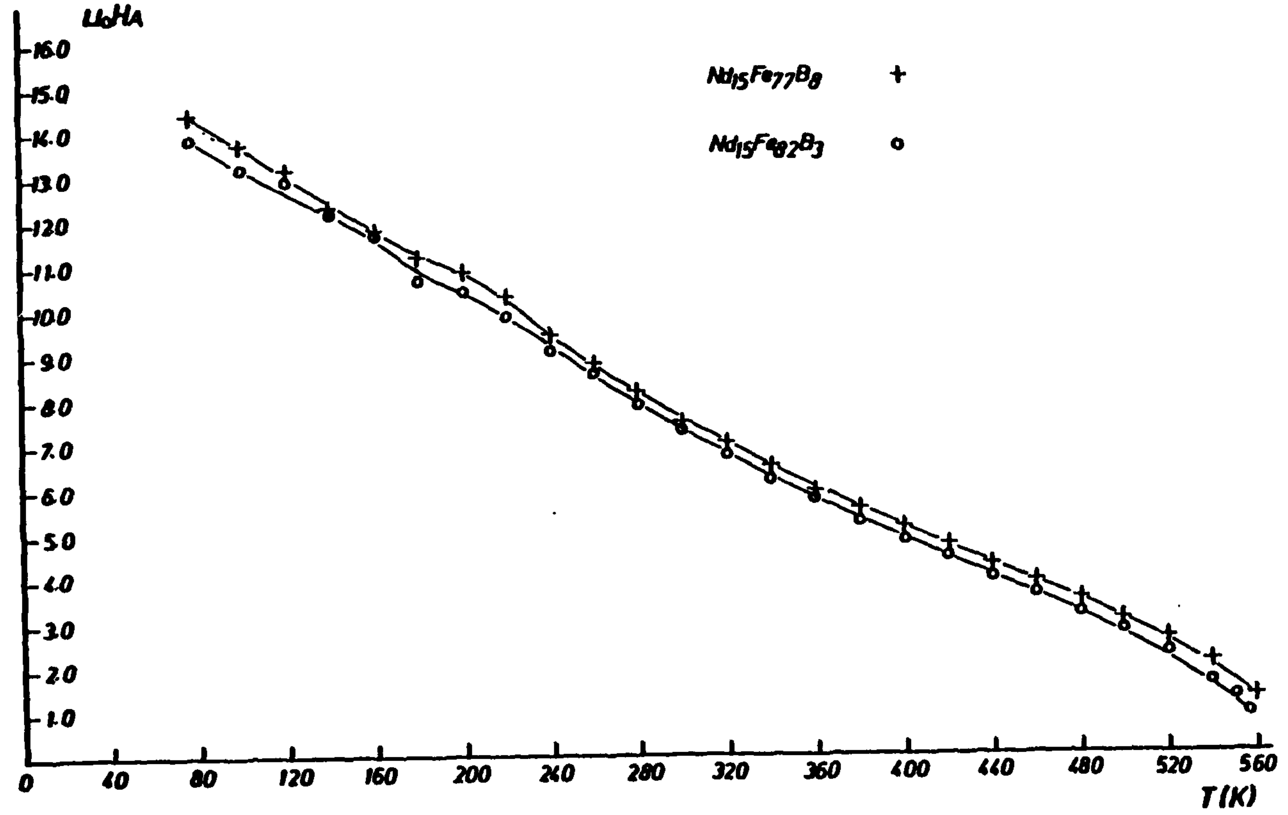

21. Temperature dependence of the anisotropy field of $Nd_{15}Fe_{77}B_8$ and $Nd_{15}Fe_{82}B_3$.

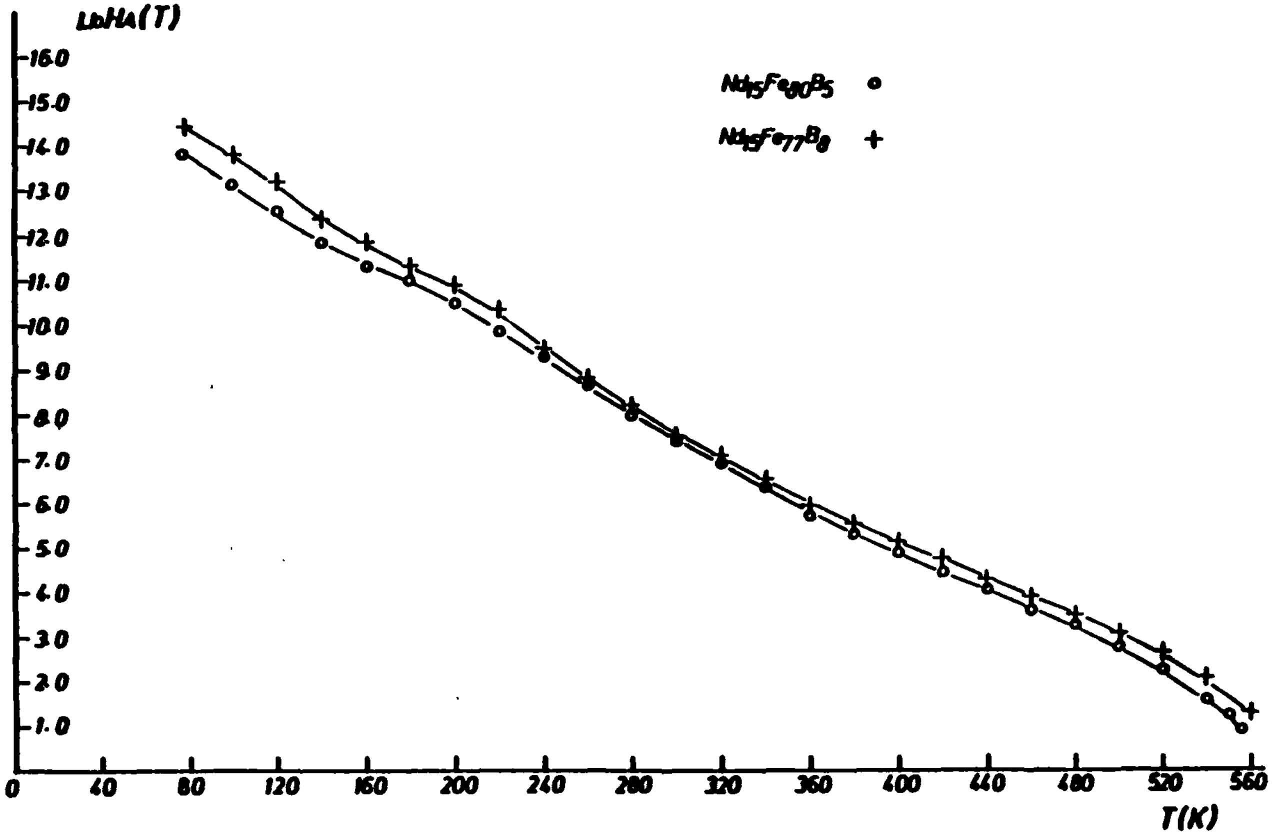

22. Temperature dependence of the anisotropy field of $Nd_{15}Fe_{77}B_8$ and $Nd_{15}Fe_{80}B_5$.

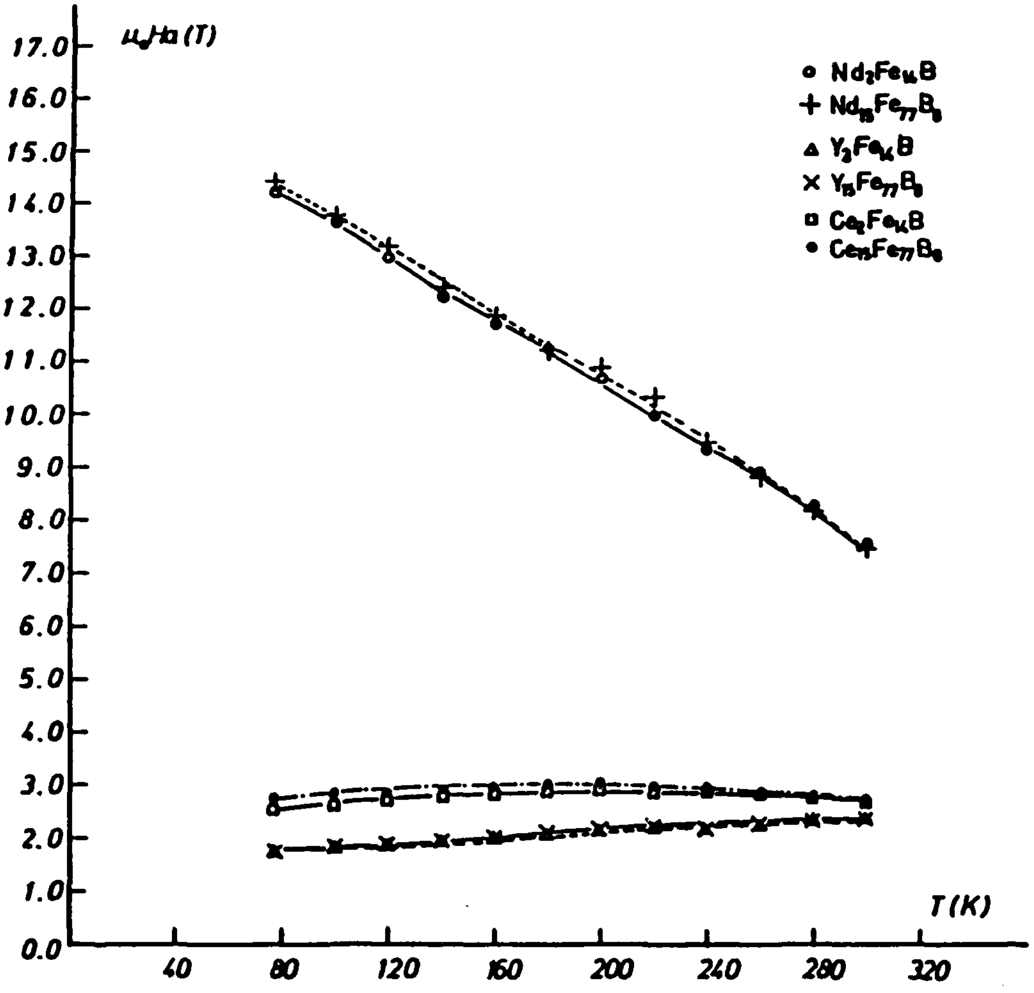

23a Comparison of the temperature dependence of $R_2Fe_{14}B$ with $R_{15}Fe_{77}B_8$ (R=Y,Ce,Nd) below room temperature.

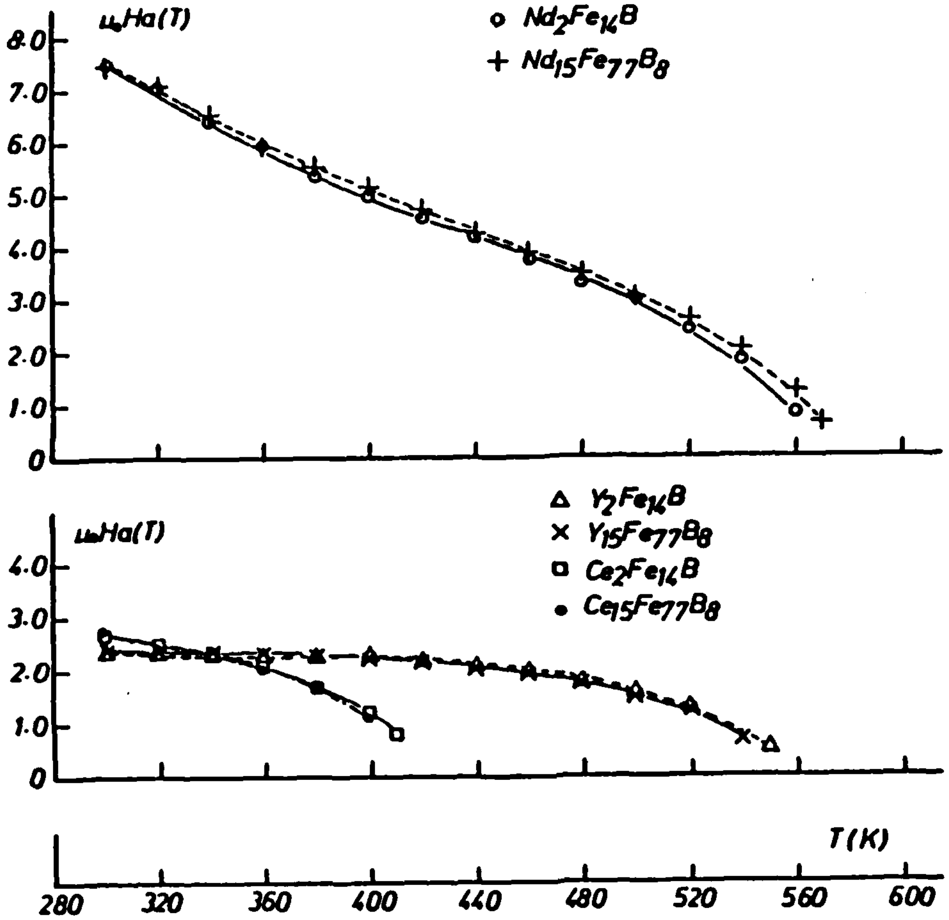

23b Comparison of the temperature dependence of $R_2Fe_{14}B$ with $R_{15}Fe_{77}B_8$ (R=Y,Ce,Nd) above room temperature.

$(Nd_{0.2}Ce_{0.8})_{15}Fe_{77}B_8$, $MM_{15}Fe_{77}B_8$, $(Nd_{0.7}Ce_{0.3})_{15}Fe_{77}B_8$, $(Nd_{0.6}Ce_{0.2}La_{0.2})_{15}Fe_{77}B_8$ in comparison with the normal $Nd_{15}Fe_{77}B_8$. In Fig.24b $H_A(T)$ of the same samples above room temperature is drawn. The similar behaviour of the $MM_{15}Fe_{77}B_8$ compared with $H_A(T)$ of $(Nd_{0.2}Ce_{0.8})_{15}Fe_{77}B_8$ demonstrates the high Ce-content of the MM-sample. This is due to the lowering effect of the Curie temperature of Ce in these compounds naturally not good. Therefore MM-Fe-B magnets might have magnet data at room temperature which are better then that of a ferrite however the thermal stability is much worse.

5.4) Commercial Nd-Fe-B based magnets

The following samples of technical permanent magnets supplied by Colt Industries based on Nd-Fe-B were available: "Coltl", which was one of the first produced sintered magnets, Crumax 30A, Crumax 35 and Crumax 40. From the Sumitomo Company the samples: "Suml", which was also one of the early Nd-Fe-B magnets, 30H, and a $Pr_{15}Fe_{77}B_8$ magnet was available. All materials were aligned sintered magnets.

Fig.25 shows the temperature dependence of the anisotropy field H_A of the Colt magnets. In Fig.26 the similar picture is drawn for the Sumitomo magnets. Below 200K an anisotropy anomaly, similar as described for all Nd containing polycrystalline Nd-Fe-B samples was observed for all permanent magnetic specimen. The exception here is only the Pr-Fe-B magnet, where no FOMP anomaly could be detected. For this magnet a smoothening of the singularity was oberved below 240K. The physical interpretation of this effect is not yet clear.

Arrows indicate this critical temperature, where a field induced first order magnetic phase transition begins to appear in the Nd-Fe-B containing magnets. The theoretical explanation is the same as that given for pure $Nd_2Fe_{14}B$ (see chapter 5.2). It should be noted that below this critical temperature the meaning of H_A is no longer that of usual anisotropy field, because there H_A is the critical field which is caused by the occurence of relative minima in the anisotropy energy surface; therefore $H_{cr} < H_A$ is valid.In some cases it is possible to observe both singularities, that which is due to the FOMP transition and one additional peak at higher fields indicating the real anisotropy field (see e.g. the $H_A(T)$ curve of the sample 30H in Fig.26; the upper branch describes the real $H_A(T)$, whereas the lower branch is $H_{cr}(T)$ due to the FOMP). It should be noted that the "H_A-singularity" disappears at approximately 135K where the spinreorientation to an easy cone starts. Below this temperature also according to the theoretical considerations the singularity in d^2M/dt^2 vs H, which occurs in the easy c-axis case, should no longer exist. Above 200K, however,

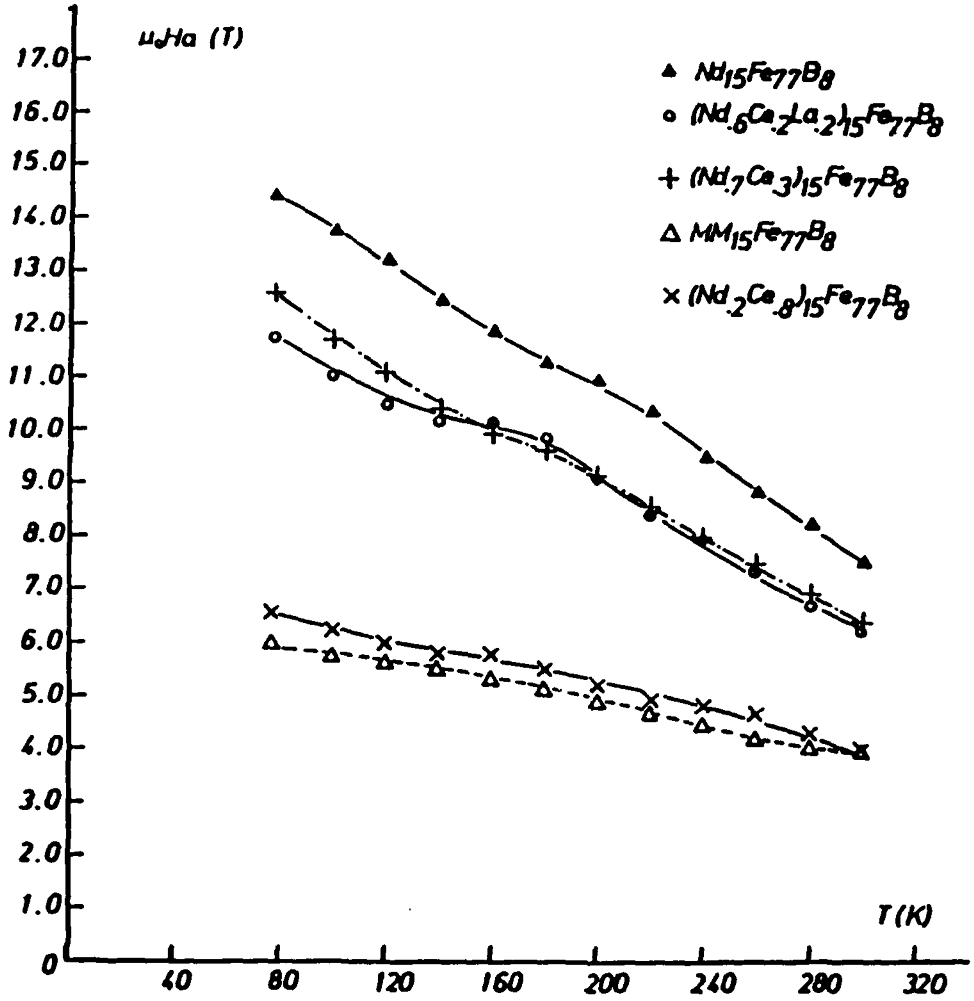

24a Temperature dependence of the anisotropy field of $(Nd_{0.7}Ce_{0.3})_{15}Fe_{77}B_8$, $(Nd_{0.2}Ce_{0.8})_{15}Fe_{77}B_8$, $MM_{15}Fe_{77}B_8$, $(Nd_{0.6}Ce_{0.2}La_{0.2})_{15}Fe_{77}B_8$ and $Nd_{15}Fe_{7}B_8$ below room temperature.

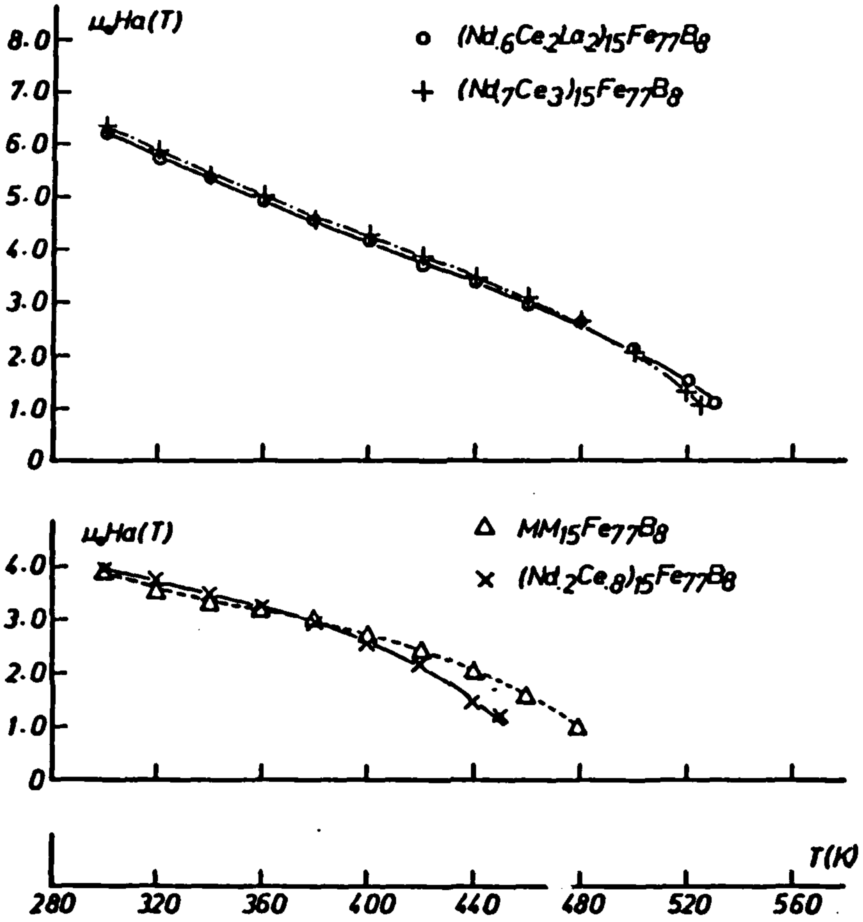

24b Temperature dependence of the anisotropy field of $(Nd_{0.7}Ce_{0.3})_{15}Fe_{77}B_{8}$, $(Nd_{0.2}Ce_{0.8})_{15}Fe_{77}B_{8}$, $MM_{15}Fe_{77}B_{8}$, $(Nd_{0.6}Ce_{0.2}La_{0.2})_{15}Fe_{77}B_{8}$ and $Nd_{15}Fe_{77}B_{8}$ above room temperature.

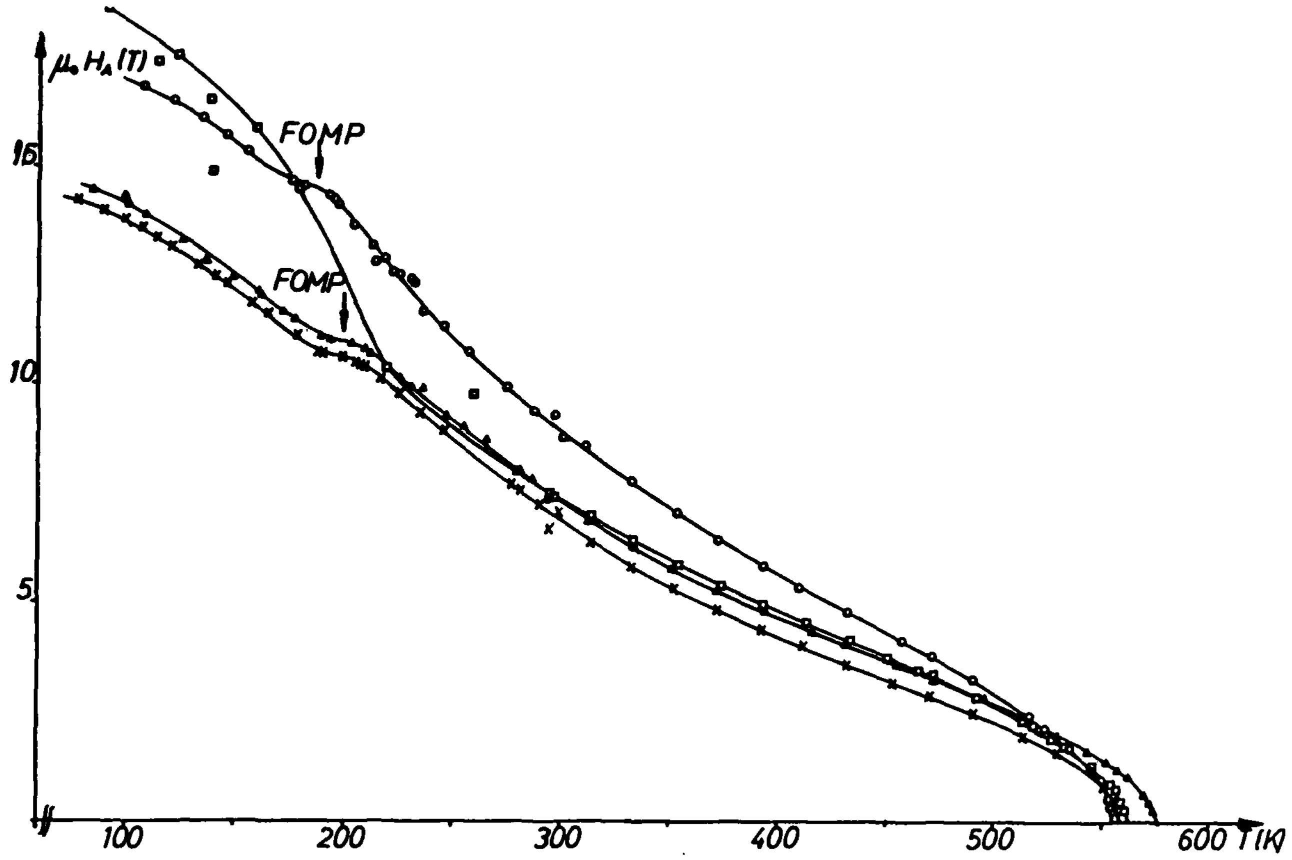

25. Temperature dependence of the anisotropy field of the Colt-magnets: "Colt 1" (□), Crumax 30A (○), Crumax 35 (×) and Crumax 40 (▲).

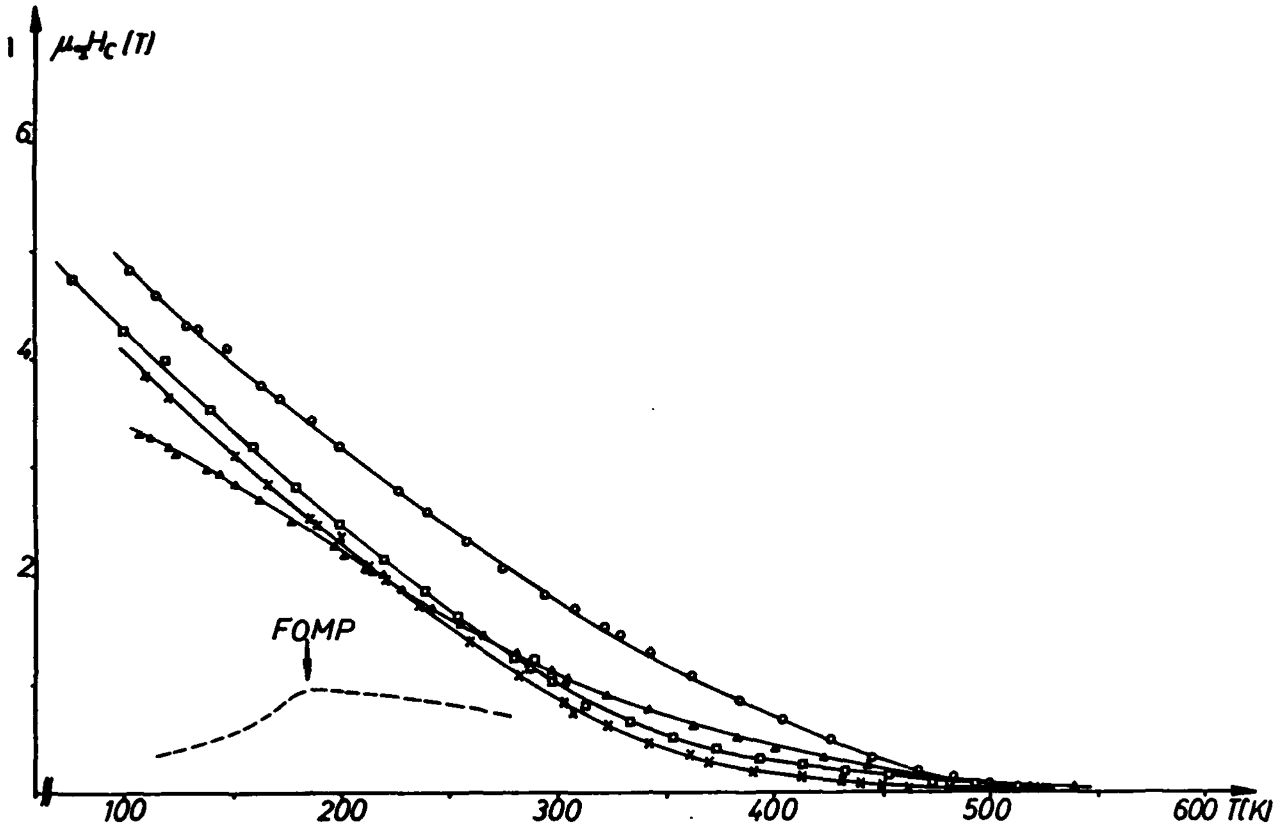

27. Temperature dependence of the coercivity field of the Colt-magnets: "Colt 1" (□), Crumax 30A (○), Crumax 35 (×) and Crumax 40 (▲).

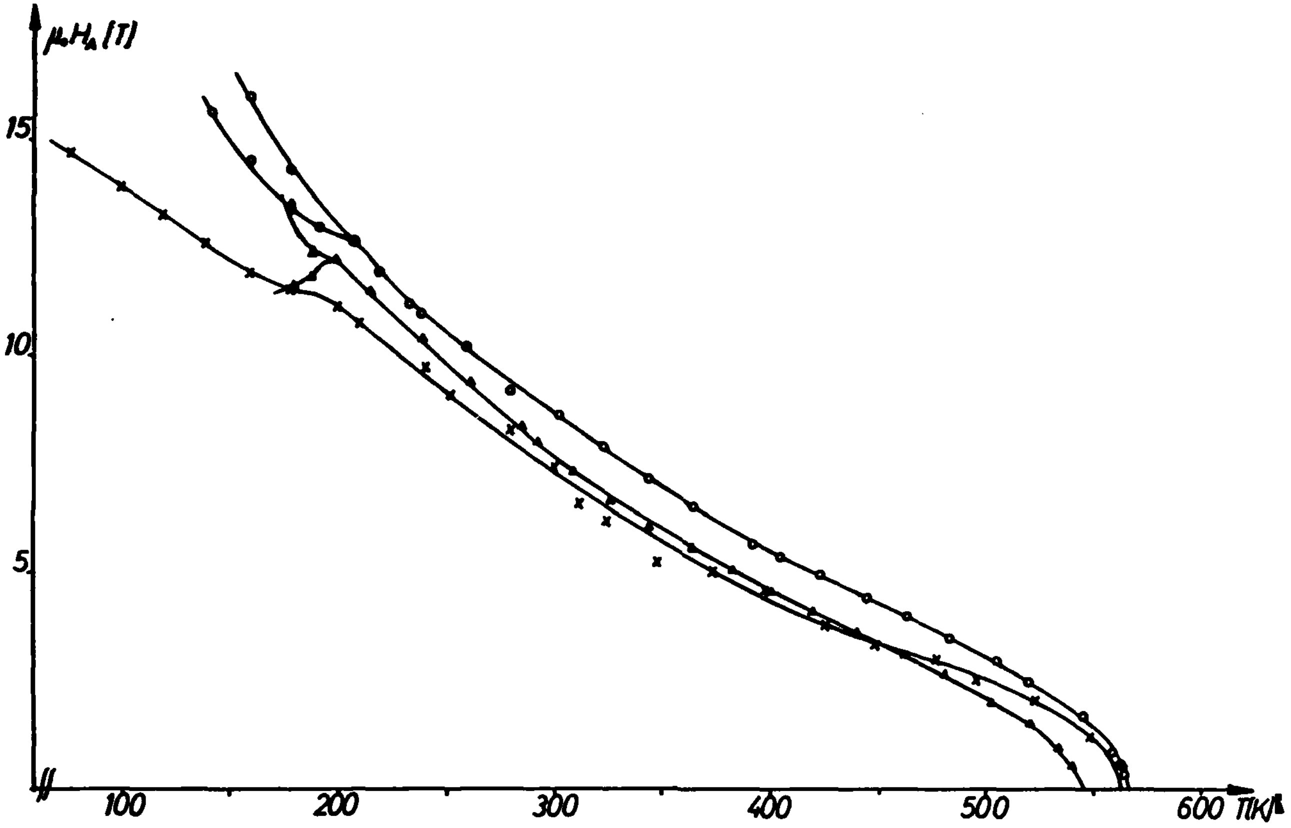

26. Temperature dependence of the anisotropy field of the Sumitomo-magnets: "Sum 1" (×), 30H (○) and $Pr_{15}Fe_{77}B_8$ (▲).

the anisotropy field as measured by the SPD-technique is in fact the real physically relevant anisotropy field. It is a great advantage of the SPD- method that it allows to determine the real anisotropy field (for a uniaxial material that field which is necessary to rotate the magnetization vector from the c-axis into the hard plane) independent of any mathematical definition.

Between 200K and the Curie temperature the $H_A(T)$ curves of all Colt samples except that of the Crumax 30A are very similar with respect to the magnitude as well as to the character. The Crumax 30A material exhibits remarkable higher values of H_A (e.g. at room temperature $\mu_0 H_A$ =9T) indicating a substitution of the Nd by a heavy rare earth element. In the case of the Sumitomo magnets a similar result was obtained. The $H_A(T)$ curve of the "30H" magnet lies above that of the usual $Nd_{15}Fe_{77}B_8$ material ("Sum1") indicating that there also a partial substitution of the Nd by a heavy rare earth element was performed. The anisotropy behaviour of the $Pr_{15}Fe_{77}B_8$ magnet shows the highest lying $H_A(T)$ values.

A similar result was obtained for the temperature dependence of the coercivity ${}_IH_c$ (see Fig.27 for the Colt and Fig. 28 for the Sumitomo magnets). Also there the ${}_IH_c(T)$ values of Crumax 30A are much higher then that of all other samples. It should be noted that the spinreorientation causes no anomaly in ${}_IH_c(T)$. Only if the external field is applied perpendicular to the preferential axis a down-turn below 200K is detected (10)(see the dotted curve in Fig.27). The Sumitomo magnets show also a ${}_IH_c(T)$ characteristic which indicates the influence of the magnetic anisotropy. The ${}_IH_c(T)$ curve of the 30H sample is above that of the "Sum1" magnet and theat of the $Pr_{15}Fe_{77}B_8$ material lies at low temperatures above that of the other magnets; at higher temperatures ${}_IH_c(T)$ is below the curve of the 30H sample. Consequently the temperature dependence of a $Pr_{15}Fe_{77}B_8$ magnet is worse as that of a usual Nd-Fe-B material (d_IH_c/dT ($Pr_{15}Fe_{77}B_8$) $<d_IH_c/dT$ ($Nd_{15}Fe_{77}B_8$)). The physical reason of the disccontinuity at low temperatures of ${}_IH_c(T)$ as observed on the sample "Sum1" at low temperatures is not yet clear.

The most important idea of trying to explain the coercivity is due to (17) (see also chapter 3.4) to search for a correlation between the coercivity field and the nucleation field which can be caused by various sources. The mathematical expression of this nucleation field is K_1/M_s, which is same as that of the anisotropy field neglecting higher order anisotropy constants. This encourages to look if any correlation can be found between ${}_IH_c$ and H_A. The general mathematical onset used for this purpose is of the type:

$${}_IH_c(T) \text{ prop } H_A(T)^k \qquad (85)$$

The above described experimental techniques allows us to

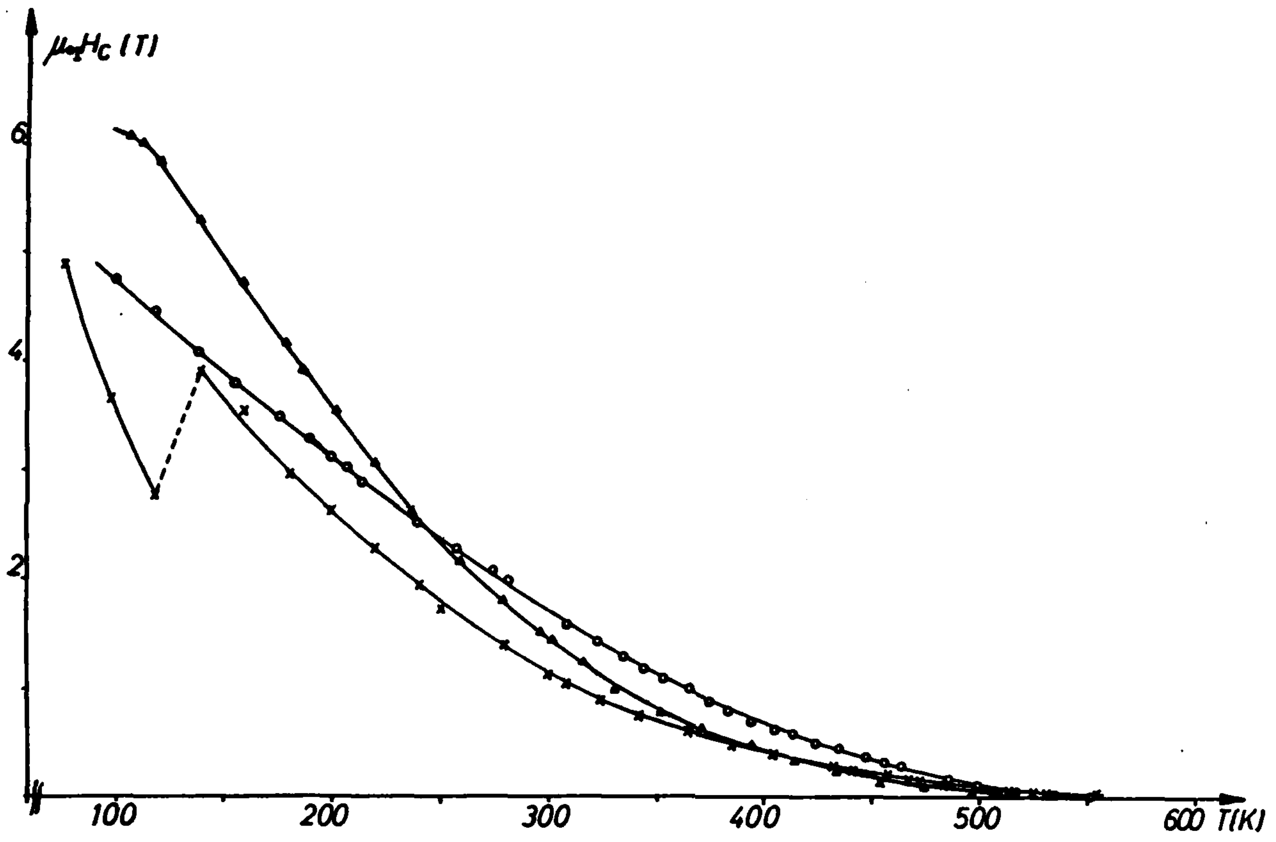

28. Temperature dependence of the coercivity field of the Sumitomo-magnets: "Sum 1" (×), 30H (○) and $Pr_{15}Fe_{77}B_8$ (▲).

determine $_IH_c$ as well as H_A on the same sample. This gives the chance testing theoretical models in a direct manner as it was not yet possible. According the fact that in the above mentioned work (17) various powers, depending on the special assumptions which are made for these calculations, are predicted, a plot of $\ln({}_IH_c(T)/{}_IH_c(T=300K))$ divided by $\ln(H_A(T)/H_A(T=300K))$ versus the temperature was made (see Fig.29 for the Colt magnets and Fig.30 for the Sumitomo materials).
The theoretical discussion as given in chapter 3.4 shows that for some simple cases a correlation between $_IH_c$ and the anisotropy field H_A can be expected. Fig.29 and Fig.30 shows that the coercivity mechanism changes with temperature, however not as clear as described by the above given formulas. Below 200K "k" values between 3/2 and 5/2 were obtained. However in this temperature range the analysis is not so reliable because of the occurence of a FOMP ($H_{cr}<H_A$; but the temperature dependence of H_{cr} is approximately the same as that of H_A). Above 200K the curves of k(T) of the samples Crumax 40 and 30A are looking similar, independent of the fact that the sample "30A" is a heavy rare earth substituted Nd-Fe-B magnet. The k(T) of the two other magnets (Colt1 and Crumax 35) are lying at higher values. The picture as obtained for the Colt magnets is supported by the results obtained for the Sumitomo samples. The "k(T)" curves of all 3 samples behave similar as the Crumax 40 and 30A (see Fig.29 and 30). This is especially surprising if one takes into account that the curve of the $Pr_{15}Fe_{77}B_8$ magnet is there included also. This means that at higher temperatures a mean value for k is approximately 5/2, which corresponds the power law as predicted by formula (76). A possible interpretation of the k(T) behaviour might be that the coercivity mechanism changes from a pinning of the domain walls at grain boundaries ($D<\delta_0$) at low temperatures to a volume pinning of extended domain walls at higher temperatures. This picture is reasonable because the with increasing temperature decreasing anisotropy (see Fig.25 and Fig.26) causes naturally an increase of the domain wall width. The there interesting fact is that in all cases the anisotropy of the hard magnetic matrix seams to determine the coercivity mechanism. Fig.29 and Fig.30 demonstrates that for k(T) the substitution of the Nd (Crumax 30A and Sumitomo 30H) but also Pr inspite of Nd is of minor importance, the different metallurgy (e. g. grain size, heat treatment) seams to determine $_IH_c(T)$ and consequently k(T). This is supported by preleminary results obtained on rapidly quenched $Nd_{15}Fe_{77}B_8$ ribbons leading to a "k" value (valid above room temperature) which was slightly higher then 1, but completely different to sintered Nd-Fe-B, indicating a different coercivity mechanism in rapidly quenched material. Concluding, this discussion shows that, the experimental

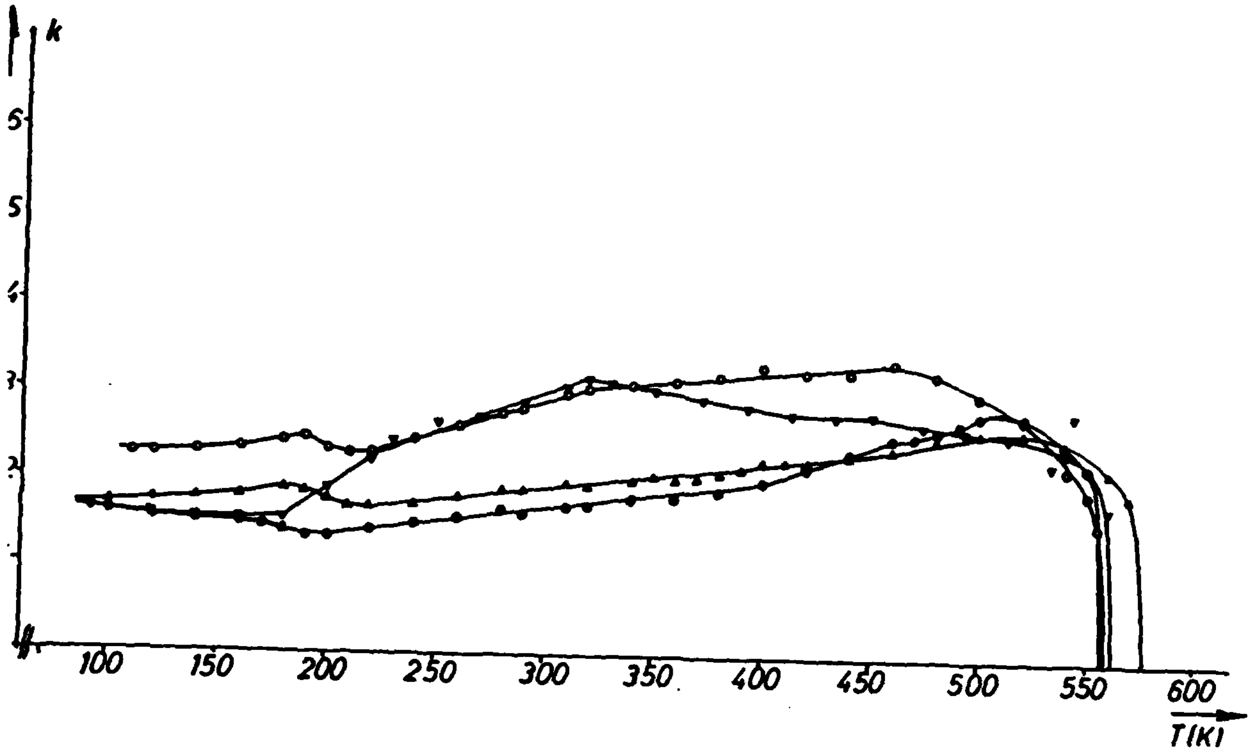

29. Temperature dependence of the power factor $k = \ln({}_{I}H_c(T)/{}_{I}H_c(T=300K))/\ln(H_A(T)/H_A(T=300K))$ for the Colt-magnets: "Colt 1" (▽), Crumax 30A (●), Crumax 35 (○) and Crumax 40 (△).

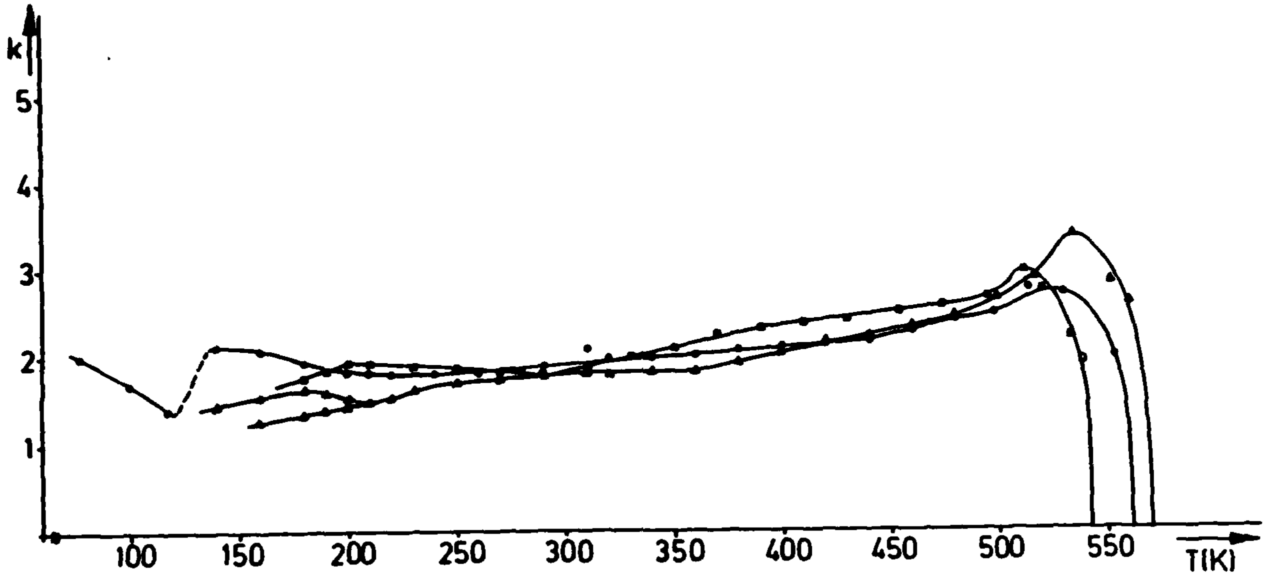

30. Temperature dependence of the power factor $k=\ln({}_{I}H_{c}(T)/{}_{I}H_{c}(T=300K))/\ln(H_{A}(T)/H_{A}(T=300K))$ for the Sumitomo- magnets: "Sum 1" (o), 30H (△) and $Pr_{15}Fe_{77}B_{8}$ (□).

possibilty of measuring $H_A(T)$ as well as ${}_IH_c(T)$ on the same sample, gives for the first time the chance to try to find a correlation between these two magnet parameters. In order to test these models ${}_IH_c(T)$ and $H_A(T)$ studies on various permanent magnets, representing different coercivity mechanisms, (e.g. rapidly quenched Nd-Fe-B magnets, Sm_2Co_{17} based materials but also ferrites) are therefore in progress.

6) Summary

The magnetic anisotropy of various R-Fe-B based samples was studied between 80K and the Curie temperature. All Nd containing samples showed at low temperatures a spinreorientation from the easy c-axis to an easy cone. Approaching this critical temperature higher order anisotropy constants become important, causing a jump in the M(H) curve. The theoretical background of such a FOMP transition for a tetragonal symmetry is there given. Unfortunately The problem can only be solved numerically.

A discussion of the definition of the anisotropy field shows that the choosen series expansion of the anisotropy energy determines essentially the mathematical expression of H_A. This is of great importance because the usually appplied extrapolation method suffers from this uncertainty. Additional this technique gives wrong H_A values because it is impossible to obtain a perfectly aligned sample, which consists of really single-domain, monodomainic particles. Theses difficulties combined with the generally to small fields which are available, makes the extrapolation method for determining H_A to a very uncertain technique. The SPD-method, on the other hand, allows to determine the real, physically relevant anisotropy field.

The study of the temperature dependence of the anisotropy field of the mixed crystal series $(Nd,R)_{15}Fe_{77}B_8$ (R=Y,La,Ce) allows an analysis of the Nd sublattice anisotropy, indicating its One Ion character. The 3d-sublattice anisotropy behaves anomal, because $H_A(T)$ decreases slightly with decreasing temperature. This can be explained assuming different contributions with differnet signs caused from the various Fe-sites. At room temperature a correlation between H_A and the coefficient $(1-(3/8)(c/a)^2)$ could be found, indicating the sensitivity of the 3d-anisotropy on the interatomic distance. A comparison of the H_A data of all $R_2Fe_{14}B$ compounds with the χ_i values gave evidence that χ_i of these hard magnetic materials is mainly determined by H_A as well as by the easy axis of magnetization.

Investigations of $H_A(T)$ of different stochiometries in the Nd-Fe-B system showed that $H_A(T)$ is insensitive against such variations, indicating a rather small homogeneity range of the $Nd_2Fe_{14}B$ phase. Attempts replacing Nd partly by Ce or fully by MM (Mischmetal) lead to reasonable high H_A values at room temperature, however due to the tetravalent Ce the ordering temperature is lowered, which lead to a much worse temperature stability as in the case of the pure Nd-materials.

The there available experimental technique (pulsed field with reasonable high fields) allows the determination of $H_A(T)$ and ${}_IH_c(T)$ on the same sample. This gives the opportunity to test models describing coercivity mechanisms. Any substitution of the Nd by heavy rare earth elements increases H_A as well as ${}_IH_c$. However analysing these magnet parameters assuming a general law of the type ${}_IH_c(T)$ prop. $(H_A(T))^k$ lead to "k" values which are at low temperatures close to 3/2 increasing with temperature, reaching 5/2 at room temperature. Regarding the corresponding figures, it is evident that this behaviour is independent from any substitution of the Nd by a heavy rare earth element. Even a $Pr_{15}Fe_{77}B_8$ sintered magnet showed the same k(T) characteristic. Consequently at low temperatures a pinning of the broad domain walls at thin grain boundaries have to be assumed. At higher temperatures these domain walls pinns at statistically distributed deffects (inclusions, impurity phases). It is clear that these explanations are only rough approaches determining the coercivity mechanism from the H_A to ${}_IH_c$ correlation. Further studies on other permanent magnets with well known coercivity mechanisms are proposed in order to test the reliability of these models.

References

1 K.S.V.L. Narasimhan
Proc. of 8-th Int. Workshop on rare earth magnets (1985)
Dayton (USA) p.459

2 J.F. Herbst, J.J. Croat, F.E. Pinkeron, W.P. Yelon
Phys. Rev., B29, 4176 (1984)

3 R. Grössinger, P. Obitsch, X.K. Sun, R. Eibler, H.R. Kirchmayr, F. Rothwarf, H. Sassik
Mat. Lett., 2, 539 (1984)

4 P. Givord, H.S. Li, J.M. Moreau, R. Perrier de la Bathie
E. du Tremolet de lacheisserie
Physica 130B, 323 (1985)

5 R. Grössinger, X.K. Sun, R. Eibler, K.H.J. Buschow, H.R. Kirchmayr
J. de Physique C6(9), C6-221 (1985)

6 G. Asti, F. Bolzoni
JMMM 15-18, 29 (1980)

7 G. Asti, F. Bolzoni, F. Leccabue, R. Panizzierie, L. Pareti, S. Rinaldi
JMMM 15-18, 561 (1980)

8 H.B. Callen, E. Callen
J. Phys. Chem. Solids 27, 1271 (1966)

9 G. Asti, S. Rinaldi
J. Applied Phys., 45, 3600 (1974)

10 R. Grössinger, H.R. Kirchmayr, R. Krewenka, K.S.V.L. Narasimhan, M. Sagawa
Proc. of 8-th Int. Workshop on rare earth magnets (1985)
Dayton (USA) p.565

11 Yang Fu-Ming, Zhao Xi-Chao, Zhao Ru-Wen, Yu Zhi-Hong, Zhang Shou Gong, Zhou Xi-Jian, Sun Tian-Duo
Proc. of 8-th Int. Workshop on rare earth magnets (1985)
Dayton (USA) p.529

12 X.K. Sun
Thesis (1985) Techn. Univ. Vienna

13 R. Grössinger et al
(1986) to be published

14 H. Träuble, O. Boser, H. Kronmüller, A. Seeger
phys. stat. sol., 10, 283 (1965)

15 K.D. Durst, H. Kronmüller
JMMM (1985) in print

16 J.J. Croat, J.F. Herbst, R.W. Lee, F.E. Pinkerton
J. Applied Phys., 55, 2078 (1984)

17 R. Kütterer, H.R. Hilzinger, H. Kronmüller
JMMM 4, 1 (1977)

18 H. Kronmüller, H.R. Hilzinger
JMMM 2, 3 (1976)

19 H. Kronmüller, H.R. Hilzinger
JMMM 5, 27 (1973)

20 A. Seeger, P. Schiller in Phys. Acoustics Vol. III A ed.
W.P. Mason (Academic Press, London 1966) p.361

21 R. Grössinger
J. Phys. D 15, 1545 (1982)

22 J. Fidler, R.Grössinger, H. Kirchmayr, P. Skalicky
Rep. of United States Army
DAJA (1983)-37-82-C-0050
DAJA (1984)-45-84-C-0010

23 R. Grössinger
Proc. of 6-th Int. Workshop on rare earth cobalt Perm.
Magnets (1982) Baden (Austria) p.305

24 G. Wouch, E.A. Jord Jr.
Am. J. Phys., 46, 464 (1978)

25 R. Grössinger, X.K. Sun,, R. Eibler, H.R. Kirchmayr
Proc. of 8-th Int. Workshop on rare earth magnets (1985)
Dayton (USA) p.553

26 K. Inomata
Jap. J. Applied Phys. 15, 821 (1976)

27 B. Szpunar, P.A. Lindgard
J. Phys F 9, L55 (1979)

28 R. Grössinger, X.K. Sun, R. Eibler, K.H.J. Buschow, H.R.
Kirchmayr
JMMM 85,(1986) in print

29 S. Sinnema, R.H. Radwanski, J.J.M. Franse, D.B. De Mooij
K.H.J. Buschow
JMMM 44, 333 (1984)

30 A. Seeger: Moderne Probleme der Metallphysik; Springer Verlag (1966) p.420

31 H. Yamauchi, M. Yamada, Y. Yamaguchi, H. Yamamoto, S. Hirosawa, M. Sagawa
JMMM 54-57, 575 (1986)

32 R. Grössinger, P. Obitsch, H .Kirchmayr, F. Rothwarf
IEEE Trans. on Magn. MAG-20, 1575 (1984)

ATE

LMED

-8